






Review

Characteristics and Behavior of Different Catalysts Used for Water Decontamination in Photooxidation and Ozonation Processes

José Rivera-Utrilla ^{1,*}, María Victoria López-Ramón ^{2,*}, Manuel Sánchez-Polo ¹, Miguel Ángel Álvarez ² and Inmaculada Velo-Gala ³

¹ Department of Inorganic Chemistry, Faculty of Science, University of Granada, 18071 Granada, Spain; mansanch@ugr.es

² Department of Inorganic and Organic Chemistry, University of Jaén, 23071 Jaén, Spain; malvarez@ujaen.es

³ Laboratory of Separation and Reaction Engineering-Laboratory of Catalysis and Materials (LSRE-LCM), Departamento de Engenharia Química, Faculdade de Engenharia, Universidade do Porto, Rua Dr. Roberto Frias s/n, 4200-465 Porto, Portugal; invega@ugr.es

* Correspondence: jrivera@ugr.es (J.R.-U.); mvlro@ujaen.es (M.V.L.-R.)

Received: 30 November 2020; Accepted: 16 December 2020; Published: 19 December 2020



Abstract: The objective of this study was to summarize the results obtained in a wide research project carried out for more than 15 years on the catalytic activity of different catalysts (activated carbon, metal-carbon xerogels/aerogels, iron-doped silica xerogels, ruthenium metal complexes, reduced graphene oxide-metal oxide composites, and zeolites) in the photooxidation (by using UV or solar radiation) and ozonation of water pollutants, including herbicides, naphthalenesulfonic acids, sodium para-chlorobenzoate, nitroimidazoles, tetracyclines, parabens, sulfamethazine, sodium diatrizoate, cytarabine, and surfactants. All catalysts were synthesized and then texturally, chemically, and electronically characterized using numerous experimental techniques, including N₂ and CO₂ adsorption, mercury porosimetry, thermogravimetric analysis, X-ray diffraction, Fourier-transform infrared spectroscopy, Raman spectroscopy, X-ray photoelectron spectroscopy, diffuse reflectance UV-vis spectroscopy, photoluminescence analysis, and transmission electron microscopy. The behavior of these materials as photocatalysts and ozonation catalysts was related to their characteristics, and the catalytic mechanisms in these advanced oxidation processes were explored. Investigations were conducted into the effects on pollutant degradation, total organic carbon reduction, and water toxicity of operational variables and the presence of different chemical species in ultrapure, surface, ground, and wastewaters. Finally, a review is provided of the most recent and relevant published studies on photocatalysis and catalyzed ozonation in water treatments using similar catalysts to those examined in our project.

Keywords: catalysts; photooxidation; ozonation; water pollutants; UV radiation; solar radiation

1. Introduction

Advanced oxidation processes (AOPs) are characterized by the in situ production of a sufficient amount of powerful chemical oxidants (e.g., hydroxyl radicals [HO•]) to oxidize and destroy organic pollutants in water and air. The free radicals generated are highly reactive species that can effectively degrade most organic and inorganic compounds and have elevated reaction rate constants (106–109 M⁻¹ s⁻¹). As shown in Table 1, AOPs include a wide range of systems capable of generating these radicals [1,2].

Table 1. Water treatment technologies based on advanced oxidation processes.

Non-Photochemical Processes	Photochemical Processes
<ul style="list-style-type: none"> • Oxidation in sub/supercritical water • Catalytic wet peroxide oxidation (Fenton reagent $\text{Fe}^{2+}/\text{H}_2\text{O}_2$) • Electrochemical oxidation • Radiolysis • Nonthermal plasma • Ultrasound • Ozonation in alkaline medium (O_3/OH^-) • Ozonation in the presence of hydrogen peroxide ($\text{O}_3/\text{H}_2\text{O}_2$) • Catalytic ozonation 	<ul style="list-style-type: none"> • Photolysis of water with vacuum UV • UV/hydrogen peroxide • UV/ozone • UV/radical generators • Photo-Fenton • Heterogeneous photocatalysis

There has been an increasing decline in water resources for human use and a growing rise in the consumption of water by populations, agriculture, and industry. Conventional water treatment systems are under strain and facing additional difficulties from the continual appearance of new pollutants. There is a need to increase the effectiveness and efficiency of polluted water treatment removal through the development of improved technologies [3,4].

Biological treatments with adsorbents and conventional chemical methods (chlorination, ozonation, or permanganate oxidation) are generally effective to treat polluted waters, but they sometimes fail to reduce pollutant levels sufficiently to comply with legislation and to allow utilization of the effluent [5,6]. AOPs are highly effective to oxidize many organic and inorganic compounds, including biologically toxic or non-degradable pollutants (e.g., aromatics, colorants, surfactants, pharmaceuticals, petroleum components, pesticides, and volatile organic compounds). These pollutants are commonly present in water at trace concentrations, ranging from a few ng/L to several $\mu\text{g}/\text{L}$. In general, contaminants are mineralized by oxidation into stable inorganic compounds such as carbon dioxide, water, or salts. The aim of applying AOPs in wastewaters is to diminish chemical contaminants and water toxicity to a sufficient extent to allow the treated water to be reintroduced into receiving streams or conventional sewage treatment plants [7–9]. This review focuses on AOPs that involve heterogeneous photocatalysis and catalytic ozonation.

Ever since reports in the 1960s and 1970s on the potential of ZnO and TiO_2 electrodes for water splitting and environmental remediation [10,11], heterogeneous photocatalysis has attracted considerable research attention. However, most semiconductors offer low photonic efficiency, and there is special interest in optimizing the optical characteristics of semiconductor materials [12,13]. There is a need to improve the performance of semiconductors and to explore the potential use of other materials for this purpose.

Numerous oxides and sulfides have appropriate chemical and physical properties for their utilization as photocatalysts [14,15]. Titanium dioxide is the most widely used photocatalyst but has a low quantum yield and shows a tendency to recombine the electrons and positive holes generated, leading to numerous attempts to improve the behavior of this semiconductor [16–18]. Technological interest in photocatalytic processes has made the development of effective photocatalysts one of the most important challenges in materials research. Photocatalysis is not only used in water treatments but also shows promise in other fields, including the generation of hydrogen by water splitting or the reduction in CO_2 to obtain different organic compounds [19,20]. Many carbon materials have been used in this field, ranging from activated carbons (ACs), carbon blacks, and graphite to novel forms such as carbon nanotubes, fullerenes, graphene, and graphitic carbon nitride. Investigations in this field initially focused on the application of carbon materials as supports for metallic catalysts, followed by their use as doping agents, as carbon-coating for titanium dioxide particles, and an electron donor/acceptor-forming composites with different metallic oxides. It was recently shown that some carbon materials possess self-photoactivity [21–29].

Three mechanisms have been proposed for the synergistic promotion of photocatalysis in titanium dioxide-nanotube composite materials: (i) nanotubes act as acceptors of the electrons photogenerated by titanium dioxide, inhibiting recombination of the electrons and positive holes that are generated; (ii) photoabsorption of the carbon material and generation of additional positive hole–electron pairs, increasing the generation of radicals; and (iii) carbon atoms act as a doping element of the TiO₂ network, decreasing the bandgap energy by introducing new energy bands between the valence and conduction bands of TiO₂, extending the applicability of the photocatalyst to less energetic radiations, such as those of the visible spectrum [30].

Another section of the present review addresses catalytic ozonation. Water treatment technologists have shown considerable interest in the important oxidation and disinfection potential of ozone. However, although ozone offers major advantages, it is associated with a few drawbacks, such as (i) low solubility and stability in water, (ii) low reactivity with certain organic compounds, and (iii) inability to completely transform organic compounds into CO₂, leaving degradation byproducts that can be more toxic than the original micropollutant. AOPs (O₃/H₂O₂, O₃/UV, O₃/catalysts) have been developed to increase the effectiveness of ozonation. Chen et al. [31] first described the heterogeneous catalytic ozonation of certain compounds using Fe₂O₃ as a catalyst. Subsequently, numerous catalysts have been studied, such as metal oxides [32,33], supported metal oxides [34,35], supported metals [36], mesoporous materials [37], and carbon materials [38] (AC by itself [39,40], carbon xerogels [41], carbon nanotubes [42], metal oxides supported on AC [43], metal-doped carbon aerogels [44], platinum supported on carbon nanotubes [45], and graphene derivatives [46]). The characteristics of the solution (pH, temperature, ionic strength, etc.) and the chemical and textural properties of the catalyst generally have a major influence on the efficacy of heterogeneous catalysis in ozone decomposition. It has frequently been observed that these materials are able to catalytically decompose ozone, generating HO• radicals. General conclusions on the underlying mechanisms of action are complicated by the wide range of solid catalyst types and surface properties and by interactions among the catalyst, ozone, and organic molecules.

With the above background, the aim of this review was to summarize the results of a wide >15-year investigation into the characteristics and behavior of numerous different catalysts (AC, metal–carbon xerogels/aerogels, iron-doped silica xerogels, ruthenium metal complexes, reduced graphene oxide–metal oxide composites, and zeolites) in the photooxidation (UV and solar) and ozonation of water polluted with herbicides, naphthalenesulfonic acids, sodium para-chlorobenzoate, nitroimidazoles, tetracyclines, parabens, sulfamethazine, sodium diatrizoate, cytarabine, and surfactants. Data are analyzed on the chemical, electronic, and textural characteristics of the catalysts, their catalytic activity in the degradation of the contaminants, and the effect of the chemical nature of the aqueous solution. A special section is devoted to the study of reaction mechanisms and the toxicity of degradation products. Many of the results obtained by the project have been published [40,44,47–81]. Finally, there is a discussion of the most recent and relevant results published on photocatalysis and catalyzed ozonation in water treatments using similar catalysts to those studied in our project.

2. Catalysts Used in Pollutant Photooxidation

AOPs involving photocatalytic processes that use visible or UV light to electronically activate catalysts have achieved promising results in the removal of organic pollutants that resist biological treatment [82]. Highly active HO• radicals that participate in photooxidation are generated via different mechanisms [83]. Photochemical and photocatalytic methods have proven highly effective for water treatments [84]. The studied catalysts include ACs, metal–carbon aerogels, iron-doped silica xerogels, ruthenium metal complexes, and rGO–metal oxide composites.

2.1. Activated Carbons

ACs exert major photocatalytic activity. Oxidation systems with UV or solar radiation have proven able to completely degrade multiple pollutants in an aqueous solution in the absence of the usual semiconductor materials when ACs are present [22–24,69,75].

ACs have been successfully used as photocatalysts to remove sodium diatrizoate (DTZ), a pharmaceutical iodinated contrast medium, in the presence of UV and solar light [69,75]. Four commercial ACs were used: Sorbo (S), Merck (M), Ceca (C), and Witco (W), as well as gamma-radiated ACs derived from S, M, C and W under different conditions, as previously described [85]. A novel approach was proposed, using ionizing (gamma) radiation to simultaneously generate oxidizing and reducing species and thereby modify the surface chemistry of the ACs [85]. Table 2 displays the nomenclature of the irradiated ACs obtained.

Table 2. Nomenclature of the activated carbon (AC) samples used (reproduced from [69] with permission of Elsevier, 2013).

Ceca series	C	Original Ceca carbon
	C-H [•]	Ceca carbon irradiated in the presence of H [•] radical
	C-e ⁻ _{aq}	Ceca carbon irradiated in the presence of e ⁻ _{aq}
	C-HO [•]	Ceca carbon irradiated in the presence of HO [•] radical
	C-0	Ceca carbon irradiated in the presence of all three radicals
	C-a	Ceca carbon irradiated in the air (without water)
Merck series	M	Original Merck carbon
	M-H [•]	Merck carbon irradiated in the presence of H [•] radical
	M-e ⁻ _{aq}	Merck carbon irradiated in the presence of e ⁻ _{aq}
	M-HO [•]	Merck carbon irradiated in the presence of HO [•] radical
	M-0	Merck carbon irradiated in the presence of all three radicals
Sorbo series	M-a	Merck carbon irradiated in the air (without water)
	S	Original Sorbo carbon
	S-H [•]	Sorbo carbon irradiated in the presence of H [•] radical
	S-e ⁻ _{aq}	Sorbo carbon irradiated in the presence of e ⁻ _{aq}
	S-HO [•]	Sorbo carbon irradiated in the presence of HO [•] radical
	S-0	Sorbo carbon irradiated in the presence of all three radicals
Witco series	S-a	Sorbo carbon irradiated in the air (without water)
	W	Original Witco carbon
	W-H [•]	Witco carbon irradiated in the presence of H [•] radical
	W-e ⁻ _{aq}	Witco carbon irradiated in the presence of e ⁻ _{aq}
	W-HO [•]	Witco carbon irradiated in the presence of HO [•] radical
	W-0	Witco carbon irradiated in the presence of all three radicals
	W-a	Witco carbon irradiated in the air (without water)

2.1.1. Effect of Gamma Irradiation on the Textural and Chemical Properties of ACs

All ACs were texturally and chemically characterized, as previously reported [69,75,85]. Table 3 compares textural characteristics between the original and irradiated ACs, and Table 4 exhibits the chemical properties of all ACs under study.

The textural characteristics of all irradiated ACs are highly similar to those of the original ACs (Table 3). However, their surface chemistry is modified in comparison to the original ACs according to the AC type and experimental conditions of the irradiation (Table 4). Examination of the role of water radiolysis-generated radical species in surface chemistry modifications shows that AC-H[•] has a lower pH_{PZC} in comparison with the corresponding original AC due to an increase in acidic groups and a decrease in basic groups (Table 4). However, no behavior pattern is observed for irradiated ACs in the presence of solvated electrons or HO[•] radicals.

Table 3. Effect of gamma irradiation on the textural characteristics of the ACs (adapted from [85] with permission of Elsevier, 2014).

Activated Carbon	S _{BET} ^a (N ₂) m ² /g	V _T ^b (N ₂) cm ³ /g	D _P ^c (N ₂) nm	V ₀ ^d (N ₂) cm ³ /g	S _{Ext} ^e (N ₂) m ² /g	V ₀ ^f (CO ₂) cm ³ /g
C	1294	0.65	2.02	0.55	82.68	0.34
C-A	1256	0.64	2.03	0.54	71.97	0.33
C-0	1248	0.63	2.04	0.53	73.78	0.33
M	1302	0.66	2.02	0.55	84.00	0.39
M-A	1286	0.64	1.99	0.54	75.54	0.38
M-0	1278	0.63	1.97	0.54	71.16	0.38
S	1143	0.57	2.02	0.49	53.84	0.29
S-A	1049	0.52	2.00	0.45	47.48	0.27
S-0	1031	0.52	2.03	0.44	53.22	0.28
W	815	0.40	1.97	0.35	20.39	0.26
W-A	798	0.39	1.97	0.35	23.06	0.25
W-0	794	0.39	1.97	0.35	20.14	0.24

^a Surface area determined from N₂ adsorption isotherms at 77 K. ^b Total pore volume calculated for P/P₀ = 0.99. ^c Mean pore width determined for a cylindrical model. ^d Micropore volume determined by the t method. ^e External surface area calculated by the t method. ^f Ultramicropore volume based on CO₂ adsorption isotherms at 273 K following the Dubinin–Radushkevich equation.

Table 4. Effect of gamma irradiation on the chemical properties of the ACs (adapted from [85] with permission of Elsevier, 2014).

ACs	pH _{PZC}	Acidic Groups ^a μeq/g	Basic Groups ^b μeq/g	E _g ^c eV
C	7.5 ± 0.2	240	409	3.65 ± 0.03
C-A	8.7 ± 0.2	107	657	3.25 ± 0.04
C-0	7.7 ± 0.2	246	462	3.04 ± 0.02
C-H•	3.1 ± 0.2	488	158	3.36 ± 0.02
C-e ⁻ _{aq}	7.2 ± 0.2	166	467	3.14 ± 0.02
C-HO•	7.7 ± 0.2	226	500	3.00 ± 0.02
M	10.0 ± 0.2	72	650	3.50 ± 0.02
M-A	10.7 ± 0.2	90	736	3.15 ± 0.04
M-0	9.3 ± 0.1	105	468	3.33 ± 0.02
M-H•	4.2 ± 0.2	453	150	3.13 ± 0.02
M-e ⁻ _{aq}	8.4 ± 0.2	68	389	3.20 ± 0.02
M-HO•	9.0 ± 0.2	48	431	3.23 ± 0.02
S	10.7 ± 0.1	108	1857	3.58 ± 0.02
S-A	11.9 ± 0.2	48	2376	3.28 ± 0.02
S-0	10.0 ± 0.2	87	1052	2.98 ± 0.02
S-H•	4.4 ± 0.2	333	433	3.63 ± 0.02
S-e ⁻ _{aq}	9.9 ± 0.2	68	968	3.16 ± 0.02
S-HO•	10.1 ± 0.2	88	1331	2.92 ± 0.02
W	8.4 ± 0.2	188	403	3.68 ± 0.02
W-A	9.2 ± 0.2	88	622	3.50 ± 0.04
W-0	7.1 ± 0.1	128	340	3.23 ± 0.02
W-H•	4.7 ± 0.1	448	186	3.35 ± 0.02
W-e ⁻ _{aq}	9.1 ± 0.2	100	558	3.15 ± 0.02
W-HO•	9.6 ± 0.1	50	688	3.10 ± 0.02

^a Determined by neutralization with NaOH (0.05 N). ^b Determined by neutralization with HCl (0.05 N). ^c Band gap values (E_g) of the activated carbons, calculated according to the Kubelka–Munk method.

2.1.2. Effect of the Surface Chemistry of ACs on DTZ Degradation by UV/AC System

DTZ is degraded by a photolytic process in the presence of the original and irradiated ACs (UV/AC) and in the absence of AC (direct photolysis). As an example, Figure 1 depicts the results obtained by direct photolysis and in the presence of the original ACs, showing a marked increase in their presence.

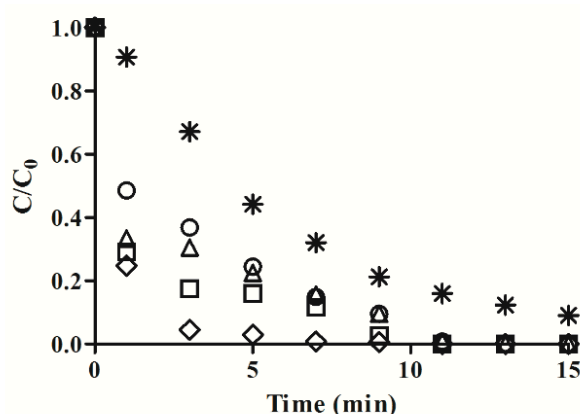


Figure 1. Sodium diatrizoate (DTZ) degradation by direct photolysis (*) and by the UV/AC system with the original activated carbons C (○), M (△), S (□), or W (◇). $[DTZ]_0 = 25 \text{ mg/L}$; $\text{pH} = 6.5$; $T = 298 \text{ K}$ (reproduced from [69] with permission of Elsevier, 2013).

The role of ACs in DTZ removal by the UV/AC system was explored by determining the “synergic effect” of the carbons, which was calculated by subtracting the adsorptive and photolytic contributions from the global removal percentage in the UV/AC system (Equation (1)) (Table 5).

$$\%S_{UV/AC} = \%D_{UV/AC} - \%D_{UV} - \%A_{AC} \quad (1)$$

where $\%S_{UV/AC}$ is the %DTZ removal due to the synergic effect of the presence of AC and UV radiation, $\%D_{UV/AC}$ is the total %DTZ removal by photocatalysis, $\%D_{UV}$ is the %DTZ degradation by direct photolysis, and $\%A_{AC}$ is the %DTZ removal by AC adsorption.

Table 5. Removal fractions and reaction rate constants for DTZ removal by UV/AC. $[DTZ]_0 = 25 \text{ mg/L}$; $\text{pH} = 6.5$; $T = 298 \text{ K}$ (reproduced from [69] with permission of Elsevier, 2013).

Activated Carbon	k_{OB} (15 min) min^{-1}	%UV Degradation (1 min)	%Removal by Adsorption (1 min)	%Removal by UV/AC (1 min)	%Synergic Removal (1 min)
C	0.47 ± 0.01	9.29	14.20	51.50	28.01
C-H•	0.75 ± 0.04	9.29	11.70	49.79	28.80
C-e ⁻ _{aq}	0.69 ± 0.03	9.29	11.60	44.61	23.72
C-HO•	1.05 ± 0.05	9.29	17.00	53.99	27.70
C-0	2.05 ± 0.00	9.29	12.90	87.09	64.90
M	0.53 ± 0.04	9.29	18.70	66.60	38.61
M-H•	1.06 ± 0.02	9.29	30.40	65.38	25.69
M-e ⁻ _{aq}	1.05 ± 0.04	9.29	0.86	65.04	54.89
M-HO•	0.93 ± 0.05	9.29	17.00	62.36	36.07
M-0	0.69 ± 0.04	9.29	12.40	53.05	31.36
S	0.59 ± 0.03	9.29	28.80	71.00	32.91
S-H•	0.42 ± 0.05	9.29	8.49	45.00	27.22
S-e ⁻ _{aq}	0.28 ± 0.02	9.29	9.07	32.49	14.13
S-HO•	1.03 ± 0.04	9.29	14.80	64.10	39.91
S-0	1.07 ± 0.02	9.29	7.67	47.00	30.04
W	1.42 ± 0.04	9.29	12.80	75.20	53.11
W-H•	1.02 ± 0.04	9.29	1.04	69.47	59.14
W-e ⁻ _{aq}	5.06 ± 0.06	9.29	1.02	100	89.69
W-HO•	5.26 ± 0.06	9.29	1.67	92.81	81.85
W-0	0.99 ± 0.01	9.29	8.23	62.87	45.35

As observed in Table 5, the largest adsorptive contribution to the total removal process is from carbon S and the smallest from carbon W. Nevertheless, carbon W has the greatest synergic effect on DTZ removal by the UV/AC system (>53% at 1 min of treatment).

With regard to the behavior of the irradiated ACs in DTZ photodegradation (Table 5), W-e⁻_{aq} and W-HO• obtain the highest rise in DTZ removal, which is not substantively increased by the sample treated with hydrogen atoms (W-H•). In addition, W-e⁻_{aq} and W-HO• make a markedly greater synergic contribution to the overall removal process at 1 min of treatment in comparison to the original carbon W (Table 5). Accordingly, irradiation of the AC increases its synergic activity, regardless of

the treatment applied (oxidizing or reducing agents). Chemical analysis of the treated carbons shows that both treatments increase the percentage of ester/anhydride groups in comparison to the original carbon. Results displayed in Table 5 show that the synergic activity of all ACs is increased by the gamma radiation treatment to varying degrees, with reaction rates that follow the order $W\text{-HO}^\bullet > W\text{-e}^-_{\text{aq}} > W > W\text{-H}^\bullet > W\text{-O}$ for carbon W, but $M\text{-H}^\bullet > M\text{-e}^-_{\text{aq}} > M\text{-HO}^\bullet > M\text{-O} > M$ for carbon M. Comparison of these results with the textural and chemical properties of the ACs revealed no general trend; however, the synergic activity is greater in the ACs with a higher percentage of surface oxygen, especially in those with a higher percentage of ester/anhydride groups and carbon atoms with sp^2 hybridization [69].

In order to investigate further the characteristics that affect AC photocatalytic activity, the bandgap energy of the samples was determined by diffuse reflectance spectroscopy. According to the results in Table 5, all of these ACs behave as semiconductors ($E_g < 4$ eV) and consequently as photoactive materials in the presence of UV radiation, and gamma irradiation reduces the E_g values of the materials. Finally, the best performance in the synergic effect is obtained with the W series, although their E_g values are not the lowest. This may be explained by the higher concentration of sulfur in carbon W than in the others because its presence increases the number of carbon atoms with sp^2 hybridization. This promotes the transit of electrons, which are the principal triggers of the photocatalytic process. An increased sp^2 hybridization is observed in the samples treated with gamma radiation, which would account for their improved behavior in DTZ photodegradation. The photocatalytic activity of the AC is therefore enhanced not only by a reduction in E_g values but also by an increase in carbon atoms with sp^2 hybridization of the material [69].

Figure 2 depicts a proposed action mechanism underlying photocatalytic DTZ removal in the presence of the ACs, based on the above findings. UV light photons falling on the ACs generate electron–hole pairs ($e^- \text{--} h^+$) by irradiating with sufficient energy to promote e^- from the valence (VB) to conduction (CB) band (reaction (2)). Accordingly, photogenerated e^- is spread throughout the graphene layers, reaching molecules of the adsorbed DTZ and oxygen. The electrons reduce the adsorbed O_2 to form $O_2^{\bullet -}$, which would react with the water molecule and produce oxidizing radical species that interact with the DTZ, contributing to its degradation (reactions (3)–(5)). Recombination of the e^- with h^+ is prevented by the presence of adsorbed oxygen (reaction (3)), permitting an interaction between a water molecule and free hole and enhancing the efficacy of the process. Positive holes are responsible for generating HO^\bullet radicals (reaction (6)).

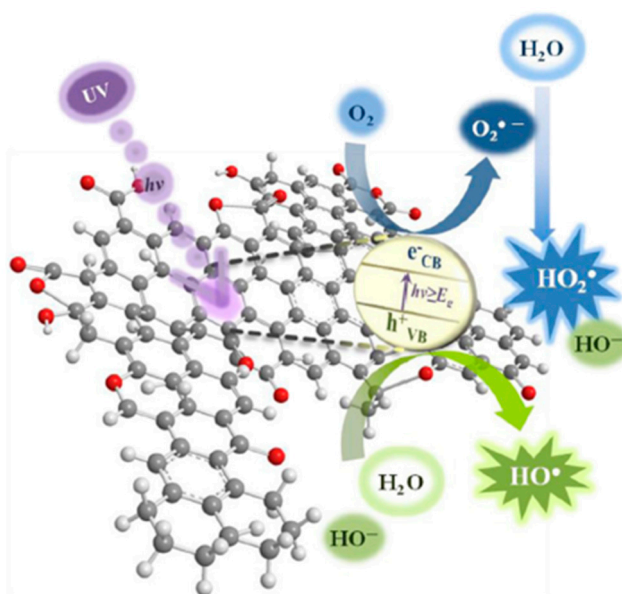


Figure 2. Action mechanism of activated carbons as photocatalyst in the presence of UV light (reproduced from [69] with permission of Elsevier, 2013).



2.1.3. Effect of the Type of Radiation in the Heterogeneous Photocatalysis Process Using ACs

The influence of radiation on the photocatalytic process was examined by determining variations in the concentration of DTZ by UV light and simulated solar radiation both in the absence and presence of ACs or TiO_2 [75]. The commercial AC W and its five irradiated carbons were used for this study (Table 4). Results obtained indicate that direct photolysis of DTZ is greater when UV radiation is used (Figure 3) due to the absorption spectrum of DTZ, which shows maximum absorbance in the range of 200–270 nm, while the emission wavelength of the low-pressure lamp is 257.7 nm. The reason for the low percentage of DTZ degradation by direct solar radiation is the minimal overlap between the emission spectrum of the Xe lamp of the solar photoreactor [75] and the absorption spectrum of DTZ.

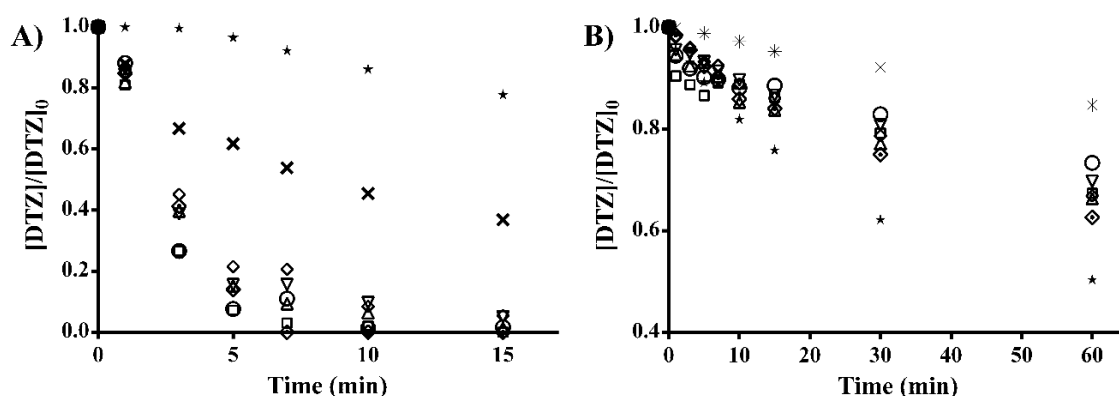


Figure 3. DTZ degradation by UV light and simulated solar radiation. (A) UV radiation: (×), direct photolysis; (★), UV/ TiO_2 system; UV/AC system with activated carbons W (○), W- H^{\bullet} (◻), W- e^-_{aq} (Δ), W- HO^{\bullet} (▽), W-0 (◇) y W-a (⊙). (B) Simulated solar radiation: (*), direct photolysis; (★), solar/ TiO_2 system; solar/AC system with activated carbons W (○), W- H^{\bullet} (◻), W- e^-_{aq} (Δ), W- HO^{\bullet} (▽), W-0 (◇). $[\text{DTZ}]_0 = 25 \text{ mg/L}$; $W_{\text{AC}} = W_{\text{TiO}_2} = 17 \text{ mg}$; $\lambda = 254 \text{ nm}$; $\text{pH} = 6.5$; $T = 298 \text{ K}$ (reproduced from [75] with permission of Elsevier, 2017).

The results obtained demonstrate the photoactive behavior of these ACs (W series) because the percentage of DTZ removed is higher than the degradation rate obtained by direct photolysis (using UV or solar radiation). An increased effect on DTZ degradation was also observed in the presence of ACs under UV radiation (Figure 3).

DTZ degradation by UV/AC and solar/AC systems was also compared with that obtained by the conventional utilization of TiO_2 as a photocatalyst. Results in Figure 3 show higher DTZ degradation with solar/ TiO_2 than with solar/AC systems, attributable to the major difference between the illumination intensity created by solar radiation (64.52 W/m^2) and that created by the UV radiation photoreactor (34.62 W/m^2) [86]. However, the degradation rates obtained by UV/AC systems are much higher than those obtained by UV/ TiO_2 system. This is because the presence of TiO_2 in the solution increases the flux of absorbed photons [87], generating more e^- - h^+ pairs and increasing the opportunity for e^- - h^+ recombination.

With regard to the photocatalytic activity of the carbon samples [75], the formation of electron holes, HO• radicals, and superoxide anions was demonstrated in both radiation systems, and the concentrations of superoxide anions and HO• radicals were found to depend on the AC surface chemistry. Results depicted in Figure 4 show an increase in the concentration of both superoxide anions and HO• radicals for a given amount of AC. As can be observed in Figure 4B, the formation rate of both oxidant species is enhanced with low amounts of AC. However, the formation rate of superoxide anions is markedly reduced with amounts >170 mg/L, while the formation rate of HO• radicals continues to rise. This may be because the formation of HO• radicals (reaction 6) leads to the formation of H⁺ on the surface of the AC, favoring reaction (7) and therefore shifting the equilibrium of reaction (8) towards the left. This results in reactions (9) and (10), which would explain the decreased concentration of superoxide anions and increased concentration of HO• radicals. The reduced concentration of superoxide anions may also be caused by the interaction between the species (reaction (11)) [88].

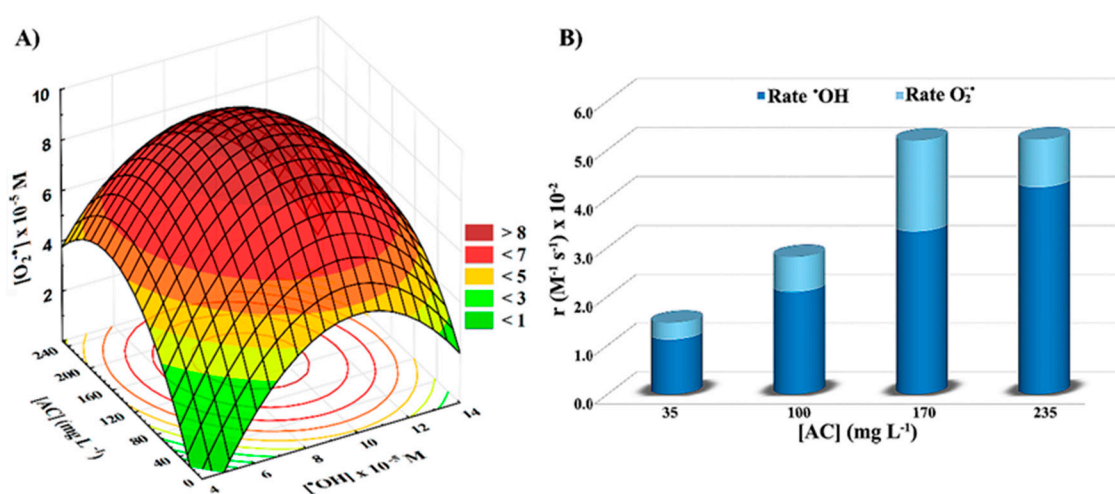
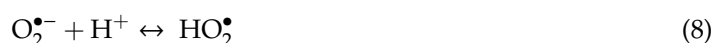


Figure 4. Variations in the concentration and formation rate of superoxide anions and HO• radicals in the UV/AC system as a function of AC concentration. (A) Variation in superoxide anion concentration as a function of HO• radical concentration and amount of AC; (B) variation in the formation rate of superoxide anions and HO• radicals as a function of the amount of AC. pH = 6.5; T = 298 K (reproduced from [75] with permission of Elsevier, 2017).

Dissolved oxygen plays a major role in photocatalytic processes [89]. Removal of dissolved oxygen from the solution was found to reduce percentage DTZ removal by the radiation/AC system [69,75] by favoring the e⁻-h⁺ recombination and thereby impeding superoxide anion and HO• radical formation. It was also observed that the presence of chemisorbed oxygen on the AC surface enhances the formation of radical species [75].

2.1.4. Effect of AC Surface Chemistry on the Photogeneration of Radical Species in UV/AC and Solar/AC Systems

The ACs under study share similar textural characteristics, but they have distinct surface chemistries (Tables 3 and 4) that may explain the differences observed in their behavior. Thus, the photogenerated concentrations of superoxide anion and HO• radical were found to depend on their surface chemistry [75]. In addition, a relationship was established for the first time between the E_g values of ACs and the main species photogenerated in the medium. In this way, HO• radical formation is favored by lower E_g values and superoxide anion formation by higher values. A relationship was found between photogenerated HO• radicals and DTZ degradation in the studied systems. Thus, percentage DTZ degradation is higher in the solar/TiO₂ system than in any solar/AC system because the concentration of HO• radicals is much higher in the solar/TiO₂ system than in the solar/AC systems.

2.2. Metal Carbon Aerogels

Metal carbon aerogels have a large number of environmental applications due to their easy preparation and their special textural, chemical, and electronic properties [90]. Thus, metal-carbon aerogels have proven highly effective as catalysts in the photooxidation of different water pollutants [60,61,72,74,77,79].

Carbon aerogels doped with transition metals (Co(II), Ti(IV) and Mn(II)) were prepared and characterized for the photooxidation of aromatic organic micropollutants in aqueous solution, using the naphthalenesulfonic acids 1-naphthalenesulfonic (NS), 1,5-naphthalenedisulfonic (NDS), and 1,3,6-naphthalentrisulfonic (NTS) [60,61] as model compounds. In addition, organic aerogels and xerogels doped with Fe, Co, or Ni were prepared, characterized, and used for the removal of the herbicide amitrole (AMT) in aqueous solutions [72]. More recently, organic xerogels doped with Ni [77,79] and Ru [74] were prepared, and their photoactivity in the degradation of certain pollutants was evaluated. Specifically, Álvarez et al. [77] studied the efficacy of a Ni organic xerogel to degrade AMT under UV irradiation and López-Ramón et al. [79] its capacity to degrade diuron (DRN) from water under simulated solar radiation, while Salazar-Rábago et al. [74] evaluated the photoactivity of xerogels doped with doses of Tris(2,2'-bipyridine) ruthenium(II) (RuBpy) in the degradation of chlortetracycline (CTC) under solar radiation.

Preparation of the aerogel samples has been reported elsewhere [91]. Briefly, metal-doped carbon gels were produced by polycondensating resorcinol (R) and formaldehyde (F) in water (W) using the corresponding metal acetates (Ag, Co, Mn, Fe, or Ni) [60,61,72,77,79], titanium tetrabutylammonium [60,61], and sodium carbonate [74] as catalyst precursors (C) and applying stoichiometric R/F, R/W, and R/C molar ratios. An identically prepared blank aerogel sample used carbonate sodium as catalyst [60,61,72,77,79]. Solutions were stirred to obtain homogeneous mixtures and then poured into glass molds and cured for a set time period. Next, the gel rods were cut into 5 mm pellets, immersed in acetone, and dried at room temperature [72,77,79] or 323 K for 3 days [74], yielding organic xerogels. The corresponding organic aerogels were formed by supercritically drying acetone exchange samples with CO₂. Finally, carbon gel samples were selected to obtain AC aerogels [60,72] and AC xerogels [72].

All samples were texturally and chemically characterized by gas adsorption (N₂ and/or CO₂ at 77 and 273 K, respectively), mercury porosimetry, determination of the pH of the point zero charge (pH_{PZC}), X-ray diffraction (XRD), and X-ray photoelectron spectroscopy (XPS), among others. Diffuse reflectance spectroscopy (DRS) was used to determine the band-gap energy of the samples. These techniques are described in detail elsewhere [53,92]. Table 6 lists the main features of the carbon xerogels and aerogels used in the study.

Table 6. Characteristics of carbon aerogels and xerogels (adapted from [60,72,73] with permission of Elsevier).

Sample	S _{BET} ^a	W ₀ ^b	V _m ^c	S _{CO2} ^d	V _{mic} ^e	V ₂ ^f	V ₃ ^g	pH _{PZC}	E _g
	m ² /g	cm ³ /g		m ² /g		cm ³ /g			eV
A	500	-	-	200	0.071	0.36	0.68	3.5	-
A-Co(II)-15	562	-	-	206	0.073	0.43	0.97	3.8	-
A-Ti(IV)-15	550	-	-	200	0.071	0.40	0.92	4.3	-
A-Mn(II)-15	554	-	-	210	0.075	0.41	0.95	4.2	-
A-Mn(II)-50	593	-	-	285	0.101	0.35	0.90	3.7	-
A-Mn(II)-200	646	-	-	321	0.114	0.28	0.86	3.2	-
A-Mn(II)-15C	880	-	-	701	0.250	0.43	0.86	7.5	-
X-Na	2	0.002	0.030	-	-	-	-	3.6	3.81
X-Co	68	0.031	0.194	-	-	-	-	3.6	3.78
X-Fe	27	0.012	0.089	-	-	-	-	3.5	3.74
X-Ni	103	0.040	0.295	-	-	-	-	3.4	3.66
A-Fe	388	0.173	0.678	-	-	-	-	3.1	3.75
A-Ni	407	0.185	0.717	-	-	-	-	3.6	3.69
XC-Fe	338	0.134	0.225	-	-	-	-	7.3	4.35
XC-Ni	382	0.144	0.230	-	-	-	-	7.0	4.16
AC-Fe	568	0.221	0.396	-	-	-	-	7.1	4.47
AC-Ni	637	0.249	0.371	-	-	-	-	6.9	4.44
XRF	<5	-	-	264	0.106	-	-	-	5.68
X50RuB	<5	-	-	204	0.082	-	-	-	-
X100RuB	<5	-	-	241	0.097	-	-	-	-
X150RuB	<5	-	-	253	0.102	-	-	-	0.98
X750RuB	<5	-	-	245	0.103	-	-	-	-

^a Surface area determined by N₂ adsorption at -196 °C. ^b Micropore volume from DR equation applied to N₂ adsorption isotherms at -196 °C. ^c Mesopore volume from N₂ adsorption isotherms at -196 °C. ^d Surface area determined by applying DR equation to CO₂ adsorption isotherms at 0 °C. ^e Micropore volume from DR equation applied to CO₂ adsorption isotherms at 0 °C. ^f Volume of pores with a diameter of 6.6–50 nm as determined by Hg porosimetry. ^g Volume of pores with a diameter higher than 50 nm as determined by Hg porosimetry.

Results obtained [60,61] showed that the addition of Co(II), Ti(IV), or Mn(II) has no significant impact on the textural or chemical properties of the aerogels (Table 6). However, the surface area of the aerogels is decreased, and their meso- and macroporosity is increased by the addition of increasing amounts of Mn (II) (R/C from 200 to 15) (Table 6). SN₂ >> SCO₂ in all samples, i.e., they have only a small proportion of narrow micropores ($\phi < 0.7$ nm) [93]. XPS analysis of the aerogels A-Co(II)-15, A-Ti(IV)-15, A-Mn(II)-15, A-Mn(II)-50, and A-Mn(II)-200 revealed a high concentration of surface oxygen (>20%), explaining the low pH values obtained and therefore the high surface acidity (Table 6). Activation of sample A-Mn(II)-15 with CO₂ markedly increases the microporosity of the new aerogel (A-Mn(II)-15C) and its surface basicity, largely attributable to the removal of oxygenated surface groups at the elevated temperatures reached during the activation process [94].

Results obtained from the direct photolysis of naphthalenesulfonic acids with UV radiation (254 nm) demonstrated that this method is not effective in removing these water pollutants [60,61]. However, photodegradation of these compounds can be achieved by irradiation with a medium-pressure Hg lamp, and a reduction in photodegradation rate and quantum yield values is observed with a higher number of sulfonic groups in the aromatic ring [60]. These groups withdraw electronic density from the aromatic ring of NTS, reducing reactivity during photooxidation [95]. The presence of the prepared aerogels (with Na, Co, or Ti) during irradiation does not significantly increase the NTS photodegradation rate [60,61]. However, the presence of Mn-doped aerogels during the photodegradation process increases the NTS removal rate, indicating that these aerogels possess the best photocatalytic activity, promoting the generation of oxidant species in the medium. In addition, the photocatalytic capacity of the Mn aerogel is increased at higher surface Mn(II) concentrations. Activation of Mn-doped aerogel increases its microporosity but does not affect its photocatalytic activity [60]. Comparison of NTS photodegradation results obtained with sample A-Mn-15 [60,61] with those obtained with TiO₂ show that TiO₂ is a more efficient photocatalyst in this process, possibly due to the greater UV radiation

absorption by TiO₂ (Figure 5). The NTS photooxidation rate is considerably increased by the addition of 5 mmol/g H₂O₂ to the system in the presence of A-Mn(II)-15 catalyst, but it becomes a potent HO• scavenger at a higher H₂O₂ dose [96]. Results obtained [60] confirm that the generation of HO• radicals governs NTS photooxidation. The following mechanism is proposed for NTS photooxidation in the presence of Mn carbon aerogels (reactions (12)–(20)) [97]:

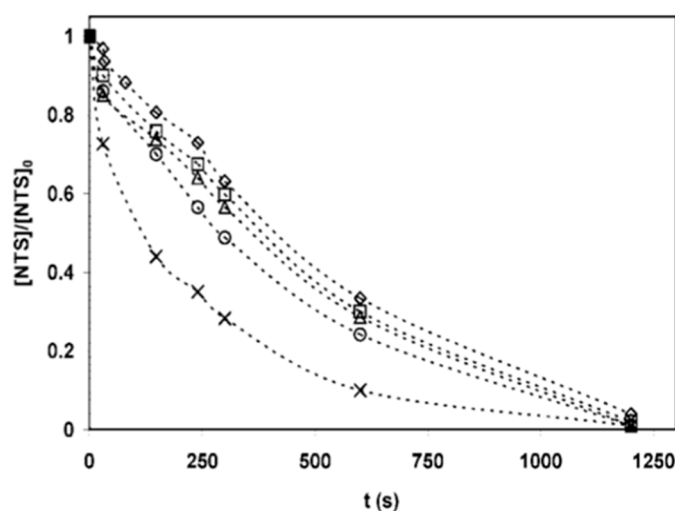
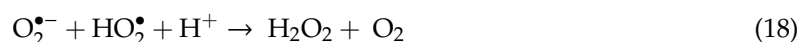
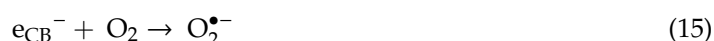
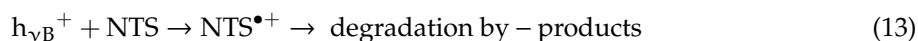
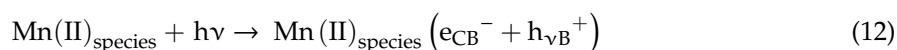


Figure 5. Photooxidation of 1,3,6-naphthalentrisulfonic acid (NTS) in the presence of metal-doped carbon aerogels. Medium-pressure lamp (MP). [NTS] = 25 μM, photocatalyst dose = 10 mg/L, pH 7, T = 25 °C: (◇) without aerogel, (◻) A-Co, (Δ) A-Ti, (○) A-Mn, (×) TiO₂ (reproduced from [61] with permission of American Chemical Society, 2008).

Organic gels doped with Fe, Co, and Ni were prepared to study the photoactivity of carbon xerogels and aerogels in the photodegradation of AMT from water under UV radiation [72]. Textural characterization of these xerogels and aerogels (see Table 6) showed that their porous texture depends on the metal salt used, with Ni and Co being the best catalysts in the polymerization process [98]. The micropore and mesopore volumes and surface area of the xerogels increase in the order: X-Na < X-Fe < X-Co < X-Ni. The surface area is higher for Fe and Ni aerogels (A-Fe and A-Ni, respectively) than for the corresponding xerogels, indicating that supercritically drying with CO₂ produces organic gels with a more developed porosity and surface area [99]. The carbonization of Ni and Fe aerogels and xerogels increases their microporosity and surface area but markedly reduces the mesoporosity of the aerogels (Table 6). The pH_{PZC} values (3.1–3.6) exhibited in Table 6 show the high surface acidity

of the xerogels and aerogels. As noted above, there is a large reduction in the surface acidity of the samples after carbonization due to the high temperatures used during this process, with a low oxygen content (Table 7) [60,94].

Table 7. Oxygen content and deconvolution of O1s XPS spectra of the carbon gel samples (%) (adapted from [72] with permission of Elsevier, 2016).

Sample	O %	–C=O/–OH 532.2 ± 0.2 eV	–C–O–C– 533.1 ± 0.2 eV	H ₂ O 535.1 ± 0.4 eV
X-Na	37.4	16.6	65.3	18.1
X-Co	37.6	18.0	66.2	15.8
X-Fe	38.1	20.4	60.1	19.5
X-Ni	32.0	24.2(28.4 ^a , 29.6 ^b)	51.2(49.2 ^a , 51.9 ^b)	24.6(22.4 ^a , 18.5 ^b)
XC-Fe	3.9	7.9	38.0	54.1
XC-Ni	7.9	9.6	36.6	53.8
A-Fe	36.4	19.9	51.1	29.0
A-Ni	33.9	22.6	46.4	31.0
AC-Fe	9.7	10.3	30.8	58.9
AC-Ni	8.5	11.7	33.7	54.6

^a At 45 min irradiation. ^b At 90 min irradiation.

The noncarbonized samples behave as semiconductor materials, with bandgap values <4 eV (Table 6). As shown in Tables 6 and 7, the X-Ni sample has a low E_g value and the highest percentage of –C=O/–OH groups (24.2%), because these groups can alter the electrical properties of materials, introducing “impurity” bands around the Fermi level and thereby reducing the energy between LUMO and HOMO orbitals [100].

Figure 6 depicts the results of AMT removal kinetics by direct photolysis with the UV/organic xerogel system. The AMT photodegradation rate markedly increases when the process is carried out in the presence of organic xerogel doped with transition metals. The reduction in AMT concentration during UV irradiation in the presence of these samples is complex, involving three processes: adsorption (k_{AD}), direct photolysis (k_{UV}), and the gel-induced synergic effect (k_{SE}) of the xerogel. Hence, AMT degradation in the UV/GEL system can be described mathematically by Equation (21):

$$-V_{UV/GEL} = -\frac{[dAMT]}{dt} = -(V_{UV} + V_{AD} + V_{SE}) = -(k_{UV} + k_{AD} + k_{SE}) \times [AMT] \quad (21)$$

The percentage removal due to the synergic effect (%SE_{UV/GEL}) was determined by subtracting adsorptive (%A_{GEL}) and photolytic (%AMT_{UV}) contributions from the total percentage removal (%AMT_{UV/GEL}) (Equation (22)):

$$\%SE_{UV/GEL} = \%AMT_{UV/GEL} - \%AMT_{UV} - \%A_{GEL} \quad (22)$$

These results indicate that $k_{UV/GEL}$ increases in the order: X-Na < X-Co < X-Fe < X-Ni, from $20.6 \times 10^{-3} \text{ min}^{-1}$ (X-Na) to $37.1 \times 10^{-3} \text{ min}^{-1}$ (X-Ni). The percentage removal (%AMT_{UV/GEL}) also increases in the same order, from 63.3% (X-Na) to 77.6% (X-Ni), after 45 min of irradiation. Finally, the highest percentage of synergetic degradation is obtained with the X-Ni sample (24.4%), related to its lowest E_g value (3.66 eV).

The reaction mechanism of AMT photooxidation in the presence of organic xerogels was investigated, conducting AMT degradation experiments to study the influence of the positive holes (h^+_{VB}) in the presence and absence of EDTA. Results obtained confirm that their photocatalytic role in AMT removal is completely inhibited by suppression of h^+_{VB} and that the xerogels act as photoactive materials. AMT degradation kinetics were also studied in the presence of tetranitromethane, showing that when organic xerogels are present during photooxidation, the concentration of superoxide radicals ($O_2^{\bullet-}$) is increased, favoring AMT degradation. Thus, the presence of xerogels during

AMT photooxidation promotes the generation of $O_2^{\bullet-}$ and HO^{\bullet} radicals via the photogeneration of electron-positive hole pairs, which can also oxidize and reduce some oxygenated groups on the xerogel surface [69] (Figure 7).

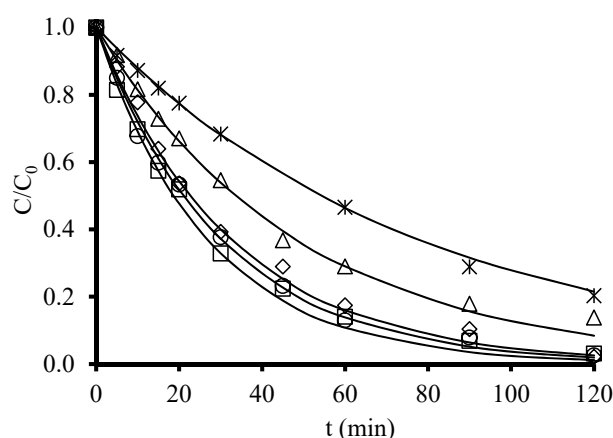


Figure 6. Removal kinetics of AMT at 25 °C with the UV/organic xerogel system as a function of treatment time. $[AMT]_0 = 0.30$ mM, $T = 25$ °C. (*) Direct photolysis; (Δ) X-Na; (\diamond) X-Co; (\circ) X-Fe; (\square) X-Ni (reproduced from [72] with permission of Elsevier, 2016).

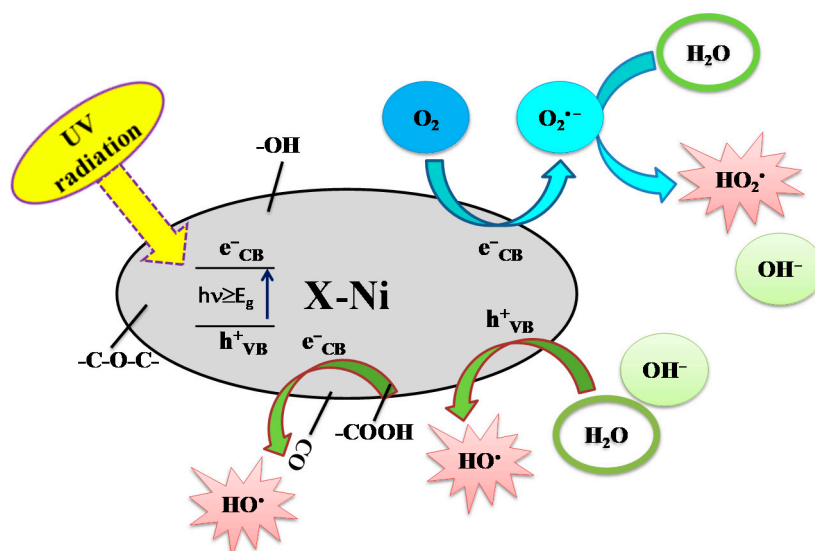


Figure 7. Mechanism proposed for the action of organic gels as photocatalysts (reproduced from [72] with permission of Elsevier, 2016).

Because the best results were obtained with the Ni xerogel, this sample was used in subsequent studies. Thus, the variation of TOC and medium toxicity during photocatalytic AMT degradation was studied under UV irradiation [77]. The rate of degradation is proportional to the X-Ni concentration up to 250 mg/L, but higher concentrations have no effect on the AMT photodegradation rate, attributed to (i) a reduction in active sites available for light absorption due to the greater aggregation of xerogel particles, lowering the photooxidation rate [101], and (ii) a decrease in the penetration of the medium by the light because of its dispersion by a large number of particles in suspension [101,102]. Hence [72], the main species in the photodegradation of AMT are $O_2^{\bullet-}$ and HO^{\bullet} radicals.

According to the results obtained, AMT photodegradation using X-Ni under UV radiation is influenced by the following factors: (i) high pH-dependency, being favored at pH 12 when AMT is in ionic form, and more HO^{\bullet} radicals are generated because there are more OH^- ions on the xerogel surface [103]; (ii) the presence of Cl^- , which behaves as a scavenger of h^+ and HO^{\bullet} radicals and therefore

reduces the AMT degradation rate (reactions (23) and (24)) [104]; (iii) the presence of organic matter, which behaves as a filter, reducing the light transmission and therefore the AMT removal [105]; (iv) the intensity of irradiated light on the solution, with a higher intensity enhancing the photogeneration of electron/hole pairs and the oxidation capacity of the system [106]; and (v) the water type, being most effective in ultrapure water free of competition for generated radicals from inorganic anions or natural organic matter [107]. Nevertheless, the toxicity is greater with longer irradiation in all types of natural water studied, suggesting that smaller byproducts are formed. Notably, the X-Ni catalyst shows adequate stability after being utilized for several cycles under optimal experimental conditions.



X-Ni sample was also tested as a photocatalyst to degrade DRN in an aqueous solution under solar radiation [79]. DRN is not very effective for direct photolysis under solar radiation because of its low aromaticity in comparison to other aromatic compounds studied [108]. The addition of X-Ni considerably enhances this photodegradation process (Figure 8). As found in the previous study [77], the photodegradation rate constant rises with a higher concentration of X-Ni, which increases the number of active surface sites for photocatalysis [108], up to a concentration of 4167–5000 mg/L. There is no increase in DRN degradation at X-Ni concentrations above 5000 mg/L, which may be explained by the two factors described above in relation to AMT photodegradation in the presence of the same xerogel under UV radiation [77,101,102]. The percentage of degradation and mineralization of DRN increases in the same order due to the greater concentration of (HO^\bullet and $\text{O}_2^{\bullet-}$) radicals at higher X-Ni doses. X-Ni also shows good stability after three consecutive cycles, losing less than 6% of its catalytic activity (Figure 8).

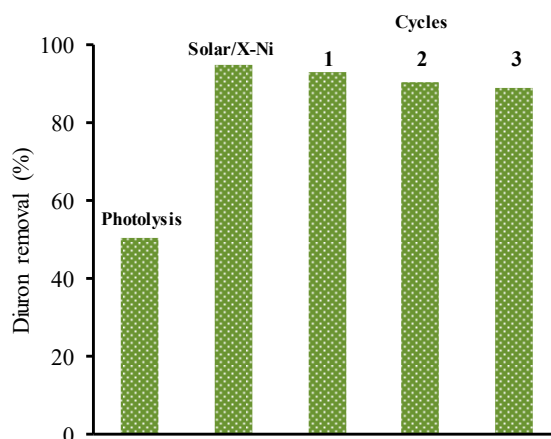


Figure 8. Diuron degradation efficacy after photolysis, heterogeneous photocatalysis, and reutilization cycles under the same experimental conditions. $T = 240$ min, $[\text{DRN}]_0 = 0.107 \times 10^{-3}$ mol/L, $[\text{X-Ni}] = 4167$ mg/L (reproduced from [79] with permission of Elsevier, 2019).

Finally, the study of RuBpy-doped organic xerogels (XRF) [74] showed the homogeneous presence of this coordination compound in the xerogel matrix; however, its presence has no effect on the morphological or textural properties of the xerogels, which all have a highly developed microporosity (Table 6). The addition of RuBpy in the XRF polymer matrix markedly reduces the bandgap energy of the xerogels and increases their capacity to generate electrons under solar irradiation in an aqueous solution.

The percentage CTC degradation by direct photolysis is 31.3% after 2 h of irradiation. However, the presence of RuBpy xerogels increases the CTC photodegradation rate up to a concentration of 500 mg/L (Figure 9). According to results obtained for the effect of radical scavengers on CTC degradation and the XPS results, the hydrated electrons (e^-_{aq}) generated by irradiation of the doped

xerogel centers migrate through this material, reacting with its functional groups and enhancing the generation of HO• radicals for CTC oxidation (reactions (25)–(27)).

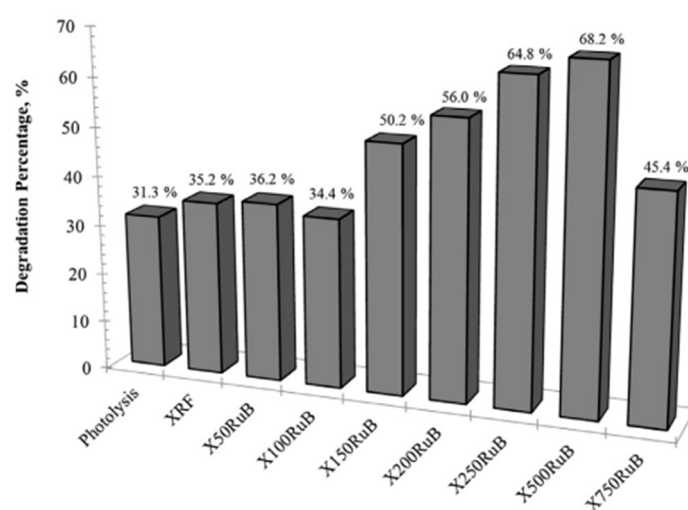
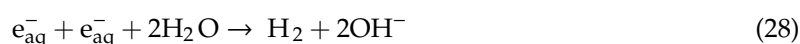
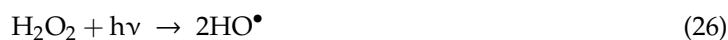
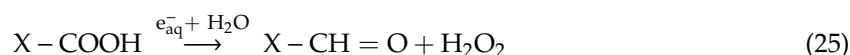


Figure 9. Percentage chlortetracycline (CTC) degradation by solar radiation/xerogel systems versus direct photolysis (reproduced from [74] with permission of Elsevier, 2016).

The photoactivity decreases at RuBpy concentrations above 500 mg/L (Figure 9) because the e_{aq}^- generated, favored at these higher concentrations, can be consumed according to reaction (28) [88].

These results indicate that xerogels doped with RuBpy do not behave as true photocatalysts for CTC degradation because of the changes in their chemical characteristics produced by irradiation, which diminishes the number of functional groups and leads to deactivation of the doped xerogels.

2.3. Iron-Doped Silica Xerogels

A novel research line was launched by the modification of silica xerogels [76,109,110] because of their particular physicochemical properties [111]. Fe(III)-doped silica xerogels (XGS) were investigated as photocatalysts, selecting tinidazole (TNZ) as a model compound for degradation under solar radiation [76]. The study used non-doped xerogels (XGS-BCO) and XGS doped with different concentrations of Fe(III) (XGS-Fe(III)-xM). Table 8 exhibits the characteristics of XGS-BCO and XGS-Fe(III)-0.4 M, with three different particle sizes.

Table 8. Textural properties of non-doped xerogels (XGS-BCO) and XGS-Fe(III)-0.4 M (reproduced from [76] with permission of Elsevier, 2018).

Sample	Surface Area S_{BET} (m^2/g)	Pore Volume V_{p} (cm^3/g)	Average Pore Diameter, D_{p} (nm)
XGS-BCO	645.92	0.668	4.140
XGS-Fe(III)-0.4 M-0.015 mm	630.28	0.350	2.588
XGS-Fe(III)-0.4 M-0.025 mm	587.69	0.337	2.633
XGS-Fe(III)-0.4 M-0.05 mm	587.37	0.331	2.256

With regard to the textural properties (Table 8), the S_{BET} of XGS-Fe(III)-0.4 M is lower when doped than non-doped (XGS-BCO) because the doping with Fe(III) reduces the pore diameter and volume, and the S_{BET} is smaller at higher Fe(III) concentrations and particle diameters. According to HRTEM analysis, iron is zoned in the contour of the particles and is present as akaganeite (β -FeOOH) [76].

The bandgap value decreases from 3.34 eV (XGS-BCO) to 2.32 eV (XGS-Fe(III)-0.4 M) due to the presence of delocalized states in the transition metals, thereby enhancing the generation of photodegraded electron hole-pairs [112]. Photoluminescence spectroscopy findings confirmed that the presence of Fe(III) strongly suppresses recombination of the photogenerated electron-hole pairs, with a consequent increase in photocatalytic activity [113].

A particle diameter of 0.025 mm was selected to study TNZ degradation under solar radiation. Figure 10 depicts the degradation results obtained by solar radiation and solar/XGS-Fe(III) systems. Similar results were obtained by direct photolysis (41.3%) and XGS-BCO (45.62%); however, 68.46% TNZ degradation was obtained with XGS-Fe(III)-0.4 M, and 98.38% with XGS-Fe(III)-0.4 M irradiated for 30 min before the treatment.

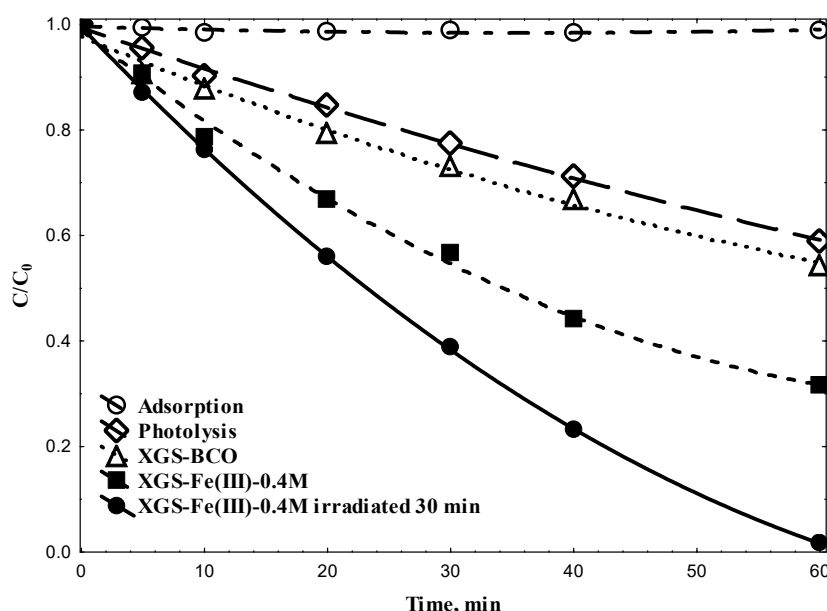


Figure 10. Degradation kinetics of tinidazole (TNZ). $[\text{TNZ}]_0 = 25 \text{ mg/L}$, $T = 25 \text{ }^\circ\text{C}$, $\text{pH}_{\text{in}} = 7$, XGS-BCO and XGS-Fe(III)-0.4 M = 1 g/L (reproduced from [76] with permission of Elsevier, 2018).

Table 9 describes the effects of different operating variables on TNZ photodegradation, showing: (i) greater degradation when XGS is doped with higher Fe(III) concentrations; (ii) no influence of particle size on rate constants, consistent with their similar textural properties (Table 8); (iii) a greater consumption of radicals at higher initial pollutant concentrations, reducing the degradation efficacy [114]; (iv) a marked increase in percentage TNZ degradation rate at higher photocatalyst doses; (v) a higher TNZ degradation rate at neutral pH, because HO^\bullet radicals, largely produced by β -FeOOH phase of XGS, are likely inhibited at acid pH (2) through the addition of H^+ ions, and also at basic pH (10), because the HO^\bullet radicals produced react with OH^- in the medium, generating HO_2^\bullet radicals and thereby reducing the degradation efficacy [114]; and (vi) significant changes in percentage TNZ removal due to the exposure of XGS-Fe(III)-0.4 M to solar radiation before the degradation process in comparison to unexposed XGS-Fe(III)-0.4 M.

Table 9. TNZ degradation under different operating conditions. T = 25 °C, time = 1 h. k values are fitted to a first-order kinetic model (adapted from [76] with permission of Elsevier, 2018).

[TNZ] ₀ mg/L	XGS g/L	[Fe(III)] ^b M	Particle Size nm	pH	k × 10 ³ min ⁻¹	Degradation %
25	0	0	0	7	8.63	41.03
25	1 ^a	0	0.025	7	9.66	45.62
25	1	9 × 10 ⁻⁵	0.025	7	9.83	45.91
25	1	0.2	0.025	7	12.27	51.37
25	1	0.4	0.025	7	18.85	68.46
25	1	0.4	0.015	7	18.91	69.01
25	1	0.4	0.050	7	17.73	68.25
15	1	0.4	0.025	7	25.37	78.81
15	0	0	0	7	14.24	56.07
40	1	0.4	0.025	7	7.00	35.75
40	0	0	0	7	7.90	30.89
25	0.5	0.4	0.025	7	9.30	43.46
25	5	0.4	0.025	7	28.74	83.54
25	1	0.4	0.025	2	9.40	42.88
25	1	0.4	0.025	10	12.75	53.54
25	0	0	0	2	6.37	32.46
25	0	0	0	10	8.65	41.26
25	1 ^c	0.4	0.025	7	62.94	98.38
25	1 ^d	0.4	0.025	7	40.19	92.47
25	1 ^e	0.4	0.025	7	28.72	83.53

^a XGS-BCO. ^b Refers to the concentration of Fe(III) in solution during chemical synthesis. ^c Irradiated for 30 min.

^d Irradiated for 60 min. ^e Irradiated for 90 min.

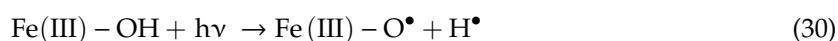
Quantification of the radicals generated during TNZ degradation in the solar/XGS-Fe(III)-0.4 M system showed that this photocatalyst degrades TNZ in an aqueous solution by promoting the formation of HO• and O₂^{•-} radicals. The byproducts are of lower molecular weight in comparison to TNZ and were found to have no toxic effects on HEK-293 cells [76].

Figure 11 depicts the proposed photocatalytic mechanism of XGS-Fe(III)-0.4 M under solar radiation. Accordingly, in the photocatalytic process with iron oxy-hydroxide, HO• can be generated by the following mechanisms (reactions (29)–(35)):

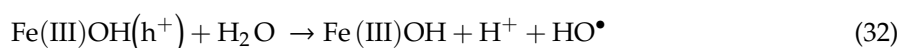
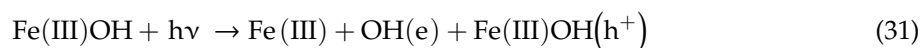
- (1) Photoredox reaction between OH groups on the catalyst surface and the iron.

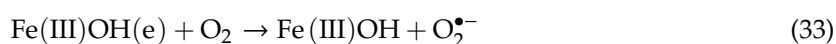


- (2) Formation of Fe(III)–O• due to the presence of Fe(III), which may induce the generation of HO• and H• radicals.



- (3) Generation of electron–hole pairs (e⁻-h⁺) by photons from the solar light that reaches the catalyst (reaction (31)); contact of the photogenerated electrons with pollutant or O₂ molecules would reduce them to O₂^{•-} radicals, which react with water molecules and produce more radical species to enhance TNZ degradation (reactions (32) and (33)) [115].





- (4) O_2 reduction by photogenerated electrons (e^-_{CB}) on the XGS-Fe(III) surface via the conduction band, which can form $\text{O}_2^{\bullet-}$ for action in reactions (34) and (35), contributing to TNZ degradation [116].

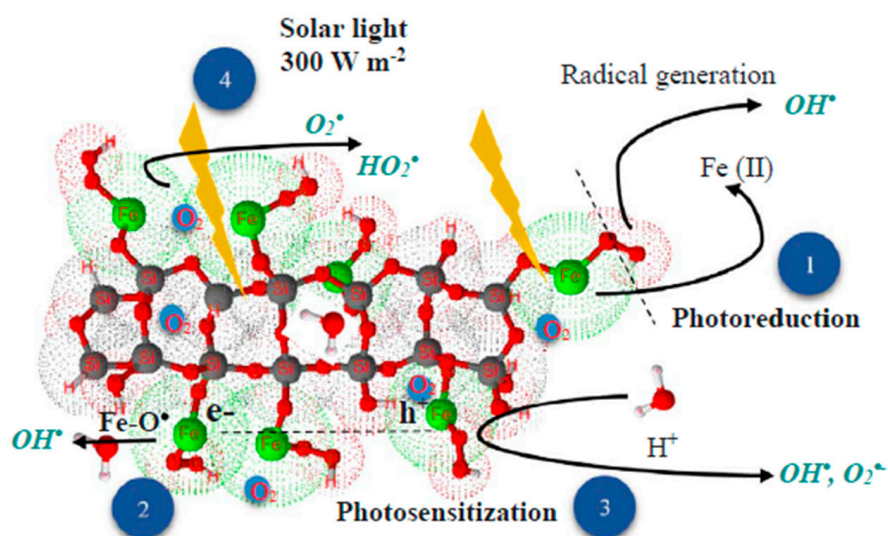


Figure 11. Proposed mechanism for TNZ degradation with XGS-Fe(III)-0.4 M photocatalyst under solar irradiation in aqueous solution (reproduced from [76] with permission of Elsevier, 2018).

XGS-Fe(III)-0.4 M can only be utilized once, given that the percentage degradation after four cycles is lower than the percentage achieved by direct photolysis, attributable to the absence of OH surface groups and the presence of Fe(II) in reutilized samples [117]. However, although XGS-Fe(III)-0.4 M does not behave as a true photocatalyst, its utilization is viable because it is inexpensive, readily synthesized, and easy to handle.

2.4. Ruthenium Metal Complexes

The development of photosensitizers to enhance sunlight photooxidation is a cutting-edge research line because of the possibility of obtaining more economically sustainable technologies. A large number of transition metal–organic complexes (MOCs) have been studied as photosensitizers due to their photochemical properties [118].

Ru(II) complexes with ligands derived from 2,2'-bipyridine or 1,10 phenanthroline are ideal for utilization as photosensitizers due to their: (i) high light absorption in the visible region of the spectrum; (ii) efficiency (nearly 100%) to transform from ground-state to excited triplet state, (iii) long half-life in an excited state, and (iv) elevated quantum performance in producing singlet oxygen ($^1[\text{O}_2]^*$), which behaves as an oxidizing agent [118,119].

The role of $^1[\text{O}_2]^*$ in the degradation of the antibiotic chlortetracycline (CTC) by direct and indirect photooxidation under solar radiation was evaluated to explore the mechanism of action of the photosensitizer and the CTC degradation pathway. Three ruthenium MOCs, cis-Bis (2,2'-bipyridine) dichlororuthenium(II) hydrate (Ru2B), tris-(2,2'-bipyridine) ruthenium(II) chloride hexahydrate (Ru3B),

and tris-(1,10 phenanthroline) ruthenium(II) chloride hydrate (Ru3P) were used as photosensitizers to promote the generation of $^1[\text{O}_2]^*$ in indirect photooxidation. Photodegradation experiments in a solar simulator were used to determine the effect on percentage CTC degradation of the initial CTC concentration, photosensitizer type, and solution pH [73].

Table 10 exhibits the results of CTC degradation by direct photolysis under different operating conditions. CTC photooxidation follows first-order kinetics, and an increase in CTC concentration reduces the maximum percentage degradation (M%Deg) and rate constant ($k_{\text{ap},\text{F}}$), attributed to a reduction in the radiant energy absorbed by each pollutant molecule.

Table 10. Chlortetracycline (CTC) photolysis under different operating conditions: kinetic parameters and maximum percentage degradation (adapted from [73] with permission of Elsevier, 2016).

$C_{\text{CTC}0}$ mg/L	pH_{in}	M%Deg	$K_{\text{ap},\text{F}} \times 10^2$ min^{-1}
15	7	25.29	0.36
25	7	21.74	0.29
35	7	16.58	0.16
25	2	9.00	0.27
25	11	44.39	5.44

Figure 12a displays the concentration decay curves for CTC degradation with Ru(II) MOCs, showing that the degradation rate is increased by adding Ru3B and Ru3P complexes, obtaining a maximum percentage degradation of 66.53 and 55.21%, respectively. These two complexes produce, respectively, 5.8- and 5.4-fold higher degradation rates in comparison to direct photolysis under the same experimental conditions (Tables 10 and 11). However, the presence of the Ru2B complex inhibits the M%Deg and degradation rate (Figure 12a). According to the results depicted in Figure 12b, the rate constant and M%Deg increase proportionally to the ability of MOCs to react with photons in the solution and transfer the energy to other species there. The highest increase in rate was observed with Ru3B, attributable to its higher molar absorption coefficient [73].

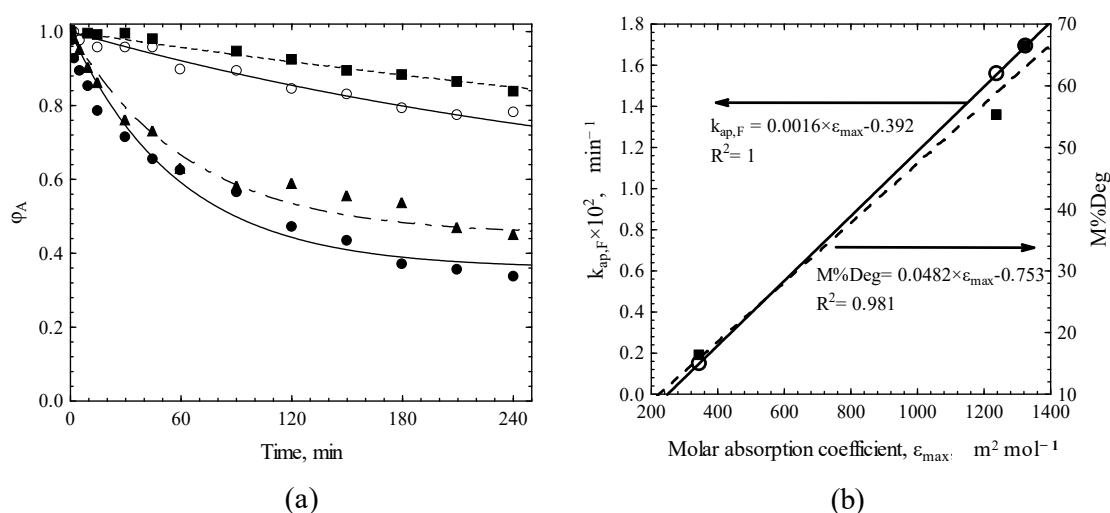
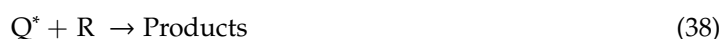


Figure 12. (a) CTC degradation with Ru(II) transition metal–organic complexes (MOCs). (○) Photolysis; (■) Ru2B; (●) Ru3B; (▲) Ru3P. $C_{\text{CTC}0} = 25$ mg/L, $C_{\text{MOC}} = 0.0134$ mM, $\text{pH} = 7$ and $T = 298$ K. (b) Correlation of kinetic constant (○) and M%Deg (■) with molar absorption coefficient. Lines represent the linear fit of the data (reproduced from [73] with permission of Elsevier, 2016).

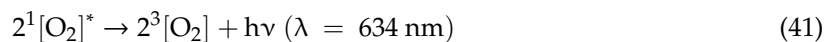
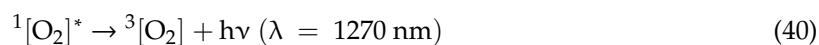
Table 11. Operating conditions, kinetic parameters, and maximum percentage degradation by CTC photodegradation sensitized with MOCs ($C_{CTC0} = 25$ mg/L) (adapted from [73] with permission of Elsevier, 2016).

MOC	C_{MOC} mM	pH _{in}	M%Deg	$K_{ap,S} \times 10^2$ min ⁻¹
Ru2B	0.0134	7	16.19	0.15
Ru3B	0.0134	7	66.53	1.69
Ru3P	0.0134	7	55.21	1.56
Ru3B	0.0067	7	59.31	1.12
Ru3B	0.0268	7	72.82	3.49
Ru3B	0.0134	2	49.99	1.59
Ru3B	0.0134	11	51.50	10.02

The Ru3B complex was selected to study the effect on CTC photodegradation of sensitizer dose. Tables 10 and 11 show that the rate constant for Ru3B-assisted CTC degradation is 3.9-, 5.8-, and 12-fold faster in comparison to the rate constant for direct photolysis. There is also an increase in M%Deg at higher Ru3B complex concentrations because they favor and enhance the transfer of energy to molecules in the system and because the reaction of the excited molecules with other chemical species can produce degradation byproducts (Equations (36)–(39)).



Results in Table 11 show the effect of solution pH on CTC photodegradation in the presence of Ru3B. The photosensitized degradation rate is highly pH-dependent, as also found for direct photolysis (Table 10). A rise in solution pH from 2 to 7 and 11 produces a 1.1- and 6.3-fold increase in the rate constant, respectively. Comparison of M%Deg in direct (Table 10) versus sensitized CTC photolysis (Table 11) shows that the presence of Ru3B produces a significant increase in M%Deg at pH values of 2 and 7, but a minimal increase at pH 11. The reduced Ru3B efficacy at pH 11 can be explained by i) interference between CTC and degradation byproducts produced by oxidizing species formed from Ru3B [120,121] and ii) the recombination of oxidizing species such as HO[•] and ¹[O₂]^{*} through reactions (40)–(43).



The capacity of the Ru3B complex to enhance ¹[O₂]^{*} formation in aqueous solution makes a significant contribution to CTC degradation, as demonstrated by the proportional decrease in CTC degradation rate with lower levels of dissolved oxygen. Figure 13 depicts the proposed mechanism of action of Ru3B in CTC photodegradation. Ru3B plays a major role as a reaction catalyst because it returns to its ground-state after participating in CTC degradation. According to high-resolution mass spectrometry analysis, degradation byproducts are produced by reduction–oxidation processes and the loss of functional groups.

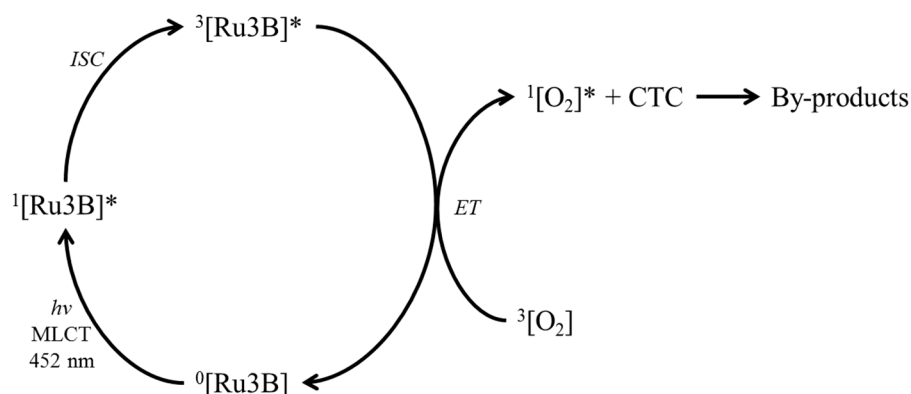


Figure 13. Reaction scheme of Ru3B-sensitized CTC photooxidation (reproduced from [73] with permission of Elsevier, 2016).

2.5. rGO Metal Oxide Composites

Graphene/metal oxide composites have attracted interest in the field of environmental remediation and water treatment because of their exceptional properties [122]. Reduced graphene oxide (rGO), a derivative of graphene oxide, is highly effective for photocatalytic reactions. In this way, rGO has been combined with different metal oxides (TiO_2 , ZnO , Cu_2O , Bi_2WO_6 , etc.) and found to be a very effective photocatalyst for the degradation of different pollutants from water and to prevent corrosion and leaching of the metal oxide nanoparticles in water [80,81,123]. A series of rGO/ TiO_2 [81] and rGO/Bi composites [80] with different rGO contents were exhaustively characterized, and their structural, chemical, and electronic properties were compared with their photocatalytic activity in the degradation of organic pollutants in aqueous solution.

Table 12 summarizes results for the textural characterization and bandgap energy of the above composites. TiO_2 has higher S_{BET} , V_0 , and $V_{0.95}$ values in comparison to P25, possibly due to the smaller size of TiO_2 nanoparticles, as observed in XRD analysis [81]. The addition of rGO sheets hinders the agglomeration of TiO_2 particles and augments the surface area and pore volume of % rGO- TiO_2 composites. The surface area and porosity are larger in rGO- TiO_2 versus rGO-P25 composites, whereas the surface area of % rGO/Bi composites (range, 17–26 m^2/g (Table 12) indicates that these materials are not porous. The larger surface area of the composites in comparison to the original Bi salt is attributable to the addition of GO, which improves the dispersion of the salt on the GO surface.

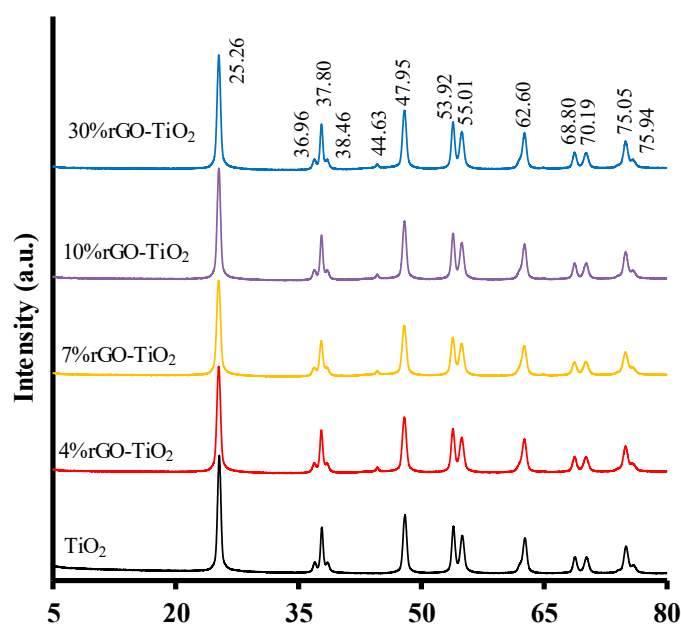
Electronic properties of the composites were studied by diffuse reflectance UV–vis spectroscopy, calculating the E_g value with the equation of Kubelka–Munk [72]. Table 12 exhibits the bandgap energy for TiO_2 , rGO- TiO_2 , and rGO/Bi samples, showing that the E_g decreases from 3.20 eV for TiO_2 to 2.55 eV for 30% rGO- TiO_2 and is narrower at higher % rGO values. However, the E_g results for rGO/Bi composites show a significant increase with higher % rGO to a maximum of 35%, followed by a decrease at a higher % rGO. These findings show that the rGO content influences the optical properties of TiO_2 and Bi_2O_3 , attributable to the formation of Ti–O–C and Bi–O–C bonds, respectively, during hydrothermal treatment of the composites, similar to results obtained for other materials [124].

The crystallographic nature of the composites was studied by XRD, and Figure 14 depicts the XRD patterns for synthesized TiO_2 nanoparticles and % rGO- TiO_2 composites. Peaks of 2θ at 25.26° and 47.95° for TiO_2 confirm its anatase structure, and the absence of peaks assigned to rutile indicate that it is in the pure anatase phase. The complete disappearance of the peak at 10.78° for GO in all samples suggests that GO is successfully converted to rGO in the final composites [124]. The mean crystal size is smaller in rGO/ TiO_2 composites (range, 19.7–17.6 nm) than in TiO_2 .

Table 12. Textural characteristics and bandgap energy (E_g) of rGO/metal oxide catalysts (adapted from [80,81]).

Sample	S_{BET}^a m ² /g	V_0^b cm ³ /g	$V_{0.95}^c$ cm ³ /g	E_g eV
TiO ₂	81.5	0.030	0.375	3.20
4% rGO-TiO ₂	89.1	0.032	0.289	3.09
7% rGO-TiO ₂	97.7	0.036	0.242	2.75
10% rGO-TiO ₂	106.3	0.039	0.282	2.63
30% rGO-TiO ₂	141.1	0.051	0.273	2.55
P25	57.0	0.020	0.138	-
4% rGO-P25	62.0	0.023	0.157	-
7% rGO-P25	66.8	0.024	0.171	-
10% rGO-P25	71.4	0.026	0.190	-
30% rGO-P25	115.9	0.043	0.236	-
Bismuth subnitrate	0.27	-	-	-
5% rGO/Bi	26	-	-	3.51
10% rGO/Bi	17	-	-	3.57
20% rGO/Bi	20	-	-	3.73
30% rGO/Bi	21	-	-	3.76
35% rGO/Bi	21	-	-	3.76
40% rGO/Bi	20	-	-	3.33
50% rGO/Bi	21	-	-	3.04

^a Surface area determined by N₂ adsorption at −196 °C. ^b Micropore volume from DR equation applied to N₂ adsorption isotherms at −196 °C. ^c Total pore volume from N₂ adsorption isotherms at −196 °C and 0.95 relative pressure.

**Figure 14.** XRD patterns for rGO-TiO₂ composites (reproduced from [81]).

XRD patterns in Figure 15 show marked changes in 5% rGO/Bi composite when Bi salt is added and GO is reduced. The mean crystal size of the 5% rGO/Bi sample is 17.9 nm. This series of composites show a reduction in main peak intensity with higher % rGO, reflecting the decrease in composite crystallinity.

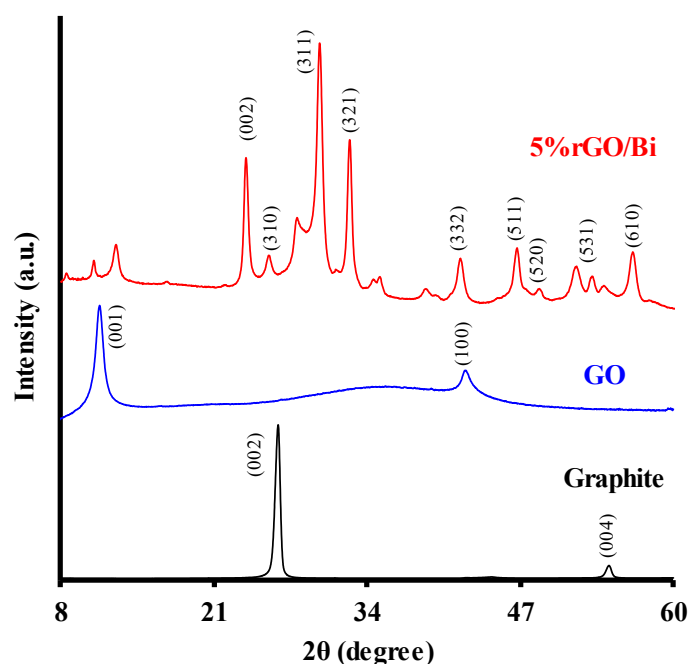


Figure 15. XRD patterns of graphite, graphene oxide, and 5% rGO/Bi (reproduced from [80]).

FTIR spectra of TiO_2 and rGO- TiO_2 composites indicate the presence of Ti-O-Ti bonds in TiO_2 and a combination of Ti-O-Ti and Ti-O-C vibrations in composites (peaks below 1000 cm^{-1}), attributable to chemical interactions between TiO_2 and rGO. FTIR spectra of P25 and rGO-P25 composites show similar results [81]. Raman spectra of rGO- TiO_2 composites indicate the persistence of the structure of rGO in the composites and show the formation of Ti-O-C on their surface. The I_D/I_G ratio increases in the order $\text{GO} < \text{rGO} < \text{rGO-TiO}_2$, indicating a reduction in the sp^2 domains formed during the hydrothermal reaction [124]. The smallest increase in this ratio is observed for the 7% rGO- TiO_2 composite. Comparison of XPS findings between rGO- TiO_2 composite materials and GO reveals an increased percentage of C=C and a reduced percentage of oxygenated groups, possibly attributable to the nucleation and growth of TiO_2 nanoparticles in GO sheets, in which C-O groups are consumed and partially reduced to C=C [125]. Finally, results also show a higher Ti/C ratio in 7% rGO- TiO_2 than in the other composites, indicating that rGO sheets are better dispersed in the TiO_2 matrix.

FTIR results for 5% rGO/Bi reveal a major reduction in the stretching vibration of C=O groups, confirming the GO reduction. In this case, peaks below 1000 cm^{-1} can be assigned to metal-oxygen vibrations, showing that Bi is well-functionalized on the rGO surface [80]. Raman spectra results for 5% rGO/Bi composite also indicate that GO in rGO/Bi sample is well deoxygenated and reduced. XPS results for 5% rGO/Bi show an increase in sp^2 C after the synthesizing process (from 29% for GO to 57.3% for the composites), confirming that GO reduction promotes the recovery of sp^2 -hybridized carbon structures.

% rGO- TiO_2 composites were used as photocatalysts for ethylparaben (EtP) degradation from water under UV radiation [80]. Direct photolysis of EtP under UV radiation alone achieves 61.5% degradation after 40 min of irradiation (Table 13).

The efficacy of catalytic EtP photodegradation decreases in the following order: 7% rGO- $\text{TiO}_2 > 4\%$ rGO- $\text{TiO}_2 > 10\%$ rGO- $\text{TiO}_2 > \text{TiO}_2 > 30\%$ rGO- $\text{TiO}_2 > \text{UV}$ (Table 13), showing that the presence of GO in TiO_2 composites favors EtP photodegradation. There is always a higher percentage degradation of EtP than of TOC (Table 13); therefore, the catalytic treatment does not mineralize all of the degraded pollutants, producing byproducts of lower molecular weight than EtP. There is a rise in photocatalytic activity when the % rGO increases from 4 to 7% and a decline when it increases to 10%, with an even greater decline for the 30% rGO- TiO_2 composite, which has lesser activity than that of TiO_2 . Among the rGO/ TiO_2 composites, 7% rGO/ TiO_2 has the smallest crystal size (17.6 nm) and the lowest I_D/I_G ratio

(0.95). More active sites are exposed to light when the crystal size is smaller, while a lower I_D/I_G ratio indicates a larger proportion of C atoms with sp^2 hybridization, favoring electronic conductivity. The photocatalytic activity of commercial P25 (anatase and rutile) is lower than that of the prepared TiO_2 (pure anatase), which may result from the larger surface area (Table 12) and smaller crystal size of TiO_2 in comparison to P25. For this reason, rGO-P25 composites are less active to photodegrade EtP in comparison to the corresponding rGO- TiO_2 composites (Table 13).

Table 13. Experimental results of ethylparaben (EtP) photodegradation under UV radiation in the presence of prepared rGO- TiO_2 composites $[EtP]_0 = 0.30 \times 10^{-3}$ mol/L, $[catalyst]_0 = 0.7$ g/L (adapted from [81]).

Sample	$t_{1/2}$ ^a min	$t_{90\%}$ ^b min	K ^c min^{-1}	EtP _{40 min} ^d %	TOC _{40 min} ^e %
UV	30.2	100.4	0.023	61.5	14.0
TiO_2	22.4	75.2	0.031	72.5	21.8
4% rGO- TiO_2	10.4	34.4	0.067	95.4	44.7
7% rGO- TiO_2	7.2	23.9	0.096	98.6	56.6
10% rGO- TiO_2	17.2	57.4	0.040	82.4	34.5
30% rGO- TiO_2	28.9	96.1	0.024	60.7	24.9
P25	28.1	93.3	0.025	64.5	-
4% rGO-P25	21.9	72.9	0.032	74.4	-
10% rGO-P25	34.5	114.6	0.020	53.3	-

^a Time required to halve the initial concentration of EtP. ^b Time required to degrade 90% of the initial concentration of EtP. ^c Degradation rate constant. ^d Percentage degradation after 40 min. ^e Percentage mineralization after 40 min.

Table 14 exhibits the results of the photocatalytic degradation of sulfamethazine (SMZ) under solar radiation in the presence of rGO/Bi composites. SMZ is not degraded in the absence of photocatalyst, while SMZ degradation is highest with 5% rGO/Bi and then decreases at higher percentages of rGO, when rGO particles can act as recombination center or cover active sites on the Bi_2O_3 surface through the aggregation of rGO/Bi composites, blocking light to the surface of composites [126]. The 5% rGO/Bi catalyst retains practically all of its activity after three photodegradation cycles, with no morphological or structural changes. Finally, the cytotoxicity study showed greater cell viability for SMZ photodegradation byproducts obtained in the presence of 5% rGO/Bi under solar radiation than for the original SMZ.

Table 14. Sulfamethazine (SMZ) degradation parameters for the different rGO/Bi composites (from [80]).

% rGO	Degradation Rate min^{-1}	% Degradation (2 h)
5	0.030	100
10	0.018	88
20	0.006	67
30	0.006	63
35	0.006	51
40	0.006	62
50	0.004	44

3. Catalysts Used in Pollutant Ozonation

Advanced oxidation processes have been developed to increase the efficacy of ozone treatment based on the generation of HO^\bullet radicals [127,128]. Solid catalysts have been proposed to increase the extent of ozonation [129,130]. ACs, metal-doped carbon aerogels, and basic treated zeolites were studied.

3.1. Activated Carbons

AC is a promising ozonation catalyst because of its chemical and textural properties and low cost [39,131]. The following groups of AC samples were studied for this purpose: (i) commercial ACs, (ii) ozonized ACs, (iii) nitrogen-enriched ACs, and (iv) ACs from petroleum coke.

The commercial ACs studied [40] were Filtrasorb 400, Sorbo, Merck, Ceca GAC, Ceca AC40, Norit, and Witco, whose characteristics are reported in Table 15.

Table 15. Characterization of activated carbons (reproduced from [40] with permission of Elsevier, 2002).

Activated Carbon	SN ₂ ^a m ² /g	V ₂ ^b cm ³ /g	V ₃ ^c cm ³ /g	pHPZC	Acid Groups ^d μeq/g	Basic Groups ^e μeq/g	Ash %
F400	1075	0.11	0.26	7.91	234	570	6.6
Sorbo	1295	0.06	0.37	9.42	88	1713	5.9
Merck	1301	0.09	0.26	7.89	114	582	5.2
Ceca GAC	966	0.13	0.16	6.83	323	99	12.0
Ceca AC40	1201	0.07	0.32	5.29	438	102	8.3
Norit	968	0.10	0.42	9.18	139	2050	4.8
Witco	808	0.04	0.05	6.85	183	253	0.3

^a Apparent surface area determined applying the BET equation to N₂ adsorption isotherm. ^b Volume of pores with a diameter of 50 to 6.6 nm. ^c Volume of pores with a diameter above 50 nm. ^d Determined by NaOH (0.1 N) neutralization. ^e Determined by HCl (0.02 N) neutralization.

The highest ash content (12%) was observed in Ceca GAC carbon and the lowest (0.3%) in Witco carbon (Table 15). High Fe (6.32%) and Al (8.41%) contents were found in Filtrasorb 400 ash, while Norit and Sorbo have low Fe and Al contents, but a substantive proportion of Mg and Ca (9–10% each). A high P content (4.11%) was observed in Ceca GAC alone. Ti was detected in Filtrasorb 400 and Merck ash samples at a concentration of ≈1% and Mn was found in Norit ashes at 0.25% and in Sorbo ashes at 0.13%. These metals often serve as catalysts in oxidation processes. Thus, Ti is favored as a catalyst in photocatalysis [132], and low concentrations of MnO₂ were used by Ma and Graham [33] to enhance chlorobenzene degradation by ozone.

Figure 16 shows the experimental results of NTS ozonation in the presence of the ACs, which all increase the ozonation rate. Sorbo, Norit, and Ceca GAC carbons produce a major increase in NTS degradation rate, whereas Witco AC has a lower effect. The higher NTS ozonation rate in the presence of these ACs may be attributable to an increased HO• concentration. The ozone-NTS direct reaction constant is 6.72 M⁻¹ s⁻¹, whereas the indirect reaction (free radical reaction) constant is 3.7 × 10⁹ M⁻¹ s⁻¹. Therefore, the radical reaction is more effective in oxidizing NTS. Similar results were obtained when these ACs were used in the ozonation of nitroimidazoles and surfactants [56,57,62].

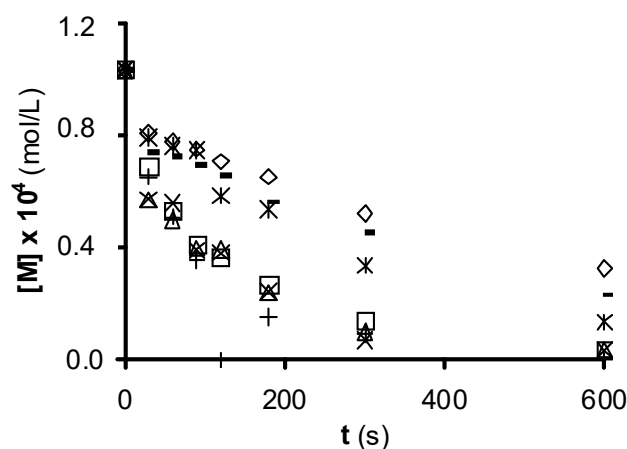


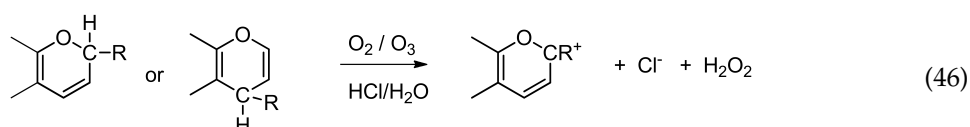
Figure 16. 1,3,6-naphthalentrisulfonic (NTS) ozonation in the presence of commercial activated carbon. (◇), without carbon; (○), Filtrasorb 400; (Δ), Merck; (◻), Ceca GAC; (*), Ceca AC40; (☆), Norit; (+), Sorbo; (-) Witco (reproduced from [50] with permission of John Wiley and Sons, 2003).

The ACs with the highest pH_{PZC} values and concentrations of basic surface groups produce the greatest increase in NTS ozonation rate (Table 15); however, this rate is not clearly related to the SN_2 of the AC. The most effective carbons to degrade NTS (Sorbo and Norit) have the largest volumes of macropores (Table 15), which behave as transport pores and favor the access of ozone to the carbon surface, reducing diffusion limitations. In this way, the low catalytic activity of Witco carbon may be in part attributable to their low V_2 and V_3 values.

ACs are heterogeneous materials with numerous surface groups and a variety of pore size distributions; however, the above findings indicate that their catalytic activity in NTS ozonation is largely a function of their basicity. Their basicity derives from the presence of basic oxygen-containing functional groups (e.g., pyrone or chromene) and/or graphene layers acting as Lewis bases and forming electron donor–acceptor (EDA) complexes with H_2O molecules. The latter basic sites are localized at π electron-rich regions within the basal planes of carbon crystallites and away from their edges. This delocalized π electron system can act as a Lewis base in aqueous solution (reaction (44)):



Hence, the delocalized π electron system of basic carbons and oxygenated basic groups (chromene and pyrone) would behave as catalytic reaction centers and reduce ozone molecules to OH^- ion and hydrogen peroxide according to the following reactions:



Both OH^- and hydrogen peroxide act as initiators of ozone decomposition in aqueous phase [133]. The presence of Sorbo ($\text{pH}_{\text{PZC}} = 9.42$) and Norit ($\text{pH}_{\text{PZC}} = 9.18$) produces higher NTS degradation rates because they have greater reducing properties, favoring reactions (45) and (46) and enhancing the decomposition of ozone into highly oxidative radicals.

The total NTS ozonation degradation rate in the presence of AC was considered as the sum of the homogeneous reaction rate in the absence of AC, $(-r_{\text{M}})_{\text{homo}}$, and the heterogeneous reaction rate in the presence of AC, $(-r_{\text{M}})_{\text{hetero}}$, mathematically expressed as:

$$(-r_{\text{total}}) = (-r_{\text{homo}}) + (-r_{\text{hetero}}) = \left(-\frac{dC_{\text{M}}}{dt}\right)_{\text{homo}} + \left(-\frac{dC_{\text{M}}}{dt}\right)_{\text{hetero}} \quad (47)$$

Heterogeneous reaction constants were determined as previously described [54] (Table 16). Thus, k_{hetero} values can be considered as a measure of the catalytic activity of ACs in NTS ozonation.

Table 16. Heterogeneous reaction constants for original and demineralized ACs according to the proposed model (adapted from [54] with permission of Elsevier, 2005).

Activated Carbon	k_{obs} s^{-1}	k_{hetero} $(\text{mol/L})^{-1} \text{s}^{-1}$	$(k_{\text{hetero}})_{\text{demi}}$ $(\text{mol/L})^{-1} \text{s}^{-1}$
F400	0.0115	134.6	106.1
Sorbo	0.0152	189.4	142.3
Merck	0.1005	114.4	105.7
Ceca GAC	0.0155	195.2	90.4
Ceca AC40	0.0086	95.2	88.5
Norit	0.0653	210.5	190.4
Witco	0.0085	94.2	94.2

Study of the association between the k_{hetero} value (Table 16) and chemical characteristics (Table 15) of ACs revealed a greater increase in NTS degradation with ACs having a high ash content and elevated concentration of basic groups, which are both catalytic centers that can decompose the ozone into highly reactive species. The highest k_{hetero} values are observed in Norit, Sorbo, and Ceca GAC carbons.

Ozonation experiments were conducted in the presence of demineralized carbons to determine the contribution of the ash to the heterogeneous NTS ozonation rate. ACs were demineralized with HCl and HF, as previously described [134]. As an example, results obtained for original and demineralized Ceca GAC samples are shown in Figure 17. The degradation rate is lower after demineralization in all ACs except for Witco because of its very low ash content (Table 15). These findings confirm the positive contribution of the mineral matter in ACs through their catalytic effect in NTS ozonation. All metals that have demonstrated catalytic activity in organic compound ozonation are found in the ACs under study, but the participation of each metal in the catalytic ozonation of NTS is difficult to evaluate.

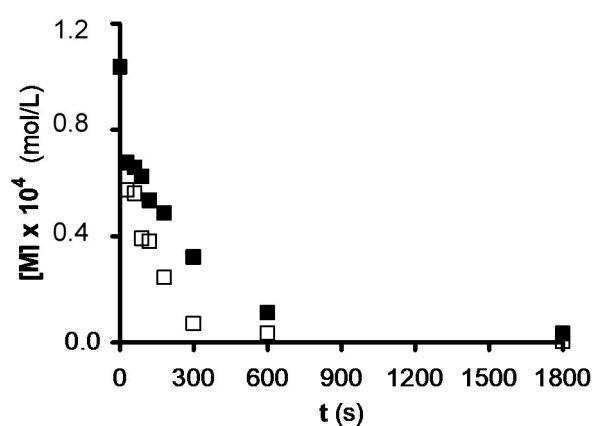


Figure 17. Effect of demineralization on the catalytic capacity of Ceca granulated activated carbon (GAC) carbon in NTS ozonation. pH = 2.3, T = 298 K. (□), untreated; (■), demineralized (reproduced from [40] with permission of Elsevier, 2002).

It has been shown that the demineralization of carbons does not substantially affect their concentration of basic surface groups [135], and the pH_{PZC} of the demineralized ACs is highly similar to that of the original ACs. Hence, a linear relationship was observed between their heterogeneous reaction constant and their surface concentration of basic groups (Figure 18). However, the ordinate in the origin is not zero, indicating that other features of the surface chemistry of ACs, in addition to the basic groups, contribute to their catalytic effect in NTS ozonation.

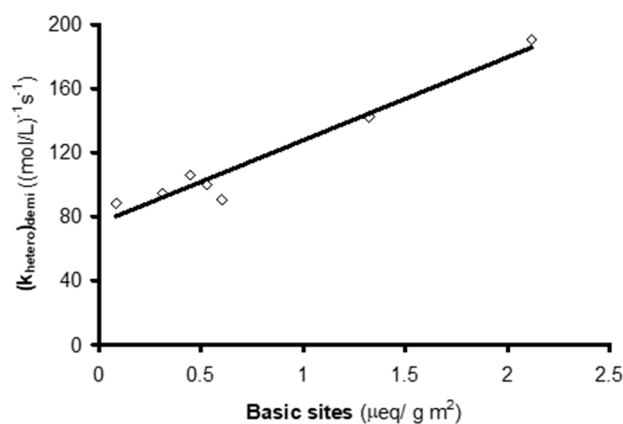


Figure 18. Relationship between (k_{hetero})_{demi} value and concentration of basic groups on the activated carbons (reproduced from [54] with permission of Elsevier, 2005).

In the presence of AC, ozonation can oxidize micropollutants by direct reaction with the ozone or by HO• radicals generated by the interaction of the ozone with the AC surface. The concentration of both oxidants must be known in order to calibrate this process with respect to its oxidation capacity. Previous studies have developed an experimental method for measuring concentrations of ozone and HO• radicals with conventional ozonation or with the AOP O₃/H₂O₂ [136]. The R_{ct} value is the ratio of HO• radical exposure to ozone exposure (Equation (48)).

$$R_{ct} = \frac{\int [HO^{\bullet}] dt}{\int [O_3] dt} \quad (48)$$

This ratio indicates the efficacy of ozone transformation into HO• radicals in a given system. The R_{ct} is calculated by measuring the reduction in a probe compound that reacts quickly with HO• but not ozone and by measuring the ozone concentration at the same time.

The influence of operational parameters was examined by conducting ozonation experiments in the presence of AC at ozone concentrations ranging between 2×10^{-5} and 6×10^{-5} M (1–3 mg/L) and AC doses ranging between 0.01 and 0.85 g/L [55]. The efficacy of HO• radical formation was identified by adding sodium para-chlorobenzoate (pCBA) as HO• radical probe compound. pCBA has a low reactivity with ozone ($k_{O_3} = 0.15 \text{ M}^{-1} \text{ s}^{-1}$) and a high affinity for HO• radicals ($k_{HO^{\bullet}} = 5.2 \times 10^9 \text{ M}^{-1} \text{ s}^{-1}$).

The concentration of dissolved ozone in the system was evaluated because the potential to oxidize micropollutants is increased at high concentrations, which also augments the formation of oxidation byproducts, e.g., bromate [137]. In addition, elevated O₃ exposure is required in disinfection systems, but not necessarily in systems designed to generate HO• radicals. Table 17 displays the R_{ct} values obtained in each experiment. It shows that this value is increased when AC F400 is present during pCBA ozonation, largely attributable to the increased rate constant for ozone decomposition (k_D), determined following a first-order kinetic model. Hence, the presence of AC promotes the transformation of ozone into HO• radicals, and a major increase in R_{ct} value is observed at higher concentrations of dissolved ozone in the O₃/AC system.

It is important to determine the minimum AC dose needed to transform ozone into HO• radicals. A higher AC dose in the system also increases the pCBA oxidation rate, and a higher rate of ozone decomposition is observed when the AC dose is increased (Table 17, Experiments 2, 5–7). Plotting the k_D or R_{ct} values against the AC dose shows a large increase at higher doses. According to these findings, the dose of AC is a key factor in the transformation of ozone into HO• radicals.

Table 17. R_{ct} values from experiments conducted at pH 7 in Milli-Q water ([NaH₂PO₄] = 5×10^{-3} M, [t-BuOH] = 8×10^{-5} M) (reproduced from [55] with permission of Elsevier, 2005).

Experiment	Sample	Carbon Dose g/L	[O ₃] M	k_D s ⁻¹	R _{ct}
1	Without carbon	0.00	2×10^{-5}	6.0×10^{-4}	2.7×10^{-9}
2	F400	0.50	2×10^{-5}	3.2×10^{-3}	1.2×10^{-8}
3	F400	0.50	4×10^{-5}	3.6×10^{-3}	1.6×10^{-8}
4	F400	0.50	6×10^{-5}	4.0×10^{-3}	4.7×10^{-8}
5	F400	0.01	2×10^{-5}	6.1×10^{-4}	3.0×10^{-9}
6	F400	0.25	2×10^{-5}	9.0×10^{-4}	6.0×10^{-9}
7	F400	0.85	2×10^{-5}	8.0×10^{-3}	5.7×10^{-8}
10	F400-1	0.50	2×10^{-5}	2.9×10^{-3}	1.4×10^{-8}
11	F400-2	0.50	2×10^{-5}	2.6×10^{-3}	1.5×10^{-8}
12	F400-3	0.50	2×10^{-5}	2.4×10^{-3}	1.5×10^{-8}
13	F400-10	0.50	2×10^{-5}	1.0×10^{-3}	5.6×10^{-9}
14	F400-120	0.50	2×10^{-5}	4.0×10^{-4}	3.8×10^{-9}

Oxidation experiments were carried out with pre-ozonated ACs (F400-1, F400-2 and F400-3) to determine changes in AC activity during ozonation [55]. It was observed that AC activity to transform ozone into HO• radicals is not affected by the ozone treatment applied, finding highly similar R_{ct} values for all three samples (Table 17, Experiments 2, 10–12). The behavior of the AC in prolonged ozone treatments was studied by subjecting AC samples to a much more drastic ozonation treatment (F400-10, F400-120). These ACs showed an important reduction in their activity to transform ozone into HO• radicals with a longer treatment time (Table 17, Experiments 2, 13, 14). The R_{ct} value is reduced from 1.2×10^{-8} (untreated) to 3.8×10^{-9} when the AC undergoes 120 min of gas-phase ozonation. According to these findings, ozone oxidation decreases the AC's catalytic properties by increasing the number of acidic oxygenated surface functional groups [55]. The electronic density of the graphene layers is diminished by these (electron-withdrawing) groups, decreasing its reductive properties and reactivity with ozone. Hence, it appears that the AC is not a true catalyst for ozone transformation but behaves as a conventional initiator or promoter in the transformation of ozone into HO• radicals.

As already noted, the combination of ozone and AC is an appealing technique for removing toxic organic compounds from waters through the AC's capacity to transform ozone into HO• radicals with higher oxidant power. This capacity is related to the AC's porous texture, surface chemistry (basic groups), and mineral matter. Accordingly, AC from petroleum coke and nitrogen-enriched ACs were prepared in our laboratory to enhance ozone transformation into HO• radicals [53,59].

Petroleum coke is a residue of the petrochemical industry, with around 4 tons being produced in the refining of 100 tons of crude oil. It cannot be used in production processes due to its elevated concentration of heavy metals (Ni, V, Fe), but this feature means that petroleum coke is an attractive material for utilization in the ozonation of aromatic pollutants. Table 18 shows the results of the textural characterization of the ACs prepared with different KOH/coke mass ratios, showing that the porosity of all samples is markedly developed by their activation, augmenting the volume of micro- (V_{mic}), meso- (V_2), and macropores (V_3). Activation of the coke also modifies its chemical nature (Table 18). Thus, the original material is mildly acid ($pH_{PZC} = 6.5$), whereas the pH_{PZC} of KOH-activated coke ranges from 8.4 for sample C-1 to 9.7 for sample C-4. This is largely due to the generation of basic surface groups during the activation process, which increases with a higher KOH/coke ratio.

Table 18. Textural characterization of original and activated cokes (adapted from [59] with permission of Elsevier, 2006).

Sample	KOH/Coke	SN_2 m^2/g	V_{mic} cm^3/g	V_2^a cm^3/g	V_3^b cm^3/g	pH_{PZC}
C	0	<30	0.02	Nil	0.011	6.5
C-1	1	1619	0.55	0.063	0.132	8.4
C-2	2	1261	0.41	0.061	0.154	8.8
C-3	3	1021	0.25	0.058	0.176	9.3
C-4	4	970	0.20	0.051	0.263	9.7

V_{mic} = micropore volume determined applying Dubinin–Radushkevich equation to CO_2 adsorption isotherm.

^a Volume of pores with a diameter of 50 to 6.6 nm. ^b Volume of pores with a diameter above 50 nm.

The k_{hetero} value of each carbon sample was calculated to determine the increase in NTS ozonation produced by its presence (Table 19), showing that the chemical activation process increases the activity of petroleum coke in NTS ozonation. Thus, the increase in k_{hetero} values with respect to that of the original coke ranges from 83% for sample C-1 to 16% for sample C-4, mainly by developing the porosity of the coke, which increases access of the ozone to its active surface sites and mineral matter, and by increasing the surface basicity of the original coke, which favors ozone reduction on its surface and thereby enhances its transformation into highly oxidant species.

Table 19. Heterogeneous reaction rate constants of activated coke samples in NTS ozonation (adapted from [59] with permission of Elsevier, 2006).

Sample	C	C-1	C-2	C-3	C-4
$k_{\text{hetero}} \text{ (mol/L)}^{-1} \text{ s}^{-1}$	57.7	105.8	86.5	76.9	67.3

Ozonation modifies the oxygenated surface groups and metal sites of these ACs and can change their oxidation state. The Fe 2p_{3/2} spectrum for samples C-1 and C-1-ozonated shows a 14% increase in the surface concentration of Fe₂O₃ on C-1-ozonated. According to these findings, the ozone can attack Fe(II) metal sites on the carbon surface during NTA ozonation, generating Fe(III) by Equations (49) and (50). These reactions can also enhance ozone transformation rate into HO• radicals, contributing to the ozonation of NTS. The main mineral components are Ni and V, and the Ni 2p_{3/2} and V 2p_{3/2} spectra show no modification in their initial oxidation state (Ni in oxidation state +2 and V in oxidation state +5).



ACs enriched in basic surface groups were prepared to examine their efficacy for NTS removal [53]. The basic surface groups were generated by treating Witco AC with nitrogenating agents (urea, ammonia, or ammonium carbonate); the textural characteristics of the samples obtained are displayed in Table 20. The treatments augment the surface area of carbon W (SN₂), especially the urea treatment (W-U). W-U has increased microporosity due to its gasification by the urea. Table 20 also reports the pore volume values determined by mercury porosimetry (V₂ and V₃), showing that treatment with ammonia (W-A) or ammonium carbonate (W-C) produces a low development of the meso- and macroporosity, whereas treatment with urea produces a high development of the micro-, meso-, and macroporosity.

Table 20. Textural characterization of basic activated carbon samples (adapted from [53] with permission of American Chemical Society, 2004).

Sample	SN ₂ m ² /g	V _{micro} cm ³ /g	V ₂ cm ³ /g	V ₃ cm ³ /g
W	812	0.238	0.040	0.050
W-A	904	0.206	0.047	0.091
W-C	825	0.222	0.042	0.102
W-U	1057	0.289	0.064	0.122

Study of the catalytic activity of the AC samples in NTS ozonation revealed increased activity in the basic samples. In the sample with the highest catalytic activity (W-U), a large proportion of surface nitrogenated groups are pyrrole groups, and a small proportion is pyridine groups, indicating that AC catalytic activity is enhanced by pyrrole-type groups. This may have the following explanation: the pair of nitrogen electrons in the pyrrole group form part of the ring electronic cloud and are therefore delocalized among the five atoms of the molecule. Consequently, pyrrole has 6 π electrons on 5 centers, making them π-excessive aromatic rings. Hence, the presence on the AC surface of pyrrole groups increases the electronic density of its basal plane, increasing its capacity to reduce the ozone dissolved on its surface (reaction (45)).

In addition, the increase in the π electron system of the AC produced by the pyrrole groups enhances the interaction with the water molecules (reaction (44)). Both processes generate OH⁻ ions in the solution, and these behave as initiators of the ozone decomposition into HO• radicals, highly reactive against NTS, which increases the degradation rate (reactions (51)–(53)).



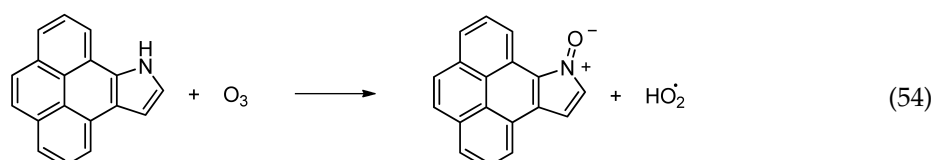


A study was conducted on the transformation of nitrogen functional groups from an interaction between ozone and AC surface during NTS ozonation in order to determine their involvement in the catalytic activity. As an example, Table 21 exhibits the changes observed in sample W-U, showing that pyridone groups are not affected by ozonation, but a large number of pyrrole-type groups are oxidized and transformed into N-oxide-type groups.

Table 21. Effect of ozonation on the concentration (%) of nitrogen surface groups on the urea treatment sample (W-U) (reproduced from [53] with permission of American Chemical Society, 2004).

Sample	Pyridine (398.5 ± 0.2 eV)	Pyridone (399.5 ± 0.2 eV)	Pyrrole (400.5 ± 0.2 eV)	N-Oxide (402.5 ± 0.2 eV)
W-U	8	42	50	-
W-U (ozonated)	7	47	16	30

According to these findings, ozone can attack the pyrrolic groups of AC graphene planes during ozonation, resulting in N-oxide type groups and hydroperoxide radicals (reaction (54)).



This reaction accounts for the changes in the pyrrole group during ozonation, which would contribute to NTS ozonation because the hydroperoxide radical increases the decomposition of ozone into radicals that can effectively degrade NTS. This may contribute to the higher catalytic activity of pyrrole groups on the AC surface.

3.2. Metal-Doped Carbon Aerogels

As mentioned above, the chemical and textural characteristics of carbon aerogels and their ready preparation have led to their utilization in numerous industrial applications [91,138,139]. Thus, carbon aerogels show high promise for boosting ozone transformation into HO[•] radicals by taking advantage of the properties of transition metals, which have contrasting catalytic activities during ozonation, preventing their dissolution in the medium and separation from the system.

Table 22 exhibits the textural characteristics of the original aerogels (A, A-Co(II)-15, A-Mn(II)-15, and A-Ti(IV)-15) prepared for utilization as ozonation catalysts [44,61]. They all have a much larger volume of mesopores (diameter 6.6–50 nm) (V_2) and macropores (V_3) than of micropores (V_{mic}).

Some chemical characteristics of carbon aerogels are shown in Table 23. Textural analysis of aerogel samples treated with ozone (A-Mn(II)-15-1, A-Mn(II)-15-2, A-Mn(II)-15-3, A-Co(II)-15-1 and A-Ti(IV)-15-1) showed similar SN_2 , SCO_2 , V_2 , and V_3 values to those in the non-pretreated samples (Table 22). According to XPS analysis, all samples show an increased percentage of surface oxygen with a higher number of ozonation cycles, whereas their pH_{PZC} values remain similar to initial values ($pH_{PZC} = 3-4$). The surface oxygen groups produced during ozonation is largely in the form of $-C=O$ in all aerogel samples. Interestingly, Mn(III) and Mn(IV) are formed in the O_3 -pretreated Mn-doped aerogel sample, and the percentage of Mn in oxidation state +4 increases with more pretreatment ozonation cycles. In samples A-Co(II)-15-1 and A-Ti(IV)-15-1, however, the oxidation state of Co and Ti stays at +2 and +4, respectively, after ozonation (Table 23).

Table 22. Textural characterization of basic activated carbon samples (adapted from [44] with permission of Elsevier, 2006).

Sample	SN ₂ m ² /g	SCO ₂ m ² /g	V _{micro} cm ³ /g	V ₂ cm ³ /g	V ₃ cm ³ /g
A	500	200	0.07	0.36	0.68
A-Co(II)-15	562	206	0.07	0.43	0.97
A-Ti(IV)-15	550	203	0.07	0.40	0.92
A-Mn(II)-15	554	210	0.07	0.41	0.95
A-Mn(II)-15-1	540	200	0.07	0.41	0.94
A-Mn(II)-15-2	534	204	0.07	0.40	0.93
A-Mn(II)-15-3	546	206	0.07	0.41	0.95
A-Co(II)-15-1	560	210	0.07	0.41	0.92
A-Ti(IV)-15-1	538	200	0.07	0.38	0.90

Table 23. Chemical characterization of the aerogel samples (adapted from [44] with permission of Elsevier, 2006).

Sample	pH _{PZC}	C %	O %	Co(II) %	Mn(II) %	Mn(III) %	Mn(IV) %	Ti(IV) %
A	3.5	68	32	-	-	-	-	-
A-Co(II)-15	3.8	64	22	14	-	-	-	-
A-Ti(IV)-15	4.3	64	21	-	-	-	-	15
A-Mn(II)-15	4.2	62	22	-	16	-	-	-
A-Mn(II)-15-1	4.0	54	30	-	10	4	2	-
A-Mn(II)-15-2	4.1	49	35	-	8	4	4	-
A-Mn(II)-15-3	3.9	42	42	-	6	4	6	-
A-Co(II)-15-1	3.9	55	31	14	-	-	-	-
A-Ti(IV)-15-1	4.2	53	32	-	-	-	-	15

Table 24 displays the R_{ct} values for pCBA ozonation in the presence of carbon aerogels and the corresponding ozone decomposition constants (k_D) determined by a first-order kinetic model.

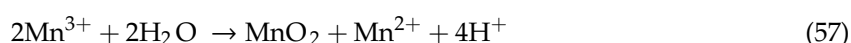
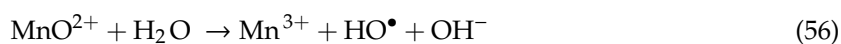
pCBA removal is not enhanced by the presence of the blank aerogel (sample A), and R_{ct} and k_D values are similar to those obtained with no aerogel (Table 24). Hence, the organic matrix of the aerogel does not contribute to the ozone transformation into HO• radicals. The presence of Mn aerogel increases the pCBA removal rate, whereas that of Co- or Ti-doped carbon aerogels has practically no impact. Given the slow reactivity of pCBA against ozone [140] and the slow adsorption kinetics of pCBA on the aerogel samples [44], the generation of HO• radicals in the system would be largely responsible for the increased oxidation rate in the presence of Mn aerogel. Furthermore, the lack of an increase in pCBA removal when the blank (aerogel A) is present corroborates a direct relationship between the activity of the aerogels to transform ozone into HO• radicals and the presence of the metal on their surfaces.

Table 24. Determination of R_{ct} value in the different ozonation experiments: pH 7, T 25 °C, $[O_3] = 2 \times 10^{-5}$ M, $[pCBA] = 8 \times 10^{-5}$ M) (adapted from [44] with permission of Elsevier, 2006).

Experiment	Sample	Carbon Dose mg	k_D s ⁻¹	R_{ct}
1	Without aerogel	0	6.0×10^{-4}	2.68×10^{-9}
2	A	2.5	6.2×10^{-4}	2.74×10^{-9}
3	A-Co(II)-15	2.5	5.8×10^{-4}	2.56×10^{-9}
4	A-Ti(IV)-15	2.5	6.1×10^{-4}	2.73×10^{-9}
5	A-Mn(II)-15	2.5	4.2×10^{-3}	5.36×10^{-8}
10	A-Mn(II)-15-1	2.5	2.6×10^{-3}	3.35×10^{-8}
11	A-Mn(II)-15-2	2.5	2.1×10^{-3}	2.68×10^{-8}
12	A-Mn(II)-15-3	2.5	1.4×10^{-3}	1.78×10^{-8}

R_{ct} values are 20-fold higher when the Mn aerogel is present during pCBA ozonation, but those obtained when Co(II) or Ti(IV) are present are similar to the R_{ct} values observed when they are not. The presence of Mn(II) aerogel during pCBA ozonation also increases the k_D value, but the presence of Co(II) or Ti(IV) aerogels has practically no effect (Table 24, Experiments 2–5). These results confirm that ozone transformation into HO^\bullet radicals is enhanced by the presence of Mn-doped carbon aerogel during the ozonation.

The mechanism by which the Mn(II) aerogel accelerates the pCBA removal rate was examined by XPS analysis of samples A-Co(II)-15, A-Mn(II)-15, and A-Ti(IV)-15 after their ozonation (samples A-Co(II)-15-1, A-Mn(II)-15-1, and A-Ti(IV)-15-1). Tables 22 and 23 exhibit their textural and chemical characteristics. Notably, the sample that enhances ozone transformation into HO^\bullet radicals (A-Mn(II)-15) is the one showing a post-ozonation increase in oxidation state (Table 23). On this sample, 10% of the surface Mn is in Mn(II), 4% in Mn(III), and 2% in Mn(IV) forms. However, the oxidation states of Co and Ti (samples A-Co(II)-15 and A-Ti(IV)-15) are not changed by ozonation (+2 and +4, respectively). According to these findings, the mechanism underlying the effect of the A-Mn(II)-15 aerogel on ozone transformation into HO^\bullet radicals is based on oxidation–reduction reactions. Hence, in agreement with results in Tables 23 and 24, the following reactions may be responsible for accelerating this transformation in the presence of A-Mn(II)-15 aerogel during pCBA:



Therefore, ozone transformation into HO^\bullet radicals through the oxidation of surface Mn(II) to Mn(III) and Mn(IV) during the oxidation process accounts for the increased pCBA removal rate. This agrees with the mechanism proposed by other authors [141,142] for atrazine and oxalic acid ozonation in the presence of dissolved Mn(II) and MnO_2 .

3.3. Basic Treated Zeolites

The crystalline network of zeolites, which are aluminosilicates, has cavities containing large ions and water molecules. Their widely varied chemical and structural composition and regular porosity make them ideal adsorbents and/or catalysts [143]. Zeolites have been proposed as catalysts of ozone decomposition in water and have been found to increase the production of free radicals during ozonation, which may be responsible for the removal of micropollutants from water [144–146]. There is currently no consensus on the factors that influence these processes, including the catalytic activity of the metals in zeolites or the ozone concentration of the catalyst. Therefore, we studied ozonation of the anionic surfactant sodium dodecylbenzene sulfonate (SDBS) as a model pollutant [67], determining the consumption of ozone and degradation of SDBS with the corresponding rate constants. Based on these findings, we proposed a reaction mechanism to modify these materials for treatment optimization.

Three types of zeolites were studied, one prepared in our lab and two commercial zeolites: high-silica zeolite ZSM-5 (SiO_2/Al_2O_3 ratio of 1000, CAS 308081-08-5), supplied by Acros Organics, and zeolite Z-13X ($Na_{86}[AlO_2]_{86}(SiO_2)_{106} \cdot xH_2O$, CAS 63231-69-6), supplied by Sigma-Aldrich. Zeolite Z-2 was obtained by mixing a molar ratio of 1.51 Na_2O , 1.13 Al_2O_3 , 0.26 SiO_2 , and 17 H_2O (Si/Al theoretical ratio = 0.24) and heating for 2 h at 373 K. Tables 25 and 26 summarize the crystallographic, elemental, and textural characteristics of all samples.

SDBS removal during ozonation in the presence and absence of the original zeolites is depicted in Figure 19, and the time course of ozone consumption in Figure 20. SDBS removal and ozone consumption rate constants are displayed in Table 27. According to these findings, Z-13X and Z-2 produced a small increase and ZSM-5 a small reduction in the SDBS removal rate. The increased SDBS removal in the presence of zeolites is related to the higher ozone consumption

observed during O₃/Zeolite treatment. Ozone has low reactivity with SDBS by direct reaction ($k_{O_3} = 3.67 \text{ M}^{-1} \text{ s}^{-1}$ [147]); therefore, SDBS degradation is largely due to the generation of HO• radicals during ozone decomposition [148]. The reaction constant of HO• radicals with SDBS is elevated ($k_{HO^\bullet} = 1.16 \times 10^{10} \text{ M}^{-1} \text{ s}^{-1}$ [147]), explaining the quick and effective degradation of the surfactant.

Table 25. Textural characteristics of zeolites (reproduced from [67] with permission of Elsevier, 2012).

Sample	SN ₂ m ² /g	W ₀ (N ₂) ^a cm ³ /g	W ₀ (CO ₂) ^b cm ³ /g	L ₀ (N ₂) ^c nm	L ₀ (CO ₂) ^d nm
Z-2	7.1	0.037	0.144	2.02	1.00
Z-13X	341.3	0.166	0.184	0.48	0.30
ZSM-5	314.4	0.161	0.245	0.41	0.74
ZSM-5-NaOH	326.4	0.162	0.320	0.70	1.14

^a Volume of micropores obtained from the Dubinin–Radushkevich equation applied to N₂ adsorption data.

^b Volume of micropores obtained from the Dubinin–Radushkevich equation applied to CO₂ adsorption data.

^c Average micropore width obtained from N₂ adsorption isotherms. ^d Average micropore width obtained from CO₂ adsorption isotherms.

Table 26. Chemical characteristics of zeolites (reproduced from [67] with permission of Elsevier, 2012).

Sample	Composition (%)				pH _{PZC}	Si/Al
	Zeolite-A	Sodalite	ZSM-5	Faujasite		
Z-2	97.3	2.7	0	0	11.4	0.89
Z-13X	0	0	0	100	11.1	1.73
ZSM-5	0	0	100	0	2.8	598.50
ZSM-5-NaOH	0	0	100	0	7.3	394.44

Table 27. Ozone consumption and SDBS removal rate constants (reproduced from [67] with permission of Elsevier, 2012).

Zeolite	Dose mg/L	K _{obs} (O ₃) s ⁻¹ × 10 ³	R ²	K _{obs} (SDBS) s ⁻¹ × 10 ⁴	R ²	(CHO•) _{het} mol/L × 10 ¹⁵
Without zeolite	0	1.27 ± 0.04	0.997	2.75 ± 0.66	0.971	
Z-2	100	1.73 ± 0.17	0.984	4.05 ± 1.16	0.959	1.36
Z-13X	100	3.83 ± 0.28	0.993	7.36 ± 1.16	0.975	4.61
ZSM-5	100	2.50 ± 0.21	0.993	2.69 ± 0.37	0.983	0
ZSM-5-NaOH	100	3.24 ± 0.22	0.981	6.25 ± 1.66	0.965	3.55

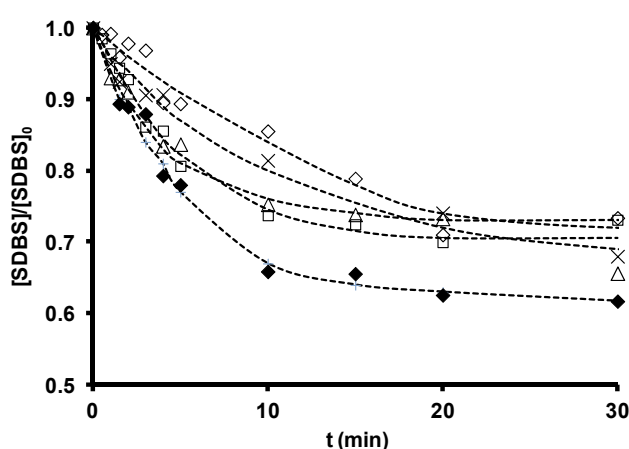


Figure 19. Sodium dodecylbenzene sulfonate (SDBS) removal as a function of ozonation time in the presence of zeolites. $[SDBS]_0 = 2.8 \times 10^{-5} \text{ M}$, $T = 298 \text{ K}$, $[O_3] = 2 \times 10^{-5} \text{ M}$, $[zeolite] = 100 \text{ mg/L}$. (x), O₃; (Δ), O₃/Z-2; (◇), O₃/ZSM-5; (◻), O₃/Z-13X; (•), O₃/ZSM-5-NaOH. (---) Fitted trend (reproduced from [67] with permission of Elsevier, 2012).

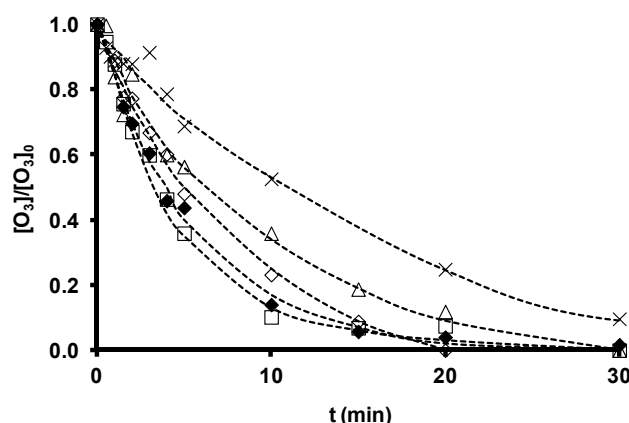
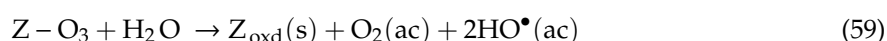


Figure 20. Time course of ozone concentration as a function of ozonation time in the presence of zeolites with different chemical characteristics. $[SDBS]_0 = 2.8 \times 10^{-5}$ M, $T = 298$ K, $[O_3] = 2 \times 10^{-5}$ M, $[zeolite] = 100$ mg/L. (x), O_3 ; (Δ), $O_3/Z-2$; (\diamond), $O_3/ZSM-5$; (\square), $O_3/Z-13X$; (\bullet), $O_3/ZSM-5-NaOH$. (---) Fitted trend (reproduced from [67] with permission of Elsevier, 2012).

Figure 19 shows that SDBS removal in these systems diminishes in the order: $O_3/Z-13X > O_3/Z-2 > O_3 > O_3/ZSM-5$. Therefore, the highest removal rate is obtained by the most basic zeolite with the largest surface area, Z-13X, underscoring the important role of these parameters in the efficacy of a zeolite as an ozone decomposition catalyst for the generation of HO^\bullet radicals. ZSM-5 obtained the lowest rate, attributable to its acid character and greater capacity to stabilize dissolved ozone molecules. However, the consumption of ozone in the presence of SDBS (Figure 20) is more rapid with the $O_3/ZSM-5$ than with the $O_3/Z-2$ system. This behavior can be attributed to the two possible contributions of zeolite to ozone consumption: (i) adsorptive contribution (reaction (58)), mainly influenced by its hydrophobicity and the type and development of its porous texture; and (ii) catalytic contribution (reaction (59)), which depends on its basicity.



The hydrophobicity of the zeolite in the $O_3/ZSM-5$ system is high and the basicity low, accelerating the consumption of ozone by adsorption. The stabilization of ozone on the adsorbent surface hampers the formation of HO^\bullet radicals and, therefore, the degradation of SDBS. In contrast, the adsorbent hydrophobicity of the zeolite is low in the $O_3/Z-13X$ and $O_3/Z-2$ systems, and its basicity is high, increasing the decomposition of ozone and generation of radicals. These HO^\bullet radicals participate in ozone decomposition in the presence of SDBS ($k_{O_3} = 1 \times 10^8 - 2 \times 10^9$ $M^{-1} s^{-1}$ [148]) (reaction (60)) and react with and degrade SDBS (reaction (61)). Consequently, ozone consumption is reduced in these systems in the presence of SDBS. This increases the efficacy of the system because fewer of the generated radicals are involved in the chain mechanism of ozone decomposition (reaction (60)).



In order to increase the catalytic potential of acid zeolite ZSM-5 in SDBS degradation, SDBS ozonation experiments were conducted in the presence of NaOH-activated ZSM-5 (sample ZSM-5-NaOH); Figures 19 and 20, and Table 27 exhibit the results.

Figure 19 shows a major increase in SDBS degradation rate (125% increase in k_{SDBS}) with the NaOH-modified zeolite ZSM-5-NaOH versus the untreated zeolite, but an increase of only 29.6% in ozone consumption (Table 27). According to findings on the chemical and textural characteristics of the

samples (Tables 25 and 26), treatment of ZSM-5 with NaOH produces: (i) increased basicity (increased pH_{PZC}), (ii) widened microporosity, and (iii) reduced hydrophobicity. These changes favor ozone decomposition into HO^\bullet radicals and, therefore, SDBS degradation. As shown in Table 27, an increased concentration of HO^\bullet radicals ($(\text{C}_{\text{HO}^\bullet})_{\text{het}}$) available for micropollutant oxidation is produced when Z13-X and ZSM5-NaOH are present during SDBS ozonation.

4. Recent Results Related to Photocatalysis and Catalyzed Ozonation for Water Treatment Using Similar Catalysts to Those Studied in Our Project

AOPs are now widely accepted as a good option for removing organic pollutants from water [149–151]. There has been an exponential growth in research on the utilization of catalyst materials to increase the efficacy of AOPs, as shown in Figure 21.

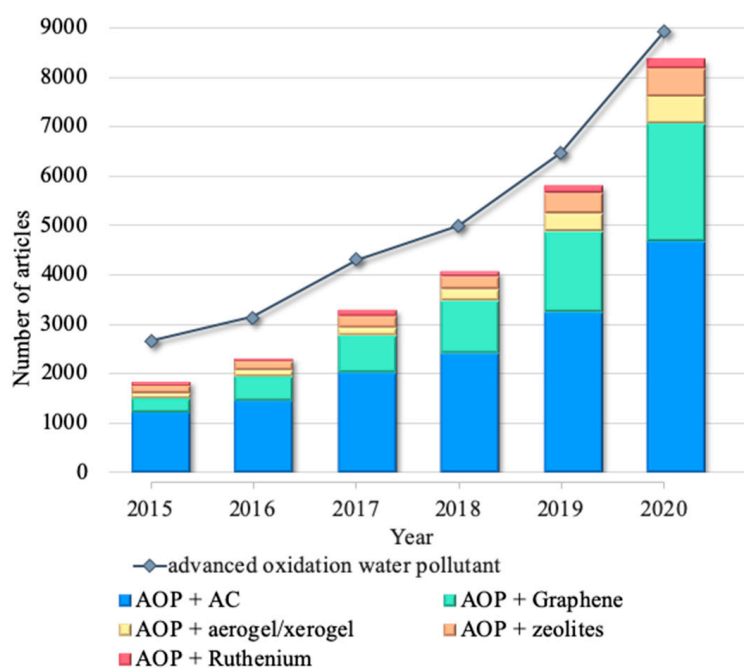


Figure 21. Trend of publications on advanced oxidation processes (AOP) research for water treatments over the past five years. Number of articles retrieved using the following search criteria (26/10/2020, Scopus): material (AC; graphene; aerogel + xerogel; zeolite; or ruthenium), advanced oxidation water pollutant.

The search of Scopus retrieved nearly 6600 research papers on the use of graphene-based materials in AOPs to treat water and 5000 of these address photocatalysis. This exponential growth in research is attributable to the exceptional characteristics of graphene, including a large surface area, excellent charge carrier mobility, superior optical transmittance, and capacity to generate different functional groups, supporting its usefulness as catalytic support [152,153]. However, challenges must still be overcome, including the stability of composite materials, their cost, and the limited scalable production of new graphene-based materials. In addition, the efficient recovery of spent graphene-based material should be explored to avoid their release into the environment. Several studies are being developed in parallel to clarify their potential toxic effects on humans and the ecosystem. These effects include severe lung diseases associated with GO [154], cytotoxicity on human erythrocytes and skin fibroblast cells [155], and reduced microbial metabolic activity [156,157]. Accordingly, there is a trend towards the development of 2D or 3D macrostructures (membranes, fibers, aerogels, and sponges) to facilitate the recovery of this material [158,159].

Nevertheless, there has been a surprising growth in the utilization of ACs in AOPs (Figure 21). Despite recognition in the world of material sciences that graphene-based catalysts are a revolutionary

material, ACs have remained the most frequently used materials over the past five years as both catalysts and supports in AOPs for water treatment. Over half (54%) of research articles address the application of some type of radiation in the AOP with AC materials, and half of these concern photocatalysis systems. The remaining studies evaluate the application of carbocatalysis in AOPs, with nearly 20% of these being AC/ozone water treatments. ACs are widely used to enhance the efficacy of AOPs because of their low cost, versatile forms, large surface areas and porosity, excellent chemical stability, and the presence of sp^2 carbon hybridization. In addition, the environmental compatibility and sustainability of ACs support their utilization in metal-free catalysis systems. Efforts have been made to facilitate the recovery of carbon material from water by structurally upgrading carbon to membranes, fibers, aerogels, and sponges [160–162]. ACs have been widely used as catalyst support [163–165], but, as explained above, some carbon materials offer more than their textural contribution. There have been no new specific studies on the photoactivity of ACs over the past five years. However, F. Velasco et al. [22,23] and Velo-Gala et al. [69,75] conducted photoactivity studies of carbon materials used as supports, finding that the removal of micropollutants is attributable to the effect of oxidant radicals generated by the interaction of radiation with the carbon.

The application of AC in ozonation systems has been most widely developed in AOPs with no radiation source [166]. Thus, recent studies focused on their applications in large-scale water treatment systems. The results obtained by Sánchez-Polo et al. [55] laid the foundations for the selection of doses and working conditions in recent large-scale research [167]. The extensive use of ACs in adsorption and ozonation processes for water treatments and their high effectiveness and simple application has brought the combined ozone/AC system closest to its full-scale application [150].

Despite the advantages of ACs, researchers have developed synthetic carbonaceous materials such as organic and carbon xerogels/aerogels to obtain high-quality materials with controllable structural and chemical properties. Organic aerogel/xerogel materials have been most widely applied in water treatment for physical pollutant separation [168]; however, it is increasingly recognized that these are promising materials for AOPs. Their useful features include their three-dimensional porous network structures, high surface area, good electrical conductivity, extremely low-density, ready separation from water, and the flexible control of their texture and composition [169,170]. Over the past two years, many researchers have shown carbon-based hybrid gels to be promising photocatalysts for the removal of organic pollutants from water [168,169,171]. In the vast majority of their applications, photocatalysis is carried out in combination with the oxides or metals dispersed in their matrix, allowing modification of their structure, physicochemical properties and, therefore, catalytic activity [168]. Aerogels/xerogels have also been applied in ozonation since the first studies on their utilization as catalysts in water. They share many of the properties of ACs, including the easy synthesis of these materials. Unlike in photocatalyst systems, carbon aerogel/xerogel materials are applied in ozonation for both their intrinsic catalytic properties and their capacities as metal support [169,172,173]. However, although these materials have made a major impact on ozonation and photocatalysis systems, they are not currently close to real-scale application due to their elevated costs. Aerogel/xerogel materials have been studied as catalysts in other AOPs, comparable to the application of ACs, but much less frequently. Their application to active oxidant sources such as persulfate was recently studied [174,175].

There have been more studies on zeolites than aerogels/xerogels in AOPs (Figure 21). Zeolites are widely used as heterogeneous catalysts in different redox processes because of the transition metals in their structure [176]. The benefits of using zeolites in AOPs include their mechanical strength, stable support of transition metal oxides, and highly selective activity [150,176–178].

Ruthenium materials have proven potentially useful in water treatments [73] but have most frequently been studied in relation to hydrogen generation [179–181].

The articles displayed in Table 28 illustrate current trends in research on different carbon-based catalysts and zeolites in photooxidation and ozonation to remove organic pollutants from water.

Table 28. Most relevant data from recent publications on carbon-based catalysts and zeolites in the photooxidation/ozonation of water contaminated with different pollutants.

Catalyst	Contaminants	System	Experimental Conditions	Observations	Ref.
Ni-, Co-, Fe-, Zn-doped organic aerogels	Trimethoprim [10 μ M]	UV/metal-carbon aerogel	Photoreactor equipped with a low-pressure Hg UV lamp (11 W) with radiation intensity between 315 and 400 nm. Temperature = 22 °C [Catalyst] ₀ = 10 mg/L Time 120 min	Trimethoprim was resistant to photolytic degradation. Apparent rate constants did not significantly vary among Fe-, Zn-, Ni-, and Co-doped aerogels. Ni-doped aerogel had a slightly higher capacity to catalyze trimethoprim degradation. % degradation = 80% with Ni doped aerogel after 2 h of irradiation.	[182]
TiO ₂ -carbon aerogel	Methyl orange [8 $\times 10^{-5}$ M]	UV/TiO ₂ -carbon aerogel	Two parallel UV lamps (Osram 18 W UV-A blacklights) Temperature = 25 °C [Catalyst] ₀ = 330 mg/L Time 240 min	The carbon aerogel (RFCA) composites had higher photocatalytic activity versus polymer aerogel (RFA) due to the larger surface area and more numerous active reaction sites of the substrate. Unexpectedly, the bare RFCA substrate was a more active photocatalyst versus its composites. % degradation = 65% with RFCA after 4 h of irradiation.	[183]
ZnO or TiO ₂ -Nitrogen-doped carbon aerogel composites	Methyl orange [4 $\times 10^{-5}$ M]	UV/carbon aerogel composites	Two parallel UV lamps (Osram 18 W UV-A blacklights) Temperature = 25 °C [Catalyst] ₀ = 330 mg/L Time 240 min	The bare carbon aerogel and TiO ₂ -coated samples were the most active ones and were even more efficacious than P25. The highest photocatalytic efficacy was observed for the sample coated with thinner layers of TiO ₂ , which decomposed around 40% of methyl orange dye after 240 min.	[184]
ZnS-carbonaceous aerogel composites	Methylene blue [40 mg/L]	Visible/carbon aerogel composites	500 W xenon lamp with 420 nm cutoff filter. [Catalyst] ₀ = 1000 mg/L Time 120 min	The 55 wt % ZnS/CA sample exhibits excellent photocatalytic performances for methylene blue degradation: 91% degradation after 180 min of irradiation.	[185]
Iron-doped carbon xerogel	Brilliant green, crystal violet, methyl green [100 mg/L]	Heterogeneous Fenton	Temperature = 25 °C, 50 rpm [Catalyst] ₀ = 4 g/L pH = 5.5–6 Time 180 min	Dyes and TOC removal efficacies up to 99% and 65%, respectively, were obtained for all dyes. % efficiencies obtained for all dyes directly correlate with the iron content.	[186]

Table 28. Cont.

Catalyst	Contaminants	System	Experimental Conditions	Observations	Ref.
ZnO-carbon xerogel composites	Chlorophenol, bisphenol A [10 mg/L]	UV or solar/carbon xerogel composites	Source of solar radiation was an Osram Ultra Vitalux 300 W lamp; source of visible radiation source was an Osram Powerstar HQI-T W/D Pro 400 W. Temperature = 25 °C [Catalyst] ₀ = 500 mg/L Time 300 min	All composites showed photocatalytic activity to degrade 4-chlorophenol and bisphenol A under both solar and visible radiation. Materials with intermediate proportions between carbon xerogel and zinc oxide were optimal for the photodegradation. The maximum values for the degradation of 4-chlorophenol were 88% and 49% after 5 h under solar and visible radiation, respectively % bisphenol A degradation values were 78% and 42%, respectively.	[187]
Iron-doped carbon xerogel	Propyl paraben (PP) [420 µg/L]	Activated persulfate (PS) oxidation	[PS] = 25–750 mg/L pH = 3, 6, and 9 Temperature = 25 °C [Catalyst] ₀ = 63 mg/L Time 60 min	The pseudo-first-order degradation rate of PP increased with higher PS concentration and lower PP concentration and solution pH. The water matrix had a detrimental effect on kinetics depending on the complexity and concentration of matrix constituents.	[188]
ZrO ₂ -carbon xerogel composites	Orange G [10 mg/L]	Visible/carbon xerogel composites	Glass photoreactor equipped with visible ReptoLux 2.0 14 W lamp. Temperature = 25 °C [Catalyst] ₀ = 1000 mg/L Time 400 min	The composites were more efficacious versus the pure samples, obtaining % degradation values of 47.7%, 63.0%, and 98.0% for catalysts with 20, 30, and 40% ZrO ₂ content, respectively. There was a very high synergic effect between carbon xerogel and ZrO ₂ , with a higher catalytic efficacy versus P25, providing an effective and more rapid degradation of Orange G.	[189]
Ni-doped carbon xerogels	Methyl orange [25, 50, and 100 mg/L]	Catalytic wet peroxide oxidation	[H ₂ O ₂] = 0.026, 0.08, 0.4 M pH = 3, 5, and 8 Temperature = 50 and 70 °C [Catalyst] ₀ = 500 and 1000 mg/L Time 150 min	The dye decomposition rate was strongly dependent on the H ₂ O ₂ dose, temperature, catalyst dose, and initial concentration of dye. The catalytic decomposition of dye was complete in 30 min using CX-Ni-500 at pH 3. Incorporation of metallic Ni by impregnation-reduction method onto the carbon xerogel surface was largely responsible for the dye decomposition efficacy.	[190]

Table 28. Cont.

Catalyst	Contaminants	System	Experimental Conditions	Observations	Ref.
Nb ₂ O ₅ -silica xerogels	Methylene blue (MB) [12 mg/L]	UVC/catalyst	Lamp with UVC light (Phillips/254 nm) [Catalyst] ₀ = 20,000 mg/L Time 500 min	The pure silica xerogel showed no photoactivity. Nanocomposites heated at 500 and 700 °C are formed by small crystallites with low photoactivity dispersed in the matrix, while samples heated at 900 °C showed good activity, reducing the concentration of MB by 80% after 500 min.	[191]
Ag/titania–silica xerogel	Methyl orange, methylene blue, phenol, salicylic acid, and rhodamine B [100 µM]	UV/catalyst	UV reactor system equipped with medium pressure 150 W Hg lamp, UV light range 350–400 nm. Temperature = 20 °C [Catalyst] ₀ = 375 mg/L Time 120 min	The efficacy to degrade methyl orange and phenol was higher by photolysis than by photocatalysis. The amount of rhodamine B degraded was higher by photocatalysis than by photolysis after the first 30 min. The methylene blue degradation rate was higher by photocatalysis than by photolysis because of the affinity of the positively charged molecule for the negative surface of the catalyst. The salicylic acid degradation rate was the same by photolysis and photocatalysis.	[192]
Fe-SiO ₂ xerogels	<i>p</i> -Nitrophenol (PNP) [10 ⁻⁴ M]	Photo-Fenton process	Halogen lamp (300 W, 220 V) with a continuous spectrum from 300 to 800 nm. [H ₂ O ₂] = 10 ⁻³ M Temperature = 20 °C [Catalyst] ₀ = 550 mg/L Time 24 h	Photo-Fenton activities of the two iron-doped samples can be directly linked to their specific morphologies. The iron-doped sample without EDAS had the greatest PNP degradation efficacy (99%) due to the direct availability of iron. Nevertheless, the PNP degradation was higher for the sample with EDAS (76%) than for the blank experiment without catalyst (64%). The catalysts displayed stable catalytic activity after 72 h of operation.	[193]
Magnetic AC	Remazol black dye (RB) [40mg/L]	UV/AC-Fe	Radiation source: low-pressure mercury lamp; emission spectrum 254 nm (30W-Philips, I = 1.20mW cm ⁻²). [Catalyst] ₀ = 300 mg/L Volume = 200 mL Time 240 min Temperature = 25 °C	Percentage discoloration of RB by photocatalysis was 16% for the AC-Fe catalyst and 17–67% for AC-Fe catalysts with different Ti concentrations. AC-Fe evidenced photoactive behavior.	[194]

Table 28. Cont.

Catalyst	Contaminants	System	Experimental Conditions	Observations	Ref.
Activated carbon codumil	Paracetamol [50 mg/L]	UV/AC	Radiation source: one or two 8 W Phillips mercury vapor lamps; emission spectrum 254 nm ($I = 59.8 \text{ mW/cm}^2$ and 119.6 mW/cm^2). [Catalyst] ₀ = 250 mg in 50 mL Volume = 50 mL Time: 120 min	There was a higher degradation of paracetamol pre-adsorbed on AC. The percentage degradation of paracetamol adsorbed on AC with UV-C irradiance had a maximum value of 79%, while the maximum values for alumina and silica were 65% and 77%, respectively.	[195]
Commercial AC and endocarp of babassu coconut (EBC) chemically activated with H ₃ PO ₄ (85%)	Methylene blue (MB) [20 mg/L]	AC Merck, ECB and EBC/Fe, simulated solar radiation	Radiation source: solar simulator box; Xe-lamp solar spectrum (I (UV region) = 105 W/m^2 , corresponding to 9% of the total radiation I of 1162 W/m^2). [Catalyst] ₀ = 50 mg/L Volume = 125 mL Time: 300 min	MB concentration was reduced by 22% with commercial AC, showing that the photochemical activity of this AC is low but not negligible. The most striking performance was achieved with the EBC/Fe-700° nanocomposite (ca. 58% MB converted after 5 h). Formation of the FePO ₄ phase at 700 °C is the main factor responsible for the increase in photoactivity.	[196]
Ruthenium doped titanate nanowires (Ru-TNW)	Cyclophosphamide (CP) and ifosfamide (IF)	UV-vis/Ru-TNW	Radiation source: 450 W medium-pressure mercury-vapor lamp (Hanovia, Slough, UK); total I energy = 40–48% in the UV range and 40–43% in the visible region. [Catalyst] ₀ = 130 mg/L Volume = 150 mL [CP] ₀ = [IF] ₀ = 10 mg/L Time 120 min Water matrix: distilled water (DW) and wastewater (WW) from secondary wastewater treatment.	The removal rate of both pollutants with Ru-TNW as photocatalyst under UV-vis radiation was two-fold that obtained with photolysis in DW. The $t_{1/2}$ was 10.6 min and 8.0 min for CP and IF, respectively. In WW, the increase in $t_{1/2}$ was 4.5 min and 4.9 min, respectively.	[197]
RuO ₂ -GO composite	Methylene blue (MB)	Sunlight/RuO ₂ Sunlight/GO Sunlight/RuO ₂ -GO	Radiation source: solar light from 11.30 a.m. to 2.30 p.m. during the summer in Bengaluru, Karnataka (India). $I = 68,000 \text{ flux}$. [Catalyst] ₀ = 500 mg/L Volume = 40 mL [MB] ₀ = 20 mg/L Time: 60 min	After irradiation for 60 min, the MB removal rate was 95% in the presence of RuO ₂ -GO composite versus 40% with pure RuO ₂ and 20% with GO. The enhanced photocatalytic activity of the RuO ₂ -GO composite was due to the synergistic effect between mesoporous RuO ₂ anchored on GO via Ru–O–C bond.	[198]

Table 28. Cont.

Catalyst	Contaminants	System	Experimental Conditions	Observations	Ref.
rGO-TiO ₂	Orange G [20 mg/L]	solar/rGO-TiO ₂	SOLAR BOX 1500 e with a 1500 W Xenon lamp Temperature = 28 °C pH = 6 [Catalyst] ₀ = 1000 mg/L Time 60 min	Orange G photodegradation was always higher with graphene derivative-TiO ₂ composites than with TiO ₂ under simulated solar light. Orange G conversion rates of 99.8%, 90.0%, 98.2%, 96.5%, and 47.6% were obtained at 60 min with GO-T, rGO-T, rGONS-T, rGOB-T, and TiO ₂ , respectively. The photocatalytic activity of the samples decreased with increased initial pH.	[199]
rGO-TiO ₂	Diuron [7.5 mg/L], alachlor [12.5 mg/L], isoproturon [12.5 mg/L] and atrazine [6.25 mg/L]	UV, visible/rGO-TiO ₂	Six UV black blue light lamps (Narva LT 15 W/073) and 4 Daylight lamps (Narva LT 15 W/865) for UV-vis experiments. Under near-visible, 10 daylight fluorescent lamps were employed [Catalyst] ₀ = 500 mg/L Time 300 min	Pesticide photodegradation and TOC abatement were greater with the GO-TiO ₂ composite than with bare TiO ₂ . This increase in photoefficiency was even greater in natural water.	[200]
rGO-TiO ₂	4-chlorophenol [0.1 mmol/L]	UV/rGO-TiO ₂	Sylvania Lynx-S 11WBLB lamp, UV light (365 nm), density of 1.0 mW/cm ² Temperature = 25 °C pH = 6 [Catalyst] ₀ = 1000 mg/L Time 300 min	The presence of rGO in the composite increased the formation of hydroxyl/HO• radicals to attack the 4-chlorophenol molecules, explaining the improvement in photocatalytic performance. In comparison to TiO ₂ , the rGO/TiO ₂ photocatalyst increased the first-order reaction rate constant by around 70%. % degradation = 85% after 5 h of irradiation.	[201]
rGO@g-C ₃ N ₄ -TiO ₂ nanotube	Tetracycline hydrochloride [20 mg/L]	UV/catalyst	Xenon lamp (150 W) Time 120 min	rGO@g-C ₃ N ₄ /TNAs photoelectrodes exhibited higher photocatalytic activity. The removal rate of tetracycline by rGO@g-C ₃ N ₄ /TiO ₂ nanotube photoelectrodes reached 90% after 120 min, and the reaction kinetic constant was 2.38-fold higher than for TiO ₂ nanotube photoelectrodes.	[202]
rGO-Cu ₂ O/Bi ₂ O ₃	Tetracycline [10 mg/L]	Visible/rGO-Bi ₂ O ₃	250 W Xe lamp with UV cutoff filters [Catalyst] ₀ = 500 mg/L Time 180 min	TC photodegradation in the presence of rGO-Cu ₂ O/Bi ₂ O ₃ and rGO/Bi ₂ O ₃ was 38% and 24.5%, respectively, after 3 h. The photocatalytic activity of the composites was greater, with an increase in GO from 20 to 50 mg.	[203]

Table 28. Cont.

Catalyst	Contaminants	System	Experimental Conditions	Observations	Ref.
rGO-Bi ₂ O ₃	Methylene blue [0–50 mg/L]	Visible/rGO-Bi ₂ O ₃	Visible photoreactor. 500 W tungsten halogen lamp (400–800 nm) [Catalyst] ₀ = 300–2000 mg/L Time 500 min	Maximum MB degradation of 98% was achieved at neutral pH with 1 g/L of catalyst. The rGO-Bi ₂ O ₃ nanocomposite exhibited higher photocatalytic activity (98%) versus pristine Bi ₂ O ₃ (55%) or rGO (20%) under visible light irradiation after 240 min.	[204]
rGO-Bi ₂ O ₃	Rhodamine B [10 mg/L]	Visible/rGO-Bi ₂ O ₃	300-W xenon lamp Temperature = 25 °C [Catalyst] ₀ = 1000 mg/L Time 90 min	Composites with 1% rGO showed the highest photocatalytic activity (100% degradation of rhodamine B after 30 min), which was three-fold higher versus bare Bi ₂ O ₃ . This high photocatalytic activity was attributed to the presence of graphene, which served as an electron collector and transporter to increase the lifetime of photogenerated charge carriers from Bi ₂ O ₃ .	[205]
Activated carbon-TiO ₂	Tetracycline [30 mg/L]	OV or US/catalyst	UV light from UV-C lamp (PHILIPS) with $\lambda = 254$ nm and intensity of 6 W. Temperature = 25 °C [Catalyst] ₀ = 300 mg/L Time 180 min	The degradation rate was higher when AC-TiO ₂ was coupled with US and UV irradiations. Removal rates of 93 and 50.4% were achieved for TC and TOC, respectively, after 180 min irradiation. The anions exerted an inhibitory effect.	[206]
Activated carbon-TiO ₂	Orange G [10 mg/L]	UV/carbon-TiO ₂	Low-pressure mercury vapor lamp (TNN 15/32, 15 W, $\lambda = 254$ nm) [Catalyst] ₀ = 1000 mg/L Time 40 min	Carbon-Ti materials with a developed micro-mesoporosity reduced the bandgap, being more active in orange G photodegradation under UV irradiation versus TiO ₂ , reaching 100% degradation after 30 min of irradiation. Catalytic activity decreased with higher carbonization temperature.	[207]
Activated carbon-TiO ₂	Carbamazepine [50 mg/L]	solar/carbon-TiO ₂	LOT Quantum Design xenon lamp system (300 W) Temperature = 20 °C [Catalyst] ₀ = 100 mg/L Time 300 min	The composite with 9% TiO ₂ was selected because it had the highest adsorption and degradation rate and lowest production cost. % degradation = 85% after 300 min of irradiation.	[208]

Table 28. Cont.

Catalyst	Contaminants	System	Experimental Conditions	Observations	Ref.
Activated carbon-TiO ₂	2,4-dichlorophenol [100 mg/L]	solar/carbon-TiO ₂	300-W xenon lamp [Catalyst] ₀ = 250 mg/L Time 300 min	AC can accept the photogenerated electrons, improving charge separation and considerably improving photocatalytic activities to degrade 2,4 dichlorophenol. The photogenerated hydroxyl/HO• radicals may predominate in the photocatalytic degradation of 2,4 dichlorophenol.	[209]
Granulated activated carbon (GAC)	Reactive Blue 194 (RB194) [10–200 mg/L]	Activated carbon catalyzed ozonation (ACCO)	Continuous 178.8 mg O ₃ /L Gas flow 1.5 L/min Temperature = 24, 35 and 50 °C [Catalyst] ₀ = a column packed with 2.6 L GAC and 1.2 L dye solution Time: 40 min [NaCl] = 5–50 g/L	With ozonation alone, an increase in NaCl concentration had a negligible effect on RB194 removal, but enhanced color removal by ACCO, obtaining % color removal of 61 and 84% after 5 min of contact with NaCl concentrations of 5 and 50 g/L, respectively. 100% color removal was achieved by O ₃ after 20 min. Besides the synergistic effect of GAC in the ozone system, the higher dye removal rate was attributed to the production of reactive chlorine species.	[210]
Olive stone activated carbon (OSAC)	Clopyralid [1 mg/L]	O ₃ /OSAC	Continuous 15 mg O ₃ /L Gas flow 30 L/h Temperature = 25 °C [Catalyst] ₀ = 0.1–1 g/L Time: 60 min solar simulator (SSR): Xe arc lamp 500 W/m ² of radiation over 300 nm.	The use of OSAC increased the removal of clopyralid from 66% to 96% after 30 min versus ozone alone. The OSAC concentration of 0.75 g/L yielded the best removal of clopyralid with O ₃ . Kinetic rate constant values were: O ₃ /OSAC (0.106 min ⁻¹) > O ₃ /OSAC/SSR (0.099 min ⁻¹) > O ₃ /SSR (0.097 min ⁻¹) > O ₃ (0.063 min ⁻¹). OSAC can be considered not only as an adsorbent but also as a catalyst.	[211]
Commercial granular activated carbon (GAC)	Acid red 3R [100 mg/L]	O ₃ MB/GAC	Continuous 12.5 mg O ₃ /L Gas flow 0.3 L/min [Catalyst] ₀ = 2.0 g/L Time 120 min Diameter of O ₃ microbubbles (MBs): 50 μm	Decolorization rate constants were 0.342 min ⁻¹ and 0.173 min ⁻¹ for MB ozonation with and without AC, respectively. O ₃ self-decomposition rate constants in water in MB aeration and coarse bubble aeration were 0.049 min ⁻¹ and 0.013 min ⁻¹ , respectively. When AC was added to MB aeration, the O ₃ self-decomposition rate constant increased to 0.093 min ⁻¹ because O ₃ decomposition was enhanced by the catalytic effect of AC. The catalytic activity of this commercial AC appeared stable after five cycles.	[212]

Table 28. Cont.

Catalyst	Contaminants	System	Experimental Conditions	Observations	Ref.
Commercial granular activated carbon (GAC)	Drugs and additives mix as micropollutants (MP)	O ₃ /GAC at pilot-scale in wastewater effluent, over a long-term experiment	Continuous 0.3 and 0.5 mg O ₃ /mg DOC. Gas flow 5 L/min [Catalyst] ₀ = 0.5 and 2.0 g/L Time 20 h. Influent: tertiary-filtered wastewater effluent from a reclamation facility in Nevada, USA. MP mix (ng/L): triclosan (27.00), sulfamethoxazole (742.5), carbamazepine (142.5), naproxen (19.25), trimethoprim (15.25), gemfibrozil (1.37), atenolol (37.5), fluoxetine (26.5), DEET (135.25), primidone (145.0), sucralose (48500), meprobamate (242.5), NMOR (15.5), TCEP (240.0).	O ₃ /GAC improved the abatement of MPs (TCEP, sucralose, and meprobamate) versus ozonation alone at 20 h of operation. However, the overall effectiveness of O ₃ /GAC markedly decreased after longer O ₃ exposure, and the improvement ceased for most of the MPs (except sucralose and NMOR) after 20 h of operation due to O ₃ -induced changes in GAC surface properties (structural damage, reduced surface area, and increase in surface acidic functional groups).	[213]
Powdered activated carbon (AC-1230) (75 µm particle size)	Drugs mix as micropollutants (MP)	O ₃ /PAC	Continuous 0.5–2.0 mg O ₃ /L Gas flow 24 L/h [Catalyst] ₀ = 20 mg/L Time 30 min Influent: ultrapure (UPW) and natural water (NW) from the Biobío river. Toxicity test with <i>Daphnia magna</i> . MP (2.30–2.90 mg/L): atrazine (ATZ), carbamazepine (CBZ), diclofenac (DCL), triclosan (TCS)	Treatment with O ₃ and O ₃ /PAC showed the slowest transformation rate for ATZ (>90% at 30 min) but a very fast rate for CBZ, DCL and TCS (>90% at 5 min). ATZ oxidation was mainly driven by HO• radicals, while CBZ, DCL and TCS were directly removed by O ₃ . Addition of PAC in the ozonation process markedly improved acute toxicity removal. For a similar TOC reduction, the reaction time was reduced from 60 to 10 min in O ₃ /PAC.	[214]
Carbon aerogel	Reactive blue 19	O ₃ /carbon aerogel	Continuous Temperature = 24 °C 2.5 mg O ₃ /min [Catalyst] ₀ = 4 g/L Time 20 min	The presence of carbon aerogel increased decolorization versus ozonation alone. The percentage of decolorization was almost 99% after 5 min in the presence of carbon aerogel.	[172]
Carbon aerogel	Reactive blue 19	O ₃ /carbon aerogel	Continuous 8 mg O ₃ /L Gas flow 0.5 L/min Temperature = 24 °C [Catalyst] ₀ = 2.0 g/L or 2.4 g/L Time 30 min	The participation of carbon aerogel strikingly enhanced the removal of dye versus ozonation alone. Decolorization rates of 85%, 73% 55% were obtained after 5 min using Ag-Fe ₂ O ₃ /carbon aerogel, carbon aerogel, and ozone alone, respectively.	[215]

Table 28. Cont.

Catalyst	Contaminants	System	Experimental Conditions	Observations	Ref.
Carbon aerogel	Reactive blue 19	O ₃ /carbon aerogel	Continuous 8 mg O ₃ /L Gas flow 0.5 L/min Temperature = 24 °C [Catalyst] ₀ = 1.0 g/L or 1.2 g/L Time 30 min	Ozonation alone was generally not able to completely degrade organic contaminants and needed the addition of a catalyst to promote degradation. After 10 min, the effluent was treated by catalytic ozonation was 100% decolorized, whereas ozonation-treated effluent remained bluish.	[216]
Cerium-loaded natural zeolite (CZ)	Penicillin G (PG) [50mg/L]	O ₃ /CZ	Continuous 6 mg O ₃ /min Gas flow 0.6 L/min Temperature = 25 °C [Catalyst] ₀ = 0–3 g/L Time 15 min Cerium = 0–8%	PG degradation efficacy of the O ₃ /CZ system was higher than that of O ₃ alone. Optimal operating conditions were: Ce loading mass = 4%, CZ dosage = 2 g/L, O ₃ dosage = 6 mg/min, and initial solution Ph = 4.5. PG removal was 99.5% after 15 min. These optimal conditions produced the highest specific catalyst surface area of the catalyst with no agglomeration of Ce particles, and the appropriate ratio between O ₃ and catalyst was not limited by ozone dosage.	[217]
High-silica zeolites ZSM5, loaded with metallic (Ce, Fe, or Mn) oxides	Nitrobenzene [100 mg/L]	O ₃ /ZSM5	Continuous 5 mg O ₃ /min Gas flow 3 L/min Temperature = 30 °C [Catalyst] ₀ = 2.5 g/L Time 60 min Ce = Fe = Mn = 0.8 wt % Pristine ZSM5 zeolites: NaZ38 (Na type of counter ion, molar ratio SiO ₂ /Al ₂ O ₃ = 38, Na ₂ O at 4.08 wt %); HZ38 (H type, SiO ₂ /Al ₂ O ₃ ratio = 38, Na ₂ O at 0.13 wt %), and NaZ100 (Na type, SiO ₂ /Al ₂ O ₃ = 100, Na ₂ O at 1.57 wt %).	Adsorption and direct ozonation contributed to early TOC removal in O ₃ /ZSM5 with HZ38 and NaZ100 zeolites. HO• radicals dominate the removal process. Among the ZSM5 zeolites studied, Ce/NaZ38 achieved the highest TOC removal, attributable to the surface SiO bonds.	[218]
Zeolite 4A (Z4A)	Paracetamol [50mg/L]	O ₃ /Z4A	Continuous 0.9 mg O ₃ /min Temperature = 25 °C [Catalyst] ₀ = 11.11 g/L Time 60 min	Z4A did not promote the decomposition of ozone to produce HO• and O ₂ • ⁻ radicals. Thus, paracetamol ozonation in the presence of Z4A followed a non-radical mechanism. Z4A removed paracetamol by direct reaction with the O ₃ molecule. The effect of Z4A was attributed to the approximation of both pollutant and O ₃ molecules by adsorption on its surface.	[219]

Table 28. Cont.

Catalyst	Contaminants	System	Experimental Conditions	Observations	Ref.
H- and Fe-modified Beta zeolite	Ibuprofen (IBU) [10–100 mg/L]	O ₃ /Beta-Zeolite	Continuous 60 mg O ₃ /L Gas flow 0.25–1.1 L/min Temperature = 5–30 °C [Catalyst] ₀ = 0.25–1.0 g/L Time 4 h Catalysts: H-Beta-25, Fe-H-Beta-EIM-25 and Fe- H-Beta-150-SSIE	The presence of zeolite catalysts improved IBU removal, especially at lower temperatures, because the O ₃ concentration was higher. Catalysts with a larger amount of Brønsted and Lewis acid sites and higher Fe concentration achieved greater degradation of IBU.	[220]
Natural zeolite	Standard mix of organochlorinated compounds (Supelco Co.) in high-quality (99%)	O ₃ /Zeolite vs. O ₃ /GAC	Continuous 5 g O ₃ /h Gas flow 0.5 L/min [Catalyst] ₀ = not specified Time 30 min Organochlorinated compounds: heptachlor (HCH), hexachlorobutadiene (HCHBD), lindane (LIN), pentachlorobenzene (PCHB), hexachlorobenzene (HCHB).	Adsorptive O ₃ /GAC and O ₃ /Zeolite ozonation processes significantly reduced the reaction time versus O ₃ or O ₃ /UV. O ₃ /GAC showed greater potential for organochlorine compound removal versus O ₃ /Zeolite.	[221]

5. Conclusions

The DTZ removal rate is markedly increased by the presence of ACs during photooxidation, and gamma radiation enhances the synergetic activity of ACs. The textural properties of ACs are not clearly related to their synergic contribution, but those containing larger percentages of ester/anhydride groups and carbon atoms with sp^2 hybridization show higher synergetic activity. In general, gamma radiation treatment reduces the bandgap values of ACs, and, in one series of commercial carbons, a lower E_g value corresponds to a higher DTZ removal rate. Materials modified by gamma radiation contain a greater percentage of carbon atoms with sp^2 hybridization, explaining their superior behavior to degrade DTZ in the presence of UV radiation.

Determination of HO^\bullet radicals and superoxide anions in UV/AC and solar/AC systems shows that AC behaves as a photocatalytic material and that these photoinduced reactive species are responsible for the percentage degradation achieved, which is much higher than that obtained by direct radiation alone. DTZ degradation is more efficacious by radiation/AC systems than by radiation/ TiO_2 systems.

The addition of a transition metal (Co, Mn, Ti) does not have a major influence on the textural and chemical properties of the aerogels. Mn-doped aerogels significantly increase the oxidation rate during NTS photodegradation, and a rise in Mn(II) surface concentration enhances the photoactivity of this material.

The porous texture of xerogels (X-Ni, X-Co, X-Fe, X-Na) depends on the nature of the metal salt. In noncarbonized xerogels, E_g values are <4 eV due to the higher concentration of $-C=O/-OH$ groups. Carbonization of the xerogels increases their surface area and E_g (>4 eV). Degradation of the herbicide AMT during UV irradiation results from a combination of adsorption, direct photolysis, and gel-induced synergic effect. The presence of xerogels during AMT degradation produces the generation of $O_2^{\bullet-}$ and HO^\bullet radicals via the photogeneration of electron-positive hole pairs. The AMT degradation rate is proportional to the initial X-Ni concentration up to around 250 mg/L due to progressive saturation of photon absorption on the catalyst for a given incident radiation flow. X-Ni catalyst shows high stability after consecutive cycles when its catalytic activity is only slightly lower. The presence of X-Ni considerably enhances DRN degradation under solar radiation, behaving as a photocatalyst. The DRN photodegradation rate constant is proportional to the xerogel concentration up to around 4000 mg/L because a higher concentration increases the number of active surface sites for DRN photooxidation. X-Ni shows high stability after three consecutive cycles of DRN degradation under solar irradiation.

In RuBpy-doped xerogels, this complex is homogeneously distributed in the polymer matrix of the organic xerogel and provides greater thermal stability. RuBpy behaves as a sensitizer in the polymer matrix, increasing the capacity of the material to promote electrons in the presence of solar irradiation. RuBpy-doped xerogels enhance the formation of HO^\bullet radicals during solar radiation, although they do not act as true photocatalysts because their chemical properties are modified by irradiation.

Chemical and textural characterization showed that the Fe(III) doping of silica xerogels modifies their physicochemical properties. XGS-Fe(III) enhances TNZ degradation under UV radiation in an aqueous solution by generating HO^\bullet and $O_2^{\bullet-}$ radical formation and reducing Fe(III). Only 3.64% of Fe(III) is needed to achieve 68% TNZ degradation under solar radiation. Although XGS-Fe(III) does not behave as a true photocatalyst, it is readily synthesized, inexpensive, and easy to handle, characteristics that favor its utilization in AOPs.

The presence of Ru(II) tris chelate type photosensitizers significantly contributes to CTC degradation by solar radiation because they promote the formation of $^1 [O_2]^*$, the main species responsible for the degradation of this contaminant.

rGO- TiO_2 composites can be prepared using a simple hydrothermal technique method. The effective reduction of GO and the formation of pure anatase and Ti-O-C bonds are observed on the composite surface. Catalytic activity is highest for 7% rGO- TiO_2 , which achieves 98.6% EtP degradation after 40 min of UV irradiation, but the degradation then reduces with a greater percentage of rGO. Photocatalytic EtP degradation is higher with rGO- TiO_2 versus rGO-P25 composites, likely

attributable to the rutile phase in commercial P25 and its smaller surface area and larger crystal size in comparison to TiO₂ composites.

rGO/Bi nanocomposites can be synthesized by microwave treatment using the Hummers method. Characterization of the composites shows that GO is reduced to rGO and that Bi is polydispersed on their surface as a crystalline phase of Bi₂O₃. Sample 5% rGO/Bi is the most active nanocomposite for SMZ degradation under solar radiation (100% removal after 2 h) and remains unchanged after three treatment cycles. The degradation rate is lower with higher rGO content. After SMZ degradation, the aqueous medium is nontoxic.

The presence of AC increases the NTS degradation rate during ozonation and removes part of the organic matter through mineralization. The highest catalytic activity in ozonation is observed with basic ACs. Basal plane electrons and oxygenated surface groups with basic character (chromene and pyrone) on ACs are largely responsible for the ozone decomposition in the aqueous phase. The reduction of ozone on the AC surface generates OH[•] ions or H₂O₂ that initiate the decomposition of ozone into highly oxidative species responsible for increasing the NTS ozonation rate. These species can also mineralize dissolved organic matter, reducing the TOC. A high macroporosity enhances ozonation, reducing diffusion problems and, therefore, favoring access of the ozone to the active centers of the carbon surface. A study of AC activity to transform aqueous ozone into HO[•] radicals shows an increase in the transformation rate at higher doses of dissolved ozone and AC in the system. The combined presence of AC and ozone reduces the genotoxicity of NTS degradation compounds. This novel purification system has demonstrated high efficacy.

The kinetic equation representing the heterogeneous reaction rate depends on the concentrations of contaminant and dissolved ozone. The reaction order with respect to both NTS and ozone is 1. Experimental results are adequately represented by the general kinetic model proposed, which permits measurement of the carbon catalytic activity in NTS ozonation. The k_{hetero} constant values range from 94.2 (mol/L)⁻¹ s⁻¹ for Witco to 210.5 (mol/L)⁻¹ s⁻¹ for Norit carbon.

Chemical activation of petroleum coke with KOH increases its catalytic activity in NTS ozonation because of the increased basicity of the carbon and the development of its porosity, giving the ozone greater access to active sites on the carbon surface. Treatment with nitrogenating agents enhances the catalytic activity of ACs in NTS ozonation because it augments the meso- and macropore volume and increases the basicity, largely due to the creation of pyrrole groups on the carbon surface.

Metal-doped carbon aerogels can enhance the transformation of ozone into HO[•] radicals as long as the metal on their surface is susceptible to oxidation by ozone. This transformation is accelerated by the presence of Mn(II)-doped carbon aerogel during ozonation as a function of the aerogel dose and the Mn(II) concentration on its surface. The capacity of Mn-doped carbon aerogel to promote ozone transformation into HO[•] radicals decreases with longer exposure to ozone. This behavior is explained by the oxidation of surface Mn(II) to higher oxidation states, leading to inactivation of the material.

There is a small increase in SDBS degradation in the presence of a basic zeolite during ozonation and a small decrease in the presence of an acid zeolite. The ozone removal rate is only increased with the acid zeolite system in comparison to the absence of SDBS, confirming the greater catalytic capacity of basic versus acid zeolites, with the additional benefit of lower consumption of ozone. NaOH treatment of acid zeolite markedly increases the catalytic activity for SDBS ozonation with respect to the original zeolite due to (i) an increased basicity, (ii) widened microporosity, and (iii) reduced hydrophobicity. These changes enhance ozone decomposition into HO[•] radicals and therefore increase SDBS degradation.

Catalysts have proven indispensable for the treatment of water pollutants by AOPs to achieve a clean environment. Current research lines focus on the preparation of more effective materials with improved photoactivity (narrow bandgap and good separation of e⁻/h⁺ pairs) for photocatalytic AOPs or with a higher capacity to decompose different oxidant sources into radical species for other AOPs. The trend is towards a combination of purposefully tailored properties of composite materials with high stability and ready recovery, seeking economic solutions. Materials with a large surface

area, open porous structure, and tunable chemistry continues to be the preferred choice for catalyst development. For all of these reasons, it is not surprising that AC-based materials are the most frequent option, not only for research but also for large-scale applications, as in the case of ozonation systems. However, this progress in the application of AC materials as catalysts does not reduce the importance of developing other types of material. Indeed, all of these advances provide the basis for selecting the most appropriate new materials for research on water treatments. This is the case of graphene-based materials and other types of catalysts described in this review. Graphene-based materials, organic aerogels/xerogels, and zeolites are all suitable for utilization as metal catalyst nanocomposites, with attractive textural and structural properties and versatile synthesizing methods.

6. Future Outlook

This review confirms the importance of carbon materials in enhancing the effectiveness of both the photooxidation and ozonation of pollutants. Future research should focus on the development of carbon material-based nanocomposites for enhancing water treatments at pilot and technological scales in flow reactors, increasing pollutant mineralization and reducing water toxicity. These nanocomposites need to be inexpensive and effective and should not undergo a transformation during water treatment, allowing their utilization for long periods of time. If they are changed by the treatments, they must be readily regenerable.

We highlight the need for standardization in research efforts to understand the mechanisms governing catalytic photooxidation and ozonation. Critical parameters in these studies would be the solution pH and the nature of active surface sites responsible for catalytic reactions.

Author Contributions: Individual contributions of all authors are specified as follows: writing—original draft preparation, J.R.-U., M.V.L.-R., M.S.-P., M.Á.Á., I.V.-G.; writing—review, editing, and supervision, J.R.-U. and M.V.L.-R. All authors have read and agreed to the published version of the manuscript.

Funding: This research was funded by the Spanish Ministry of Economy, Industry and Competitiveness and FEDER (Project CTQ2016-80978-C2-1-R), and Junta de Andalucía, Spain (Project P18-RT-4193).

Acknowledgments: Authors from the University of Granada (J.R.-U. and M.S.-P) and authors from Universidad de Jaén (M.V.L.-R. and M.Á.Á.) acknowledge financial support from Junta de Andalucía, Spain, RNM-172 and RNM-366 research groups, respectively.

Conflicts of Interest: The authors declare no conflict of interest.

References

1. Andreozzi, R.; Caprio, V.; Insola, A.; Marotta, R. Advanced oxidation processes (AOP) for water purification and recovery. *Catal. Today* **1999**, *53*, 51–59. [[CrossRef](#)]
2. Brillas, E.; Mur, E.; Sauleda, R.; Sanchez, L.; Peral, J.; Domenech, X.; Casado, J. Aniline mineralization by AOP's: Anodic oxidation, photocatalysis, electro-Fenton and photoelectro-Fenton processes. *Appl. Catal. B Environ.* **1998**, *16*, 16–31. [[CrossRef](#)]
3. Matatov, M.Y.I.; Sheintuch, M. Catalytic abatement of water pollutants. *Ind. Eng. Chem. Res.* **1998**, *37*, 309–326. [[CrossRef](#)]
4. Niu, L.; Wei, T.; Li, Q.; Zhang, G.; Xian, G.; Long, Z.; Ren, Z. Ce-based catalysts used in advanced oxidation processes for organic wastewater treatment: A review. *J. Environ. Sci.* **2020**, *96*, 109–116. [[CrossRef](#)]
5. Singer, P.C.; Reckhow, D.A. *Water Quality & Treatment: A Handbook of Community Water Supplies*; McGraw-Hill: New York, NY, USA, 1999.
6. Pitochelli, A. Biocides: Useful applications for the use of chlorine dioxide in water treatment. *Ultrapure Water* **2006**, *23*, 40–42.
7. Zou, L.Y.; Li, Y.; Hung, Y.S. Wet air oxidation for waste treatment. *Handb. Environ. Eng.* **2007**, *5*, 575–610.
8. Von Sonntag, C. The basics of oxidants in water treatment. Part A: OH radical reactions. *Water. Sci. Technol.* **2007**, *55*, 19–23. [[CrossRef](#)]
9. Peter, A.; Von Gunten, U. Oxidation kinetics of selected taste and odor compounds during ozonation of drinking water. *Environ. Sci. Technol.* **2007**, *41*, 626–631. [[CrossRef](#)]

10. Barry, T.I.; Stone, F.S. The reactions of oxygen at dark and irradiated zinc oxide surface. *Proc. R. Soc. A* **1960**, *255*, 124–144.
11. Fujishima, A.; Honda, K. Electrochemical photolysis of water at a semiconductor electrode. *Nature* **1972**, *238*, 37–38. [[CrossRef](#)]
12. Henderson, M.A. A surface science perspective on TiO₂ photocatalysis. *Surf. Sci. Rep.* **2011**, *66*, 185–297. [[CrossRef](#)]
13. Serpone, N.; Pelizzetti, E. *Photocatalysis: Fundamental and Applications*; Wiley: New York, NY, USA, 1989.
14. Zu, D.; Song, H.; Wang, Y.; Chao, Z.; Li, Z.; Wang, G.; Shen, Y.; Li, C.; Ma, J. One-pot in-situ hydrothermal synthesis of CdS/Nb₂O₅/Nb₂C heterojunction for enhanced visible-light-driven photodegradation. *Appl. Catal. B Environ.* **2020**, *277*, 119140. [[CrossRef](#)]
15. Czech, B.; Zygmont, P.; Kadirova, Z.C.; Yubuta, K.; Hojamberdiev, M. Effective photocatalytic removal of selected pharmaceuticals and personal care products by elsmoreite/tungsten oxide@ZnS photocatalyst. *J. Environ. Manag.* **2020**, *270*, 110870. [[CrossRef](#)]
16. Matos, J.; Laine, J.; Herrmann, J.M. Synergy effect in the photocatalytic degradation of phenol on a suspended mixture of titania and activated carbon. *Appl. Catal. B Environ.* **1998**, *18*, 281–291. [[CrossRef](#)]
17. Leary, R.; Westwood, A. Carbonaceous nanomaterials for the enhancement of TiO₂ photocatalysis. *Carbon* **2011**, *49*, 741–772. [[CrossRef](#)]
18. Onkani, S.P.; Diagboya, P.N.; Mtunzi, F.M.; Klink, M.J.; Olu-Owolabi, B.I.; Pakade, V. Comparative study of the photocatalytic degradation of 2-chlorophenol under UV irradiation using pristine and Ag-doped species of TiO₂, ZnO and ZnS photocatalysts. *J. Environ. Manag.* **2020**, *260*, 110145. [[CrossRef](#)]
19. Qiao, S.; Feng, C.; Guo, Y.; Chen, T.; Akram, N.; Zhang, Y.; Wang, W.; Yue, F.; Wang, J. CdS nanoparticles modified Ni@NiO spheres as photocatalyst for oxygen production in water oxidation system and hydrogen production in water reduction system. *Chem. Eng. J.* **2020**, *395*, 125068. [[CrossRef](#)]
20. Cao, D.; Wang, Q.; Wu, Y.; Zhu, S.; Jia, Y.; Wang, R. Solvothermal synthesis and enhanced photocatalytic hydrogen production of Bi/Bi₂MoO₆ co-sensitized TiO₂ nanotube arrays. *Sep. Purif. Technol.* **2020**, *250*, 117132. [[CrossRef](#)]
21. Faria, J.L.; Wang, W. Carbon materials in photocatalysis. In *Carbon Materials for Catalysis*; Serp, P., Figueiredo, J.L., Eds.; John Wiley & Sons: New York, NY, USA, 2009; pp. 481–506.
22. Ania, C.O.; Velasco, L.F.; Valdés-Solís, T. Photochemical behavior of carbon adsorbents. In *Novel Carbon Adsorbents*; Tascón, J.M.D., Ed.; Elsevier: Oxford, UK, 2012; pp. 521–547.
23. Velasco, L.F.; Parra, J.B.; Ania, C.O. Role of activated carbon features on the photocatalytic degradation of phenol. *Appl. Surf. Sci.* **2010**, *256*, 5254–5258. [[CrossRef](#)]
24. Velasco, L.F.; Fonseca, I.M.; Parra, J.B.; Lima, J.C.; Ania, C.O. Photochemical behaviour of activated carbons under UV irradiation. *Carbon* **2012**, *50*, 249–258. [[CrossRef](#)]
25. Velasco, L.F.; Maurino, V.; Laurenti, E.; Ania, C. Light-induced generation of radicals on semiconductor-free carbon photocatalysts. *Appl. Catal. A Gen.* **2013**, *453*, 310–315. [[CrossRef](#)]
26. Velasco, L.F.; Maurino, V.; Laurenti, E.; Fonseca, I.M.; Lima, J.C.; Ania, C.O. Photoinduced reactions occurring on activated carbons. A combined photooxidation and ESR study. *Appl. Catal. A Gen.* **2013**, *452*, 1–8. [[CrossRef](#)]
27. Araña, J.; Doña-Rodríguez, J.M.; Tello Rendón, E.; Garriga, I.; Cabo, C.; González-Díaz, O.; Herrera-Melián, J.A.; Pérez-Peña, J.; Colón, G.; Navío, J.A. TiO₂ activation by using activated carbon as a support: Part I. Surface characterisation and decantability study. *Appl. Catal. B Environ.* **2003**, *44*, 161–172. [[CrossRef](#)]
28. Keller, N.; Rebmann, G.; Barraud, E.; Zahraa, O.; Keller, V. Macroscopic carbon nanofibers for use as photocatalyst support. *Catal. Today* **2005**, *101*, 323–329. [[CrossRef](#)]
29. Ong, W.-J.; Tan, L.-L.; Ng, Y.H.; Yong, S.-T.; Chai, S.-P. Graphitic carbon nitride (g-C₃N₄)-based photocatalysts for artificial photosynthesis and environmental remediation: Are we a step closer to achieving sustainability? *Chem. Rev.* **2016**, *116*, 7159–7329. [[CrossRef](#)]
30. Wang, J.; Huang, H.; Xu, Z.; Kou, J.; Lu, C. The potential of carbon-based materials for photocatalytic application. *Curr. Org. Chem.* **2014**, *18*, 1346–1364. [[CrossRef](#)]
31. Chen, J.W.; Hui, C.; Keller, T.; Smith, G. Catalytic ozonation in aqueous system. *AIChE Symp. Ser.* **1977**, *73*, 206–212.

32. Andreatti, R.; Insola, A.; Caprio, V.; Marotta, R.; Tufano, V. The use of manganese dioxide as a heterogeneous catalyst for oxalic acid ozonation in aqueous solution. *Appl. Catal. A Gen.* **1996**, *138*, 75–81. [[CrossRef](#)]
33. Ma, J.; Graham, N.J.D. Preliminary investigation of manganese-catalyzed ozonation for the destruction of atrazine. *Ozone Sci. Eng.* **1997**, *19*, 227–236. [[CrossRef](#)]
34. Al Hayek, N.; Legube, B.; Doré, M. Ozonation catalytique (Fe(III)/Al₂O₃) du phénol y de ses produits d'ozonation. *Environ. Technol.* **1992**, *10*, 415–422.
35. Gracia, R.; Cortés, S.; Sarasa, J.; Ormad, P.; Ovelheiro, J.L. Catalytic ozonation with supported titanium dioxide. The stability of catalyst in water. *Ozone Sci. Eng.* **2000**, *22*, 185–193. [[CrossRef](#)]
36. Leitner, N.K.V.; Fu, H. pH effects on catalytic ozonation of carboxylic acids with metal on metal oxides catalysts. *Top. Catal.* **2005**, *33*, 249–256. [[CrossRef](#)]
37. Cooper, C.; Burch, R. Mesoporous materials for water treatment processes. *Water Res.* **1999**, *33*, 3689–3694. [[CrossRef](#)]
38. McKay, G.; McAleavey, G. Ozonation and carbon adsorption in a three-phase fluidised bed for colour removal from peat water. *Chem. Eng. Res. Des.* **1988**, *66*, 532–536.
39. Lin, S.H.; Lai, C.L. Kinetic characteristics of textile wastewater ozonation in fluidized and fixed activated carbon beds. *Water Res.* **2000**, *34*, 763–772. [[CrossRef](#)]
40. Rivera-Utrilla, J.; Sánchez-Polo, M. Ozonation of 1,3,6-naphthalenetrisulphonic acid catalysed by activated carbon in aqueous phase. *Appl. Catal. B Environ.* **2002**, *39*, 31–329. [[CrossRef](#)]
41. Orge, C.A.; Sousa, J.P.S.; Gonçalves, F.; Freire, C.; Órfão, J.J.M.; Pereira, M.F.R. Development of novel mesoporous carbon materials for the catalytic ozonation of organic pollutants. *Catal. Lett.* **2009**, *132*, 1–9. [[CrossRef](#)]
42. Liu, Z.Q.; Ma, J.; Cui, Y.H.; Zhang, B.P. Effect of ozonation pretreatment on the surface properties and catalytic activity of multi-walled carbon nanotube. *Appl. Catal. B Environ.* **2009**, *92*, 301–306. [[CrossRef](#)]
43. Ma, J.; Sui, M.; Zhang, T.; Guan, C. Effect of pH on MnO_x/GAC catalyzed ozonation for degradation of nitrobenzene. *Water Res.* **2005**, *39*, 779–786. [[CrossRef](#)]
44. Sánchez-Polo, M.; Rivera-Utrilla, J.; von Gunten, U. Metal-doped carbon aerogels as catalysts during ozonation processes in aqueous solutions. *Water Res.* **2006**, *40*, 3375–3384. [[CrossRef](#)]
45. Liu, Z.Q.; Ma, J.; Cui, Y.H. Carbon nanotube supported platinum catalysts for the ozonation of oxalic acid in aqueous solutions. *Carbon* **2008**, *46*, 890–897. [[CrossRef](#)]
46. Nidheesh, P.V. Graphene-based materials supported advanced oxidation processes for water and wastewater treatment: A review. *Environ. Sci. Pollut. Res.* **2017**, *24*, 27047–27069. [[CrossRef](#)]
47. Valdés, H.; Sánchez-Polo, M.; Rivera-Utrilla, J.; Zaror, C.A. Effect of ozone treatment on surface properties of activated carbon. *Langmuir* **2002**, *18*, 2111–2116. [[CrossRef](#)]
48. Sánchez-Polo, M.; Moncada, M.A.; Rivera-Utrilla, J.; Zaror, C.A. Effect of ozone and ozone/activated carbon treatments on genotoxic activity of naphthalenesulphonic acids. *J. Chem. Technol. Biot.* **2002**, *77*, 883–890.
49. Sánchez-Polo, M.; Rivera-Utrilla, J. Effect of the ozone-carbon reaction on the catalytic activity of activated carbon during degradation of 1,3,6-naphthalenetrisulphonic acid with ozone. *Carbon* **2003**, *41*, 303–307. [[CrossRef](#)]
50. Rivera-Utrilla, J.; Sánchez-Polo, M. Degradation and removal of naphthalenesulphonic acids by means of adsorption and ozonation catalyzed by activated carbon in water. *Water Resour. Res.* **2003**, *39*, 1232. [[CrossRef](#)]
51. Sánchez-Polo, M.; Rivera-Utrilla, J. The use of activated carbon and ozone in water treatment to eliminate naphthalenesulphonic acids. *Solid Fuel Chem.* **2004**, *1*, 26–34.
52. Sánchez-Polo, M.; Rivera-Utrilla, J. Ozonation of 1,3,6-naphthalenetrisulfonic acid in presence of heavy metals. *J. Chem. Technol. Biot.* **2004**, *79*, 902–909. [[CrossRef](#)]
53. Rivera-Utrilla, J.; Sánchez-Polo, M. Ozonation of naphthalenesulphonic acid in aqueous phase in the presence of basic activated carbons. *Langmuir* **2004**, *20*, 9217–9222. [[CrossRef](#)]
54. Sánchez-Polo, M.; Leyva-Ramos, R.; Rivera-Utrilla, J. Kinetics of 1,3,6-naphthalenetrisulphonic acid oxidation in presence of activated carbon. *Carbon* **2005**, *43*, 962–969. [[CrossRef](#)]
55. Sánchez-Polo, M.; von Gunten, U.; Rivera-Utrilla, J. Efficiency of activated carbon to transform ozone into ·OH radicals: Influence of operational parameters. *Water Res.* **2005**, *39*, 3189–3198. [[CrossRef](#)]

56. Méndez-Díaz, J.; Sánchez-Polo, M.; Rivera-Utrilla, J.; Bautista-Toledo, I.; Ferro-García, M.A. Ozonation in aqueous phase of sodium dodecylbenzenesulphonate in the presence of powdered activated carbon. *Carbon* **2005**, *43*, 3031–3034. [[CrossRef](#)]
57. Rivera-Utrilla, J.; Méndez-Díaz, J.; Sánchez-Polo, M.; Ferro-García, M.A.; Bautista-Toledo, I. Removal of the surfactant sodium dodecylbenzenesulphate from water by simultaneous use of ozone and powdered activated carbon: Comparison with system based on O₃ and O₃/H₂O₂. *Water Res.* **2006**, *40*, 1717–1725. [[CrossRef](#)]
58. Sánchez-Polo, M.; Salhi, E.; Rivera-Utrilla, J.; von Gunten, U. Combination of ozone with activated carbon as an alternative to conventional advanced oxidation processes. *Ozone Sci. Eng.* **2006**, *28*, 237–245. [[CrossRef](#)]
59. Sánchez-Polo, M.; Rivera-Utrilla, J. Ozonation of naphthalenetrisulphonic acid in the presence of activated carbons prepared from petroleum coke. *Appl. Catal. B Environ.* **2006**, *67*, 113–120. [[CrossRef](#)]
60. Sánchez-Polo, M.; Rivera-Utrilla, J. Photooxidation of naphthalenesulphonic acids in presence of transition metal-doped carbon aerogels. *Appl. Catal. B Environ.* **2006**, *69*, 93–100. [[CrossRef](#)]
61. Sánchez-Polo, M.; Rivera-Utrilla, J.; Méndez-Díaz, J.; López-Peñalver, J. Metal-doped carbon aerogels: New materials for water treatment. *Ind. Eng. Chem. Res.* **2008**, *47*, 6001–6005. [[CrossRef](#)]
62. Sánchez-Polo, M.; Rivera-Utrilla, J.; Prados-Joya, G.; Ferro-García, M.A.; Bautista-Toledo, I. Removal of pharmaceutical compounds, nitroimidazoles, from waters by using the ozone/carbon system. *Water Res.* **2008**, *42*, 4163–4171.
63. Rivera-Utrilla, J.; Sánchez-Polo, M.; Méndez-Díaz, J.D. Ozone decomposition by catalysts and its application in water treatment: An overview. In *Ozone Depletion, Chemistry and Impacts*; Bakker, S.H., Ed.; Nova Science Publishers, Inc.: New York, NY, USA, 2008; pp. 17–51.
64. Sánchez-Polo, M.; Méndez-Díaz, J.D.; Rivera-Utrilla, J.; Bautista-Toledo, I.; Ferro-García, M.A. Influence of presence of tannic acid on removal of sodium dodecylbenzenesulphonate by O₃ and advanced oxidation processes. *J. Chem. Technol. Biotechnol.* **2009**, *84*, 367–375. [[CrossRef](#)]
65. Rivera-Utrilla, J.; Sánchez-Polo, M.; Prados-Joya, G.; Ferro-García, M.A.; Bautista-Toledo, I. Removal of tinidazole from water by using ozone and activated carbon in dynamic regime. *J. Hazard. Mater.* **2010**, *174*, 880–886. [[CrossRef](#)]
66. Rivera-Utrilla, J.; Sánchez-Polo, M.; Gómez-Serrano, V.; Álvarez, P.M.; Alvim-Ferraz, M.C.M.; Dias, J.M. Activated carbon modifications to enhance its water treatment applications. An overview. *J. Hazard. Mater.* **2011**, *187*, 1–23. [[CrossRef](#)]
67. Rivera-Utrilla, J.; Sánchez-Polo, M.; Bautista-Toledo, M.I.; Méndez-Díaz, J.D. Enhanced oxidation of sodium dodecylbenzenesulfonate aqueous solution using ozonation catalyzed by base treated zeolite. *Chem. Eng. J.* **2012**, *180*, 204–209. [[CrossRef](#)]
68. Medellín-Castillo, N.A.; Ocampo-Pérez, R.; Leyva-Ramos, R.; Sánchez-Polo, M.; Rivera-Utrilla, J.; Méndez-Díaz, J.D. Removal of diethyl phthalate from water solution by adsorption, photo-oxidation, ozonation and advanced oxidation process (UV/H₂O₂, O₃/H₂O₂ and O₃/activated carbon). *Sci. Total Environ.* **2013**, *442*, 26–35. [[CrossRef](#)]
69. Velo-Gala, I.; López-Peñalver, J.J.; Sánchez-Polo, M.; Rivera-Utrilla, J. Activated carbon as photocatalyst of reactions in aqueous phase. *Appl. Catal. B Environ.* **2013**, *142–143*, 694–704. [[CrossRef](#)]
70. Velo-Gala, I.; López-Peñalver, J.J.; Sánchez-Polo, M.; Rivera-Utrilla, J. Role of activated carbon on micropollutants degradation by different radiation processes. *Mediterr. J. Chem.* **2015**, *4*, 68–80. [[CrossRef](#)]
71. Ocampo-Perez, R.; Rivera-Utrilla, J.; Abdel Daiem, M.M.; Sánchez-Polo, M. Integrated technologies based on the use of activated carbon and radiation to remove contaminants present in landfill leachates. In *Landfills and Recycling Centers. Processing Systems, Impact on the Environment and Adverse Health Effects*; Jackson, C.H., Ed.; Nova Science Publishers, Inc.: New York, NY, USA, 2015; pp. 69–109.
72. Orellana-García, F.; Álvarez, M.A.; López-Ramón, M.V.; Rivera-Utrilla, J.; Sánchez-Polo, M. Photoactivity of organic xerogels and aerogels in the photodegradation of herbicides from waters. *Appl. Catal. B Environ.* **2016**, *181*, 94–102. [[CrossRef](#)]
73. Salazar-Rábago, J.J.; Sánchez-Polo, M.; Rivera-Utrilla, J.; Leyva-Ramos, R.; Ocampo-Pérez, R. Role of ¹[O₂]* in chlortetracycline degradation by solar radiation assisted by ruthenium metal complexes. *Chem. Eng. J.* **2016**, *284*, 896–904. [[CrossRef](#)]

74. Salazar-Rábago, J.J.; Sánchez-Polo, M.; Rivera-Utrilla, J.; Leyva-Ramos, R.; Ocampo-Pérez, R.; Carrasco-Marin, F. Organic xerogels doped with Tris(2,2'-bipyridine) ruthenium (II) as hydroxyl radical promoters: Synthesis, characterization, and photoactivity. *Chem. Eng. J.* **2016**, *306*, 289–297. [[CrossRef](#)]
75. Velo-Gala, I.; López-Peñalver, J.J.; Sánchez-Polo, M.; Rivera-Utrilla, J. Role of activated carbon surface chemistry in its photocatalytic activity and the generation of oxidant radicals under UV or solar radiation. *Appl. Catal. B Environ.* **2017**, *207*, 412–423. [[CrossRef](#)]
76. Acosta-Rangel, A.; Sánchez-Polo, M.; Polo, A.M.S.; Rivera-Utrilla, J.; Berber-Mendoza, M.S. Tinidazole degradation assisted by solar radiation and iron-doped silica xerogels. *Chem. Eng. J.* **2018**, *344*, 21–33. [[CrossRef](#)]
77. Álvarez, M.A.; Orellana-García, F.; López-Ramón, M.V.; Rivera-Utrilla, J.; Sánchez-Polo, M. Influence of operational parameters on photocatalytic amitrole degradation using nickel organic xerogel under UV irradiation. *Arab. J. Chem.* **2018**, *11*, 564–572. [[CrossRef](#)]
78. Martínez-Costa, J.I.; Rivera-Utrilla, J.; Leyva-Ramos, R.; Sánchez-Polo, M.; Velo-Gala, I. Individual and simultaneous degradation of antibiotics sulfamethoxazole and trimethoprim by UV and solar radiation in aqueous solution using bentonite and vermiculite as photocatalysts. *Appl. Clay Sci.* **2018**, *160*, 217–225. [[CrossRef](#)]
79. López-Ramón, M.V.; Rivera-Utrilla, J.; Sánchez-Polo, M.; Polo, A.M.S.; Mota, A.J.; Orellana-García, F.; Álvarez, M.A. Photocatalytic oxidation of diuron using nickel organic xerogel under simulated solar irradiation. *Sci. Total Environ.* **2019**, *650*, 1207–1215. [[CrossRef](#)] [[PubMed](#)]
80. Fernández-Perales, M.; Rozalen, M.; Sánchez-Polo, M.; Rivera-Utrilla, J.; López-Ramón, M.V.; Álvarez, M.A. Solar degradation of sulfamethazine using rGO/Bi composite photocatalysts. *Catalysts* **2020**, *10*, 573. [[CrossRef](#)]
81. Ruidíaz-Martínez, M.; Álvarez, M.A.; López-Ramón, M.V.; Cruz-Quesada, G.; Rivera-Utrilla, J.; Sánchez-Polo, M. Hydrothermal synthesis of rGO-TiO₂ composites as high-performance UV photocatalysts for ethylparaben degradation. *Catalysts* **2020**, *10*, 520. [[CrossRef](#)]
82. Ahmed, S.; Rasul, M.G.; Brown, R.; Hashib, M.A. Influence of parameters on the heterogeneous photocatalytic degradation of pesticides and phenolic contaminants in wastewater: A short review. *J. Environ. Manag.* **2011**, *92*, 311–330. [[CrossRef](#)]
83. Ledezma-Estrada, A.; Li, Y.Y.; Wang, A. Biodegradability enhancement of wastewater containing cefalexin by means of the electro-Fenton oxidation process. *J. Hazard. Mater.* **2012**, *227–228*, 41–48. [[CrossRef](#)]
84. Sacco, O.; Vaiano, V.; Rizzo, L.; Sannino, D. Photocatalytic activity of a visible light active structured photocatalyst developed for municipal wastewater treatment. *J. Clean. Prod.* **2018**, *175*, 38–49. [[CrossRef](#)]
85. Velo-Gala, I.; López-Peñalver, J.J.; Sánchez-Polo, M.; Rivera-Utrilla, J. Surface modifications of activated carbon by gamma radiation. *Carbon* **2014**, *67*, 236–249. [[CrossRef](#)]
86. Kralchevska, K.; Milanova, M.; Tsvetkov, M.; Dimitrov, D.; Todorovsky, D. Influence of gamma-irradiation on the photocatalytic activity of Degussa P25 TiO₂. *J. Mater. Sci.* **2012**, *47*, 4936–4945. [[CrossRef](#)]
87. Tolosana-Moranchel, A.; Casas, J.A.; Carbajo, J.; Faraldos, M.; Bahamonde, A. Influence of TiO₂ optical parameters in a slurry photocatalytic reactor: Kinetic modelling. *Appl. Catal. B Environ.* **2017**, *200*, 164–173. [[CrossRef](#)]
88. Buxton, G.V.; Greenstock, C.L.; Helman, W.P.; Ross, A.B. Critical Review of rate constants for reactions of hydrated electrons, hydrogen atoms and hydroxyl radicals (OH/O[•]) in aqueous solutions. *J. Phys. Chem. Ref. Data* **1988**, *17*, 2593–2600. [[CrossRef](#)]
89. Zhang, D.; Qiu, R.; Song, L.; Eric, B.; Mo, Y.; Huang, X. Role of oxygen active species in the photocatalytic degradation of phenol using polymer sintetized TiO₂ under visible light irradiation. *J. Hazard. Mater.* **2009**, *163*, 843–847. [[CrossRef](#)] [[PubMed](#)]
90. Moreno-Castilla, C.; Maldonado-Hódar, F.J. Carbon aerogels for catalysis applications: An overview. *Carbon* **2005**, *43*, 455–465. [[CrossRef](#)]
91. Moreno-Castilla, C.; Maldonado-Hódar, F.J.; Rivera-Utrilla, J.; Rodríguez-Castellón, E. Group 6 metal oxide-carbon aerogels. Their synthesis, characterization and catalytic activity in the skeletal isomerization of 1-butene. *Appl. Catal. A Gen.* **1999**, *183*, 345–356. [[CrossRef](#)]
92. López, R.; Gómez, R. Band-gap energy estimation from diffuse reflectance measurements on sol-gel and commercial TiO₂: A comparative study. *J. Sol-Gel Sci. Technol.* **2012**, *61*, 1–7. [[CrossRef](#)]

93. Rodríguez-Reinoso, F.; Linares-Solano, A. Microporous structure of activated carbons as revealed by adsorption methods. In *Chemistry and Physics of Carbon*; Walker, P.L., Ed.; Marcel Dekker: New York, NY, USA, 1989; Volume 21, pp. 146–195.
94. Zielke, U.; Huttinger, J.; Hoffman, W.P. Surface-oxidized carbon fibers: I. Surface structure and chemistry. *Carbon* **1994**, *34*, 983–998. [[CrossRef](#)]
95. Tratnyek, P.G.; Hoigné, J. Photo-oxidation of 2,4,6-trimethylphenol in aqueous laboratory solutions and natural waters: Kinetics of reaction with singlet oxygen. *J. Photochem. Photobiol. A Chem.* **1994**, *84*, 153–160. [[CrossRef](#)]
96. Stefan, M.I.; Bolton, J.R. Reinvestigation of the acetone degradation mechanism in dilute aqueous solution by the UV/H₂O₂ Process. *Environ. Sci. Technol.* **1999**, *33*, 870–873. [[CrossRef](#)]
97. Hoigné, J. Inter-calibration of OH radical sources and water quality parameters. *Water Sci. Technol.* **1997**, *35*, 1–8. [[CrossRef](#)]
98. Moreno-Castilla, C.; Maldonado-Hódar, F.J.; Pérez-Cadenas, A. Physicochemical surface properties of Fe, Co, Ni, and Cu-doped monolithic organic aerogels. *Langmuir* **2003**, *19*, 5650–5655. [[CrossRef](#)]
99. Czakkel, O.; Marthi, K.; Geissler, E.; László, K. Influence of drying on the morphology of resorcinol-formaldehyde-based carbon gels. *Micropor. Mesopor. Mater.* **2005**, *86*, 124–133. [[CrossRef](#)]
100. Milowska, K.Z.; Majewski, J.A. Functionalization of carbon nanotubes with –CH_n, –NH_n fragments, –COOH and –OH groups. *J. Chem. Phys.* **2013**, *138*, 194704–194714. [[CrossRef](#)] [[PubMed](#)]
101. Parra, S.; Stanca, S.E.; Guasaquillo, I.; Thampi, K.R. Photocatalytic degradation of atrazine using suspended and supported TiO₂. *Appl. Catal. B Environ.* **2004**, *51*, 107–116. [[CrossRef](#)]
102. Fenoll, J.; Hellín, P.; Martínez, C.M.; Flores, P.; Navarro, S. Semiconductor-sensitized photodegradation of s-triazine and chloroacetanilide herbicides in leaching water using TiO₂ and ZnO as catalyst under natural sunlight. *J. Photochem. Photobiol. A* **2012**, *238*, 81–87. [[CrossRef](#)]
103. Wei, L.; Shifu, C.; Wei, Z.; Sujuan, Z. Titanium dioxide mediated photocatalytic degradation of methamidophos in aqueous phase. *J. Hazard. Mater.* **2009**, *164*, 154–160. [[CrossRef](#)]
104. Wu, R.; Chen, C.; Chen, M.; Lu, C. Titanium dioxide-mediated heterogeneous photocatalytic degradation of terbufos: Parameter study and reaction pathways. *J. Hazard. Mater.* **2009**, *162*, 945–953. [[CrossRef](#)]
105. Lin, C.; Lin, K. Photocatalytic oxidation of toxic organohalides with TiO₂/UV: The effects of humic substances and organic mixtures. *Chemosphere* **2007**, *66*, 1872–1877. [[CrossRef](#)]
106. Chen, J.; Wang, D.; Zhu, M.; Gao, C. Photocatalytic degradation of dimethoate using nanosized TiO₂ powder. *Desalination* **2007**, *207*, 87–94. [[CrossRef](#)]
107. Orellana-García, F.; Álvarez, M.A.; López-Ramón, M.V.; Rivera-Utrilla, J.; Sánchez-Polo, M. Effect of HO[•], SO₄^{•-} and CO₃^{•-}/HCO₃[•] radicals on the photodegradation of the herbicide amitrole by UV radiation in aqueous solution. *Chem. Eng. J.* **2015**, *267*, 182–190. [[CrossRef](#)]
108. Wang, H.L.; Liang, W.Z.; Jiang, W.F. Solar photocatalytic degradation of 2-sec-butyl-4,6-dinitrophenol using TiO₂/SiO₂ aerogel composite photocatalysts. *Mater. Chem. Phys.* **2011**, *130*, 1372–1379. [[CrossRef](#)]
109. Shi, L.; Yang, L.; Zhang, H.; Chang, K.; Zhao, G.; Kako, T. Implantation of iron(III) in porphyrinic metal organic frameworks for highly improved photocatalytic performance. *Appl. Catal. B Environ.* **2018**, *224*, 60–68. [[CrossRef](#)]
110. de Escobar, C.C.; dos Santos, F.P.; dos Santos, J.H.Z. Effect of the amount and time of addition of a dye template on the adsorption and photocatalytic performance of molecularly imprinted silica. *J. Environ. Chem. Eng.* **2018**, *6*, 190–196. [[CrossRef](#)]
111. Rebbouh, L.; Rosso, V.; Renotte, Y.; Lion, Y.; Grandjean, F.; Heinrichs, B.; Pirard, J.-P.; Delwiche, J.; Hubin-Franskin, M.-J.; Long, G.J. The nonlinear optical, magnetic, and Mössbauer spectral properties of some iron (III) doped silica xerogels. *J. Mater. Sci.* **2006**, *41*, 2839–2849. [[CrossRef](#)]
112. Wang, Y.; Zhang, R.; Li, J.; Li, L.; Lin, S. First-principles study of transition metal doped anatase TiO₂. *Nanoscale Res. Lett.* **2014**, *9*, 46. [[CrossRef](#)]
113. Moradi, V.; Jun, M.B.; Blackburn, A.; Herring, R.A. Significant improvement in visible light photocatalytic activity of Fe doped TiO₂ using an acid treatment process. *Appl. Surf. Sci.* **2018**, *427*, 791–799. [[CrossRef](#)]
114. Rahmani, H.; Gholami, M.; Mahvi, A.; Alimohammadi, M.; Azarian, G.; Esrafil, A.; Rahmani, K.; Farzadkia, M. Tinidazole removal from aqueous solution by sonolysis in the presence of hydrogen peroxide. *Bull. Environ. Contam. Toxicol.* **2014**, *92*, 341–346. [[CrossRef](#)]

115. Mangayayam, M.; Kiwi, J.; Giannakis, S.; Pulgarin, C.; Zivkovic, I.; Magrez, A.; Rtimi, S. FeO_x magnetization enhancing E. coli inactivation by orders of magnitude on Ag-TiO₂ nanotubes under sunlight. *Appl. Catal. B Environ.* **2017**, *202*, 438–445. [[CrossRef](#)]
116. El mehdi Benacherine, M.; Debbache, N.; Ghoul, I.; Mameri, Y. Heterogeneous photoinduced degradation of amoxicillin by Goethite under artificial and natural irradiation. *J. Photochem. Photobiol. A* **2017**, *335*, 70–77. [[CrossRef](#)]
117. Ocampo-Gaspar, M.; Cano-Guzmán, C.F.; Payan-Martínez, L.F.; González-Reyes, L.; Hernández-Pérez, I.; Garibay-Febles, V.; Pérez-Orozco, J.P.; Cabrera-Lara, L.I.; Ramón-García, M.I.; Galicia-Luis, L.; et al. Sizing the Fenton's catalyst. *J. Photochem. Photobiol. A* **2018**, *353*, 527–535. [[CrossRef](#)]
118. Schultz, D.M.; Yoon, T.P. Solar synthesis: Prospects in visible light photocatalysis. *Science* **2014**, *343*, 1–8. [[CrossRef](#)] [[PubMed](#)]
119. Kalyanasundaram, K. Photophysics, photochemistry and solar energy conversion with tris(bipyridyl)ruthenium(II) and its analogues. *Coord. Chem. Rev.* **1982**, *46*, 159–244. [[CrossRef](#)]
120. Miskoski, S.; Sanchez, E.; Garavano, M.; Lopez, M.; Soltermann, A.T.; Garcia, N.A. Singlet molecular oxygen-mediated photo-oxidation of tetracyclines: Kinetics, mechanism and microbiological implications. *J. Photochem. Photobiol. B Biol.* **1998**, *43*, 164–171. [[CrossRef](#)]
121. Klavarioti, M.; Mantzavinos, D.; Kassinos, D. Removal of residual pharmaceuticals from aqueous systems by advanced oxidation processes. *Environ. Int.* **2009**, *35*, 402–417. [[CrossRef](#)]
122. Raizada, P.; Sudhaik, A.; Singh, P. Photocatalytic water decontamination using Graphene and ZnO coupled: A review. *Mater. Sci. Technol.* **2019**, *2*, 509–525. [[CrossRef](#)]
123. Upadhyay, R.K.; Soin, N.; Roy, S.S. Role of graphene metal oxide composites as photocatalysts, adsorbents and disinfectants in water treatment: In review. *RSC Adv.* **2014**, *4*, 3823–3848. [[CrossRef](#)]
124. Pastrana-Martínez, L.M.; Morales-Torres, S.; Likodimos, V.; Figueiredo, J.L.; Faria, J.L.; Falaras, P.; Silva, A.M.T. Advanced nanostructured photocatalysts based on reduced graphene oxide-TiO₂ composites for degradation of diphenhydramine pharmaceutical and methyl orange dye. *Appl. Catal. B Environ.* **2012**, *123–124*, 241–256. [[CrossRef](#)]
125. Alamelu, K.; Raja, V.; Shiamala, L.; Jaffar Ali, B.M. Biphasic TiO₂ nanoparticles decorated graphene nanosheets for visible light driven photocatalytic degradation of organic dyes. *Appl. Surf. Sci.* **2018**, *430*, 145–154. [[CrossRef](#)]
126. Petala, A.; Noe, A.; Frontitis, Z.; Drivas, C.; Kennou, S.; Mantzavinos, D.; Kondarides, D.I. Synthesis and characterization of CoO_x/BiVO₄ photocatalysts for the degradation of propyl paraben. *J. Hazard. Mater.* **2019**, *372*, 198–206. [[CrossRef](#)]
127. Bruny, R.; Bourbigot, M.M.; Doré, M. Oxidation of organic compounds through the combination ozone-hydrogen peroxide. *Ozone Sci. Eng.* **1985**, *7*, 241–257.
128. Beltrán, F.J.; García Araya, J.F.; Acedo, B. Advanced oxidation of atrazine in water. II Ozonation combined with ultraviolet radiation. *Water Res.* **1994**, *28*, 2165–2174. [[CrossRef](#)]
129. Logemann, F.P.; Anne, J.H.J. Water treatment with a fixed bed catalytic ozonation process. *Water Sci. Technol.* **1997**, *35*, 353–360. [[CrossRef](#)]
130. Jans, U.; Hoigné, J. Activated carbon and carbon black catalyzed transformation of aqueous ozone into oh-radicals. *Ozone Sci. Eng.* **1998**, *20*, 67–90. [[CrossRef](#)]
131. Álvarez, P.M.; García-Araya, J.F.; Beltrán, F.J.; Giráldez, I.; Jaramillo, J.; Gómez-Serrano, V. The influence of various factors on aqueous ozone decomposition by granular activated carbons and the development of a mechanistic approach. *Carbon* **2006**, *44*, 3102–3112. [[CrossRef](#)]
132. Yeber, M.C.; Rodríguez, J.; Freer, J.; Baeza, J.; Durán, N.; Mansilla, H.D. Toxicity abatement and biodegradability by advanced chemical oxidation. *Water. Sci. Technol.* **1999**, *40*, 337–342. [[CrossRef](#)]
133. Staehelin, J.; Hoigne, J. Decomposition of ozone in water in the presence of organic solutes acting as promoters and inhibitors of radical chain reactions. *Environ. Sci. Technol.* **1985**, *19*, 1206–1213. [[CrossRef](#)]
134. Morgan, M.E.; Jenkins, R.G.; Walter, P.L. Inorganic constituents in American lignites. *Fuel* **1981**, *60*, 189–193. [[CrossRef](#)]
135. Moreno-Castilla, C.; Carrasco-Marín, F.; Maldonado-Hódar, F.J.; Rivera-Utrilla, J. Effects of non-oxidant and oxidant acid treatments on the surface properties of an activated carbon with very low ash content. *Carbon* **1998**, *36*, 145–151. [[CrossRef](#)]

136. Elovitz, M.S.; von Gunten, U. Hydroxyl radical/ozone ratios during ozonation processes. I. The R_{ct} concept. *Ozone Sci. Eng.* **1999**, *21*, 239–260. [[CrossRef](#)]
137. von Gunten, U. Ozonation of drinking water: Part II. Disinfection and by-product formation in presence of bromide, iodide or chlorine. *Water Res.* **2003**, *37*, 1469–1487. [[CrossRef](#)]
138. Li, W.; Reichenauer, G.; Fricke, J. Carbon aerogels derived from cresol-resorcinol-formaldehyde for supercapacitors. *Carbon* **2002**, *40*, 2955–2959. [[CrossRef](#)]
139. Rotter, H.; Landau, M.V.; Carrera, M.; Goldfarb, D.; Herskowitz, M. High surface area chromia aerogel efficient catalyst and catalyst support for ethylacetate combustion. *Appl. Catal. B Environ.* **2004**, *47*, 111–126. [[CrossRef](#)]
140. Yao, C.C.D.; Haag, W.R. Rate constants for direct reactions of ozone with several drinking water contaminants. *Water Res.* **1991**, *27*, 761–773.
141. Andreozzi, R.; Insola, A.; Caprio, V.; D'Amore, G. The kinetics of Mn(II)-catalysed ozonation of oxalic acid in aqueous solution. *Water Res.* **1992**, *26*, 917–921. [[CrossRef](#)]
142. Ma, J.; Graham, N.J.D. Degradation of atrazine by manganese-catalysed ozonation-influence of radical scavengers. *Water Res.* **2000**, *34*, 3822–3828. [[CrossRef](#)]
143. Smit, B.; Maesen, T.L.M. Towards a molecular understanding of shape selectivity. *Nature* **2008**, *451*, 671–678. [[CrossRef](#)]
144. Valdés, H.; Farfán, V.J.; Manoli, J.A.; Zaror, C.A. Catalytic ozone aqueous decomposition promoted by natural zeolite and volcanic sand. *J. Hazard. Mater.* **2009**, *165*, 915–922. [[CrossRef](#)]
145. Sagehashi, M.; Shiraiishi, K.; Fujita, H.; Fujii, T.; Sakoda, A. Adsorptive ozonation of 2-methylisoborneol in natural water with preventing bromate formation. *Water Res.* **2005**, *39*, 3900–3908. [[CrossRef](#)]
146. Sano, N.; Yamamoto, T.; Yamamoto, D.; Kim, S.-I.; Eiad-Ua, A.; Shinomiya, H.; Nakaiwa, M. Degradation of aqueous phenol by simultaneous use of ozone with silica-gel and zeolite. *Chem. Eng. Process.* **2007**, *46*, 513–519. [[CrossRef](#)]
147. Beltrán, F.J.; García-Araya, J.F.; Álvarez, P.M. Sodium dodecylbenzenesulfonate removal from water and wastewater. 1. Kinetics of decomposition by ozonation. *Ind. Eng. Chem. Res.* **2000**, *39*, 2214–2220. [[CrossRef](#)]
148. Von Gunten, U. Ozonation of drinking water: Part I. Oxidation kinetics and product formation. *Water Res.* **2003**, *37*, 1443–1467. [[CrossRef](#)]
149. Yang, Z.; Zhang, C.; Zeng, G.; Tan, X.; Wang, H.; Huang, D.; Yang, K.; Wei, J.; Ma, C.; Nie, K. Design and engineering of layered double hydroxide based catalysts for water depollution by advanced oxidation processes: A review. *J. Mater. Chem. A* **2020**, *8*, 4141–4173. [[CrossRef](#)]
150. Rekhate, C.V.; Srivastava, J.K. Recent advances in ozone-based advanced oxidation processes for treatment of wastewater—A review. *Chem. Eng. J. Adv.* **2020**, *3*, 100031. [[CrossRef](#)]
151. Giwa, A.; Yusuf, A.; Balogun, H.A.; Sambudi, N.S.; Bilad, M.R.; Adeyemi, I.; Chakraborty, S.; Curcio, S. Recent advances in advanced oxidation processes for removal of contaminants from water: A comprehensive review. *Process. Saf. Environ.* **2021**, *146*, 220–256. [[CrossRef](#)]
152. Tiwaria, S.K.; Sahoo, S.; Wang, N.; Huczko, A. Graphene research and their outputs: Status and prospect. *J. Sci. Adv. Mater.* **2020**, *5*, 10–29. [[CrossRef](#)]
153. Karim, A.V.; Selvaraj, A. Graphene composites in photocatalytic oxidation of aqueous organic contaminants—A state of art. *Process Saf. Environ.* **2021**, *146*, 136–160. [[CrossRef](#)]
154. Rodrigues, A.F.; Newman, L.; Jasim, D.; Mukherjee, S.P.; Wang, J.; Vacchi, I.A.; Ménard-Moyon, C.; Bianco, A.; Fadeel, B.; Kostarelos, K.; et al. Size-Dependent Pulmonary Impact of Thin Graphene Oxide Sheets in Mice: Toward Safe-by-Design. *Adv. Sci.* **2020**, *7*, 1903200. [[CrossRef](#)]
155. Liao, K.H.; Lin, Y.S.; MacOsco, C.W.; Haynes, C.L. Cytotoxicity of graphene oxide and graphene in human erythrocytes and skin fibroblasts. *ACS Appl. Mater. Interfaces* **2011**, *3*, 2607–2615. [[CrossRef](#)]
156. Ahmed, F.; Rodrigues, D.F. Investigation of acute effects of graphene oxide on wastewater microbial community: A case study. *J. Hazard. Mater.* **2013**, *256–257*, 33–39. [[CrossRef](#)]
157. Kryuchkova, M.; Danilushkina, A.; Lvov, Y.; Fakhrullin, R. Evaluation of toxicity of nanoclays and graphene oxide in vivo: A Paramecium caudatum study. *Environ. Sci. Nano* **2016**, *3*, 442–452. [[CrossRef](#)]
158. Bano, Z.; Mazari, S.A.; Saeed, R.M.Y.; Majeed, M.A.; Xia, M.; Memon, A.Q.; Abro, R.; Wang, F. Water decontamination by 3D graphene based materials: A review. *J. Water Process. Eng.* **2020**, *36*, 101404. [[CrossRef](#)]

159. Yousefi, N.; Lu, X.; Elimelech, M.; Tufenkji, N. Environmental performance of graphene-based 3D macrostructures. *Nat. Nanotechnol.* **2019**, *14*, 107–119. [[CrossRef](#)] [[PubMed](#)]
160. Saufi, S.; Ismail, A. Fabrication of carbon membranes for gas separation—a review. *Carbon* **2004**, *42*, 241–259. [[CrossRef](#)]
161. Liang, P.; Wei, A.; Zhang, Y.; Wu, J.; Zhang, X.; Li, S. Immobilisation of TiO₂ films on activated carbon fibres by a hydrothermal method for photocatalytic degradation of toluene. *Micro Nano Lett.* **2016**, *11*, 539–544. [[CrossRef](#)]
162. Stolz, A.; Floch, S.L.; Reinert, L.; Ramos, S.M.M.; Tuailon-Combes, J.; Soneda, Y.; Chaudet, P.; Baillis, D.; Blanchard, N.; Duclaux, L.; et al. Melamine-derived carbon sponges for oil-water separation. *Carbon* **2016**, *107*, 198–208. [[CrossRef](#)]
163. Yang, Y.; Chiang, K.; Burke, N. Porous carbon-supported catalysts for energy and environmental applications: A short review. *Catal. Today* **2011**, *178*, 197–205. [[CrossRef](#)]
164. Vottero, E.; Carosso, M.; Jiménez-Ruiz, M.; Pellegrini, R.; Groppo, E.; Piovano, A. How do the graphenic domains terminate in activated carbons and carbon-supported metal catalysts? *Carbon* **2020**, *169*, 357–369. [[CrossRef](#)]
165. Raji, M.; Mirbagheri, S.A.; Ye, F.; Dutta, J. Nano zero-valent iron on activated carbon cloth support as Fenton-like catalyst for efficient color and COD removal from melanoidin wastewater. *Chemosphere* **2021**, *263*, 127945. [[CrossRef](#)]
166. Malik, S.N.; Ghosh, P.C.; Vaidya, A.N.; Mudliar, S.N. Hybrid ozonation process for industrial wastewater treatment: Principles and applications: A review. *J. Water Process Eng.* **2020**, *35*, 101193. [[CrossRef](#)]
167. Wang, B.; Zhang, H.; Wang, F.; Xiong, X.; Tian, K.; Sun, Y.; Yu, T. Application of heterogeneous catalytic ozonation for Refractory Organics in Wastewater. *Catalysts* **2019**, *9*, 241. [[CrossRef](#)]
168. Lee, J.H.; Park, S.J. Recent advances in preparations and applications of carbon aerogels: A review. *Carbon* **2020**, *163*, 1–18. [[CrossRef](#)]
169. Maleki, H.; Hüsing, N. Current status, opportunities and challenges in catalytic and photocatalytic applications of aerogels: Environmental protection aspects. *Appl. Catal. B Environ.* **2018**, *221*, 530–555. [[CrossRef](#)]
170. Suh, D.J. Catalytic applications of composite aerogels. *J. Non-Cryst. Solids* **2004**, *350*, 314–319. [[CrossRef](#)]
171. Hasanpour, M.; Hatami, M. Photocatalytic performance of aerogels for organic dyes removal from wastewaters: Review study. *J. Mol. Liq.* **2020**, *309*, 113094. [[CrossRef](#)]
172. Hu, E.; Shang, S.M.; Tao, X.; Jiang, S.; Chiu, K.L. Regeneration and reuse of highly polluting textile dyeing effluents through catalytic ozonation with carbon aerogel catalysts. *J. Clean. Prod.* **2016**, *137*, 1055–1065. [[CrossRef](#)]
173. Xinbo, E.H.; Shang, W.S.; Tao, X.; Jiang, S.; Gan, L. Catalytic ozonation of simulated textile dyeing wastewater using mesoporous carbon aerogel supported copper oxide catalyst. *J. Clean. Prod.* **2016**, *112*, 4710–4718.
174. Jiang, L.; Wang, Q.; Zhou, M.; Liang, L.; Li, K.; Yang, W.; Lu, X.; Zhang, Y. Role of adsorption and oxidation in porous carbon aerogel/persulfate system for non-radical degradation of organic contaminant. *Chemosphere* **2020**, *241*, 125066. [[CrossRef](#)]
175. Jiang, L.; Zhang, Y.; Zhou, M.; Liang, L.; Li, K. Oxidation of Rhodamine B by persulfate activated with porous carbon aerogel through a non-radical mechanism. *J. Hazard. Mater.* **2018**, *358*, 53–61. [[CrossRef](#)]
176. Rashid, T.; Iqbal, D.; Hazafa, A.; Hussain, S.; Sher, F.; Sher, F. Formulation of zeolite supported nano-metallic catalyst and applications in textile effluent treatment. *J. Environ. Chem. Eng.* **2020**, *8*, 104023. [[CrossRef](#)]
177. Gonzalez-Olmos, R.; Holzer, F.; Kopinke, F.D.; Georgi, A. Indications of the reactive species in a heterogeneous Fenton-like reaction using Fe-containing zeolites. *Appl. Catal. A* **2011**, *398*, 44–53. [[CrossRef](#)]
178. Bandala, E.R.; Sadek, R.; Gurgul, J.; Łątka, K.; Zimowska, M.; Valentin, L.; Rodriguez-Narvaez, O.M.; Dzwigaj, S. Assessment of the capability of Fe and Al modified BEA zeolites to promote advanced oxidation processes in aqueous phase. *Chem. Eng. J.* **2020**. [[CrossRef](#)]
179. Ismail, A.A.; Bahnemann, D.W. Photochemical splitting of water for hydrogen production by photocatalysis: A review. *Sol. Energy Mat. Sol. C* **2014**, *128*, 85–101. [[CrossRef](#)]
180. Koyyada, G.; Pilli, N.S.; Jung, J.H.; Mandari, K.K.; Shanigaram, B.; Chandrasekharam, M. Shining light on panchromatic ruthenium sensitizers towards dye-sensitized photocatalytic hydrogen evolution. *Int. J. Hydrog. Energy* **2018**, *43*, 6963–6976. [[CrossRef](#)]

181. Luis, E.T.; Iranmanesh, H.; Beves, J.E. Photosubstitution reactions in ruthenium(II) trisdiimine complexes: Implications for photoredox catalysis. *Polyhedron* **2019**, *160*, 1–9. [[CrossRef](#)]
182. Bolobajev, J.; Kask, M.; Kreek, K.; Kulp, M.; Koel, M.; Goi, A. Metal-doped organic aerogels for photocatalytic degradation of trimethoprim. *Chem. Eng. J.* **2019**, *357*, 120–128. [[CrossRef](#)]
183. Justh, N.; Mikula, G.J.; Bakos, L.P.; Nagy, B.; László, K.; Parditka, B.; Erdélyi, Z.; Takáts, V.; Mizsei, J.; Szilágyi, I.M. Photocatalytic properties of TiO₂@polymer and TiO₂@carbon aerogel composites prepared by atomic layer deposition. *Carbon* **2019**, *147*, 476–482. [[CrossRef](#)]
184. Bakos, L.P.; Mensah, J.; László, K.; Parditka, B.; Erdélyi, Z.; Székely, E.; Lukács, I.; Kónya, Z.; Cserháti, C.; Zhou, C.; et al. Nitrogen doped carbon aerogel composites with TiO₂ and ZnO prepared by atomic layer deposition. *J. Mater. Chem. C* **2020**, *8*, 6891–6899. [[CrossRef](#)]
185. Lu, J.; Hu, H.; Yang, S.; Shanmugam, P.; Wei, W.; Selvaraj, M.; Xie, J. ZnS@carbonaceous aerogel composites fabricated in production of hydrogen and for removal of organic pollutants. *J. Mater. Sci. Mater. Electron.* **2018**, *29*, 8523–8534. [[CrossRef](#)]
186. Maicaneanu, S.A.; McGhee, B.; Stefan, R.; Barbu-Tudoran, L.; Sedwick, C.; Lake, C.H. Investigations on Cationic Dye Degradation using iron-doped carbon xerogel. *Chem. Eng.* **2019**, *3*, 61. [[CrossRef](#)]
187. De Moraes, N.P.; Valim, R.B.; da Silva Rocha, R.; da Silva, M.L.C.P.; Campos, T.M.B.; Thim, G.P.; Rodrigues, L.A. Effect of synthesis medium on structural and photocatalytic properties of ZnO/carbon xerogel composites for solar and visible light degradation of 4-chlorophenol and bisphenol A. *Colloids Surf. A Physicochem. Eng.* **2020**, *584*, 124034. [[CrossRef](#)]
188. Metheniti, M.E.; Frontistis, Z.; Ribeiro, R.S.; Silva, A.M.T.; Faria, J.L.; Gomes, H.T.; Mantzavinos, D. Degradation of propyl paraben by activated persulfate using iron-containing magnetic carbon xerogels: Investigation of water matrix and process synergy effects. *Environ. Sci. Pollut. Res.* **2018**, *25*, 34801–34810. [[CrossRef](#)] [[PubMed](#)]
189. Bailón-García, E.; Elmouwahidi, A.; Carrasco-Marín, F.; Pérez-Cadenas, A.F.; Maldonado-Hódar, F.J. Development of Carbon-ZrO₂ composites with high performance as visible-light photocatalysts. *Appl. Catal. B Environ.* **2017**, *217*, 540–550. [[CrossRef](#)]
190. Fathy, N.A.; El-Khouly, S.M.; Hassan, N.A.; Awad, M.S. Free- and Ni-doped carbon xerogels catalysts for wet peroxide oxidation of methyl orange. *J. Water Process Eng.* **2017**, *16*, 21–27. [[CrossRef](#)]
191. Lima, L.F.d.S.; Coelho, C.R.; Gomes, G.H.M.; Mohallem, N.D.S. Nb₂O₅/SiO₂ mesoporous monoliths synthesized by sol-gel process using ammonium niobate oxalate hydrate as porogenic agent. *J. Sol-Gel Sci. Technol.* **2020**, *93*, 168–174. [[CrossRef](#)]
192. Peter, A.; Mihaly-Cozmuta, A.; Nicula, C.; Mihaly-Cozmuta, L.; Jastrzebska, A.; Olszyna, A.; Baia, L. UV light-assisted degradation of methyl orange, methylene blue, phenol, salicylic acid, and rhodamine B: Photolysis versus Photocatalysis. *Water Air Soil Pollut.* **2017**, *228*, 41–53. [[CrossRef](#)]
193. Mahy, J.G.; Hermans, S.; Tilkin, R.G.; Lamber, S.D. Influence of nucleating agent addition on the textural and photo-Fenton properties of Fe(III)/SiO₂ catalysts. *J. Phys. Chem. Solids* **2020**, *144*, 109502. [[CrossRef](#)]
194. De Oliveira Pereira, L.; Marques Sales, I.; Pereira Zampiere, L.; Vieira, S.S.; Guimarães, I.R.; Magalhães, F. Preparation of magnetic photocatalysts from TiO₂, activated carbon and iron nitrate for environmental remediation. *J. Photochem. Photobiol. A* **2019**, *382*, 111907. [[CrossRef](#)]
195. Baeza, P.; Aballay, P.; Matus, C.; Camú, E.; Ramirez, M.F.; Eyzaguirre, J.; Ojeda, J. Degradation of Paracetamol Adsorbed on Inorganic Supports Under UV Irradiation. *Water Air Soil Pollut.* **2019**, *230*, 34. [[CrossRef](#)]
196. Matos, J.; Poon, P.S.; Montaña, R.; Romero, R.; Gonçalves, G.R.; Schettino, M.A., Jr.; Passamani, E.C.; Freitas, J.C.C. Photocatalytic activity of P-Fe/activated carbon nanocomposites under artificial solar irradiation. *Catal. Today* **2020**, *356*, 226–240. [[CrossRef](#)]
197. Osawa, R.A.; Barrocas, B.T.; Monteiro, O.C.; Oliveira, M.C.; Florêncio, M.H. Photocatalytic degradation of cyclophosphamide and ifosfamide: Effects of wastewater matrix, transformation products and in silico toxicity prediction. *Sci. Total Environ.* **2019**, *692*, 503–510. [[CrossRef](#)]
198. Akshatha, S.; Sreenivasa, S.; Kumar, K.Y.; Archana, S.; Prashanth, M.K.; Prasanna, B.P.; Chakraborty, P.; Krishnaiah, P.; Raghu, M.S.; Alrobei, H. Rutile, mesoporous ruthenium oxide decorated graphene oxide as an efficient visible light driven photocatalyst for hydrogen evolution reaction and organic pollutant degradation. *Mat. Sci. Semicon. Proc.* **2020**, *116*, 105156. [[CrossRef](#)]

199. Pérez-Molina, A.; Morales-Torres, S.; Maldonado-Hódar, F.J.; Pastrana-Martínez, M.L. Functionalized graphene derivatives and TiO₂ for high visible light photodegradation of azo dyes. *Nanomaterials* **2020**, *10*, 1106. [[CrossRef](#)] [[PubMed](#)]
200. Cruz, M.; Gomez, C.; Duran-Valle, C.J.; Pastrana-Martínez, L.M.; Faria, J.L.; Silva, A.M.T.; Faraldos, M.; Bahamonde, A. bare TiO₂ and graphene oxide TiO₂ photocatalysts on the degradation of selected pesticides and influence of the water matrix. *Appl. Surf. Sci.* **2017**, *416*, 1013–1021. [[CrossRef](#)]
201. Zouzalka, R.; Remzova, M.; Plsek, J.; Brabec, L.; Rathousky, J. Immobilized rGO/TiO₂ photocatalyst for decontamination of water. *Catalysts* **2019**, *9*, 708. [[CrossRef](#)]
202. Zhang, B.; Ma, X.; Ma, J.; Zhou, Y.; Liu, G.; Ma, D.; Deng, Z.; Luo, M.; Xin, Y. Fabrication of rGO and g-C₃N₄ co-modified TiO₂ nanotube arrays photoelectrodes with enhanced photocatalytic performance. *J. Colloid Interface Sci.* **2020**, *577*, 75–85. [[CrossRef](#)]
203. Shen, H.; Wang, J.; Jiang, J.; Luo, B.; Mao, B.; Shi, W. All-solid-state Z-scheme system of RGO-Cu₂O/Bi₂O₃ for tetracycline degradation under visible-light irradiation. *Chem. Eng. J.* **2017**, *313*, 508–517. [[CrossRef](#)]
204. Suresh, M.; Sivasamy, A. Bismuth oxide nanoparticles decorated graphene layers for the degradation of Methylene blue dye under visible light irradiations and antimicrobial activities. *J. Environ. Chem. Eng.* **2018**, *6*, 3745–3756. [[CrossRef](#)]
205. Yang, J.; Xie, T.P.; Liu, C.L.; Xu, L.J. Facile fabrication of dumbbell-like beta-Bi₂O₃/graphene nanocomposites and their highly efficient photocatalytic activity. *Materials* **2018**, *11*, 1359. [[CrossRef](#)]
206. Kakavandi, B.; Bahari, N.; Kalantary, R.R.; Fard, E.D. Enhanced sono-photocatalysis of tetracycline antibiotic using TiO₂ decorated on magnetic activated carbon, MAC@T, coupled with US and UV: A new hybrid system. *Ultrason. Sonochem.* **2019**, *55*, 75–85. [[CrossRef](#)]
207. Hamad, H.; Bailón-García, E.; Morales-Torres, S.; Carrasco-Marín, F.; Pérez-Cadenas, A.; Maldonado-Hódar, F.J. Functionalized cellulose for the controlled synthesis of novel carbon–Ti nanocomposites: Physicochemical and photocatalytic properties. *Nanomaterials* **2020**, *10*, 729. [[CrossRef](#)]
208. El Mouchtari, E.M.; Daou, C.; Rafqah, S.; Najjar, F.; Anane, H.; Piram, A.; Hamade, A.; Briche, S.; Wong-Wah-Chung, P. TiO₂ and activated carbon of Argania Spinosa tree nutshells composites for the adsorption photocatalysis removal of pharmaceuticals from aqueous solution. *J. Photochem. Photobiol. A Chem.* **2020**, *388*, 112183. [[CrossRef](#)]
209. Ali, S.; Li, Z.; Chen, S.; Zada, A.; Khan, I.; Khan, I.; Ali, W.; Shaheen, S.; Qu, Y.; Jing, L. Synthesis of activated carbon-supported TiO₂-based nano-photocatalysts with well recycling for efficiently degrading high-concentration pollutants. *Catal. Today* **2019**, *335*, 557–564. [[CrossRef](#)]
210. Shokouhi, S.B.; Dehghanzadeh, R.; Aslani, H.; Shahmahdi, N. Activated carbon catalyzed ozonation (ACCO) of Reactive Blue 194 azo dye in aqueous saline solution: Experimental parameters, kinetic and analysis of activated carbon properties. *J. Water Process Eng.* **2020**, *35*, 101188. [[CrossRef](#)]
211. Rajah, Z.; Guiza, M.; Solís, R.R.; Rivas, F.J.; Ouederni, A. Catalytic and photocatalytic ozonation with activated carbon as technologies in the removal of aqueous micropollutants. *J. Photochem. Photobiol. A Chem.* **2019**, *382*, 111961. [[CrossRef](#)]
212. Zhang, J.; Huang, G.Q.; Liu, C.; Zhang, R.N.; Chen, X.X.; Zhang, L. Synergistic effect of microbubbles and activated carbon on the ozonation treatment of synthetic dyeing wastewater. *Sep. Purif. Technol.* **2018**, *201*, 10–18. [[CrossRef](#)]
213. Vatankhah, H.; Riley, M.S.; Murray, C.; Quiñones, O.; Steirer, K.X.; Dickenson, E.R.V.; Bellona, C. Simultaneous ozone and granular activated carbon for advanced treatment of micropollutants in municipal wastewater effluent. *Chemosphere* **2019**, *234*, 845–854. [[CrossRef](#)]
214. Rozas, O.; Baeza, C.; Núñez, K.; Rossner, A.; Urrutia, R.; Mansilla, H.D. Organic micropollutants (OMPs) oxidation by ozone: Effect of activated carbon on toxicity abatement. *Sci. Total Environ.* **2017**, *590–591*, 430–439. [[CrossRef](#)]
215. Hu, E.; Shang, S.M.; Tao, X.M.; Jiang, S.X.; Chiu, K.L. Minimizing freshwater consumption in the wash-off step in textile reactive dyeing by catalytic ozonation with carbon aerogel hosted bimetallic catalyst. *Polymers* **2018**, *10*, 193. [[CrossRef](#)]
216. Hu, E.; Shang, S.; Chiu, K.L. Removal of reactive dyes in textile effluents by catalytic ozonation pursuing on-site effluent recycling. *Molecules* **2019**, *24*, 2755. [[CrossRef](#)]

217. Zhang, J.; Xiong, Z.; Wei, J.; Song, Y.; Ren, Y.; Xu, D.; Lai, B. Catalytic ozonation of penicillin G using cerium-loaded natural zeolite (CZ): Efficacy, mechanisms, pathways and toxicity assessment. *Chem. Eng. J.* **2020**, *383*, 123144. [[CrossRef](#)]
218. Chen, C.; Yan, X.; Yoza, B.A.; Zhou, T.; Li, Y.; Zhan, Y.; Wang, Q.; Li, Q.X. Efficiencies and mechanisms of ZSM5 zeolites loaded with cerium, iron, or manganese oxides for catalytic ozonation of nitrobenzene in water. *Sci. Total Environ.* **2018**, *612*, 1424–1432. [[CrossRef](#)] [[PubMed](#)]
219. Ikhlaq, A.; Waheed, S.; Joya, K.S.; Kazmi, M. Catalytic ozonation of paracetamol on zeolite A: Non-radical mechanism. *Catal. Commun.* **2018**, *112*, 15–20. [[CrossRef](#)]
220. Saeid, S.; Tolvanen, P.; Kumar, N.; Eränen, K.; Peltonen, J.; Peurla, M.; Mikkola, J.P.; Franz, A.; Salmi, T. Advanced oxidation process for the removal of ibuprofen from aqueous solution: A non-catalytic and catalytic ozonation study in a semi-batch reactor. *Appl. Catal. B Environ.* **2018**, *230*, 77–90. [[CrossRef](#)]
221. Derco, J.; Dudáš, J.; Valičková, M.; Šimovičová, K.; Kecskés, J. Removal of micropollutants by ozone based processes. *Chem. Eng. Process.* **2015**, *94*, 78–84. [[CrossRef](#)]

Publisher’s Note: MDPI stays neutral with regard to jurisdictional claims in published maps and institutional affiliations.



© 2020 by the authors. Licensee MDPI, Basel, Switzerland. This article is an open access article distributed under the terms and conditions of the Creative Commons Attribution (CC BY) license (<http://creativecommons.org/licenses/by/4.0/>).